THE UNIVERSITY OF CHICAGO

SEEKING DESIGN PRINCIPLES FOR CONTROL OF ULTRAFAST ENERGY TRANSFER IN SYNTHETIC LIGHT HARVESTING SCAFFOLDS

A DISSERTATION SUBMITTED TO
THE FACULTY OF THE DIVISION OF THE PHYSICAL SCIENCES
IN CANDIDACY FOR THE DEGREE OF
DOCTOR OF PHILOSOPHY

DEPARTMENT OF CHEMISTRY

BY
RICHARD J. MAZUSKI

CHICAGO, ILLINOIS
AUGUST 2020

to Pan

TABLE OF CONTENTS

LIST OF FIGURES

LIST OF TABLES

ACKNOWLEDGMENTS

My time during graduate school was supported by the National Science Foundation Graduate Research Fellowship Program (NSF-GRFP) under grant No. DGE-1746045. Additional support for the research presented was made possible by the U.S. Naval Research Laboratory (NRL), the NRL Nanoscience Institute for base funding, and the Laboratory University Collaborative Initiative (LUCI). The work at Engel Group at the University of Chicago was supported by the Vannevar Bush Faculty Fellowship Program (Grant No. N00014-16-1-2513 and N00014-15-1-0048), the Air Force Office of Scientific Research (AFOSR) (FA9550-18-1-0099 and FA9550-16-1-0347) and the NSF (under grant no. 1900359).

First, I thank my research advisor, Professor Gregory S. Engel for his support and enthusiasm during the past five years. Research can sometimes take years to bear fruit, so I truly appreciate the reassurance Greg grants all his students even when progress takes a long time to be apparent. I will always remember my time at the University of Chicago fondly and I believe that future students from the Engel Group will continue to find success due to Greg's trusting approach. Beyond research, Greg has been a great mentor in terms of professional development and is always happy to have his students forge their own paths both during their time researching, as well as in preparation for whatever career path they choose. This has made it possible to investigate future plans and potential careers without needless stress.

The Engel Group as a whole was a very welcoming place to research. In particular, I wish to thank Dr. Marco Allodi for his help in our first project on Optical Resonance Imaging and for really teaching me about ultrafast spectroscopy. Additionally, I was very lucky to have a wonderful, smart peergroup who kept me honest and instilled a great atmosphere in the lab. Dr. Ryan Wood and Lawson Lloyd were instrumental in helping to set up the Redfield Lab for my samples and got me through many, many different fluences of pump probe. The atmosphere of scholarship and academic rigor was evident from the very first

summer of research, and I wish to acknowledge Engel group alumni for having nurtured such an environment, namely Dr. Peter Dahlberg, Prof. Moira Flanagan, Prof. Sara Massey, Dr. John Otto, Dr. Brian Rolczynski, Dr. Ved Singh, Dr. Sara Sohail, Dr. Lili Wang, Dr. Nick Williams, and Dr. Haibin Zheng. I also wish to thank the rest of the Engel Group who provide a fun and supportive atmosphere to conduct research, particularly Sami Abdulhadi, Elizabeth Bain, Jake Higgins, Polina Navotnaya, Siddhartha Sohoni, Po-Chieh Ting, and Sarah Zinn.

I am grateful for my defense committee members, Professor David Mazziotti and Professor Bozhi Tian for their support and accommodating my defense under trying circumstances.

I thank my collaborators at the Naval Research Lab, Dr. Sebastian Diaz and Dr. Igor Medintz, for constructing the DNA-dye samples and assisting in the preparation of our manuscript on the Cy5 molecular photonic wires.

Finally, my family as a whole has constantly been a great source of inspiration. My parents have always provided my siblings and me with love, stability, and reassurance to follow our own paths. My three siblings have provided great role models, and in particular my two sisters, Cristina and Andrea, who both completed PhDs before me, have been a constant source of inspiration. Last, but certainly foremost, I wish to thank my partner, Pan Xiao for her loving support for as long as we have been together. It was upon her suggestion that I applied and ended up attending University of Chicago, as I hadn't considered it a possibility. This one example is a microcosm of the thought and support she grants me everyday, and looking forward to our future, I hope to repay her in full for all the time and effort she has spent encouraging me throughout these past five years.

ABSTRACT

Using solar energy as an efficient renewable energy source is one of the grand challenges for science in the 21st century. Chemistry has succeeded in synthesizing a vast library of tailor-made light harvesting molecules, but tethering these molecules in a useful way that creates a system more than the sum of its parts has proven to be a challenge. Photobiology, on the other hand, has succeeded at using only a few chromophores to create efficient light harvesting networks due to their protein scaffolds, which hold and modulate the photoactive components with unmatched precision. Synthetic light harvesting seeks to mimic this approach, with dyes on double stranded DNA becoming a standard means of studying fundamental energy transfer properties as well as having applications in many bio-applied sciences. While creating new synthetic machinery and divulging energy transfer properties through spectroscopy and process of elimination is valuable, it is an indirect means of characterizing an exciton, while an ultrafast microscopy would enable the direct viewing of excitons and charge carriers. Coupled together, this research seeks a fundamental understanding of the photophysics driving light harvesting and manipulation. In dye-DNA work, the existence of an ultrafast nonradiative trap state in a molecular photonic wire composed of Cy5 dimers was determined to be linked to macroscale dynamics of the molecular photonic wire as a whole, where both the trap state and the overall dynamics were tied to fluence and temperature. In complementary work, a novel technique called ORI was theorized, which could lead to the direct imaging of ultrafast energy transfer through excitons. Finally, preliminary work on a more sophisticated system, the four-arm star, is presented, in which incipient fluence dependence is seen.

CHAPTER 1

SYNTHETIC LIGHT HARVESTING SYSTEMS: THEORY, APPLICATIONS, AND STUDIES

Solar energy is a plentiful radiative energy source which reaches the earth at a maximum power of 120,000 TW. Although only a fraction of that can be used for photovoltaic applications (due to sub-optimal land coverage, weather conditions, etc.), the total power still dwarfs the energy expenditure of the world from 2018, 18 TW. Photosynthesis has evolved over billions of years to efficiently harness photonic energy from the Sun and harvests 130 TW of solar energy into biomass each year. A grand challenge of science has been to take inspiration from photosynthesis to better use the renewable power of the Sun for humanity's energy needs. [1, 2, 3]

Synthetic light harvesting systems are designed to harness the powerful radiation from the Sun towards useful work. The use of the words 'light harvesting' is deliberate as these devices seek to emulate the efficient excitation energy transfer seen in photosynthetic complexes, which generally make use of peripheral light harvesting (LH) antennae to siphon photonic energy downhill towards reaction centers (RC). Photosynthesis has a multi-billion year head start compared to synthetic light harvesting, whose first studies only appeared a few decades ago. Therefore, any foray into solar energy harnessing, if it is to be efficient, must be informed by our understanding of photosynthetic design principles. [4, 5]

In the following research, we draw inspiration from photosynthesis to efficiently and thoroughly study the energy transfer properties of sythetic light harvesting media, primarily composed of molecular dyes attached to double-stranded (ds) DNA scaffolds. This scheme is analogous to photosynthetic complexes, in which photoactive chromophores are embedded in a protein scaffold. Spectroscopic studies into the design principles of photosynthesis are quite numerous,[6, 7, 8] but beyond the scope of this thesis. A basic review of several outstanding energy transfer schemes, however, will be helpful to understand the motivation

behind the types of constructs studied and the spectroscopic methods employed in this research. Following this cursory introduction into multiple photosynthetic design principles, a brief review of synthetic light harvesting systems will follow.

1.1 Inspiration from Photosynthesis: Design Principles Towards Efficient Energy Transfer

Scientific advances have always arisen from humanity's desire to understand the world around us. Given society's current need for a renewable and reliable source of energy, it makes sense for newest generations of energy harvesting media to be inspired by photosynthesis. The solar spectrum (Figure 1.1) shows several key characteristics which influence our methods of understanding light harvesting in photosynthesis. First off, there is a large bandwidth of wavelengths between 400-700 nm which remains near flat (as in, no discernible spikes of intensity). Additionally, the absorption bands of water play a key role in determining which wavelengths reach the surface. This becomes even more pronounced considering aquatic photosynthesis, since scattering affects bluer wavelengths much more severely than redder wavelengths. [9, 10]

The initial absorption and energy transfer events in photosynthetic organisms are simply the first step in a larger, slower process that culminates in the synthesis of stable carbon compounds towards the creation of biomass. For a full discussion of the mechanisms of photosynthesis, readers are advised towards Professor Robert Blankenship's book, *Molecular Mechanisms of Photosynthesis.*[12] Briefly, following initial absorption by antenna complexes, energy is funneled spatially from many peripheral complexes towards fewer numbers of core complexes and finally even fewer reaction centers. This spatial funneling is typically accompanied by a similar energetic funneling, in which energy absorbed at bluer wavelengths is transferred downhill towards redder wavelengths. Following energy transfer to the pigment-protein complex known as the reaction center, the primary pigment of the reaction center

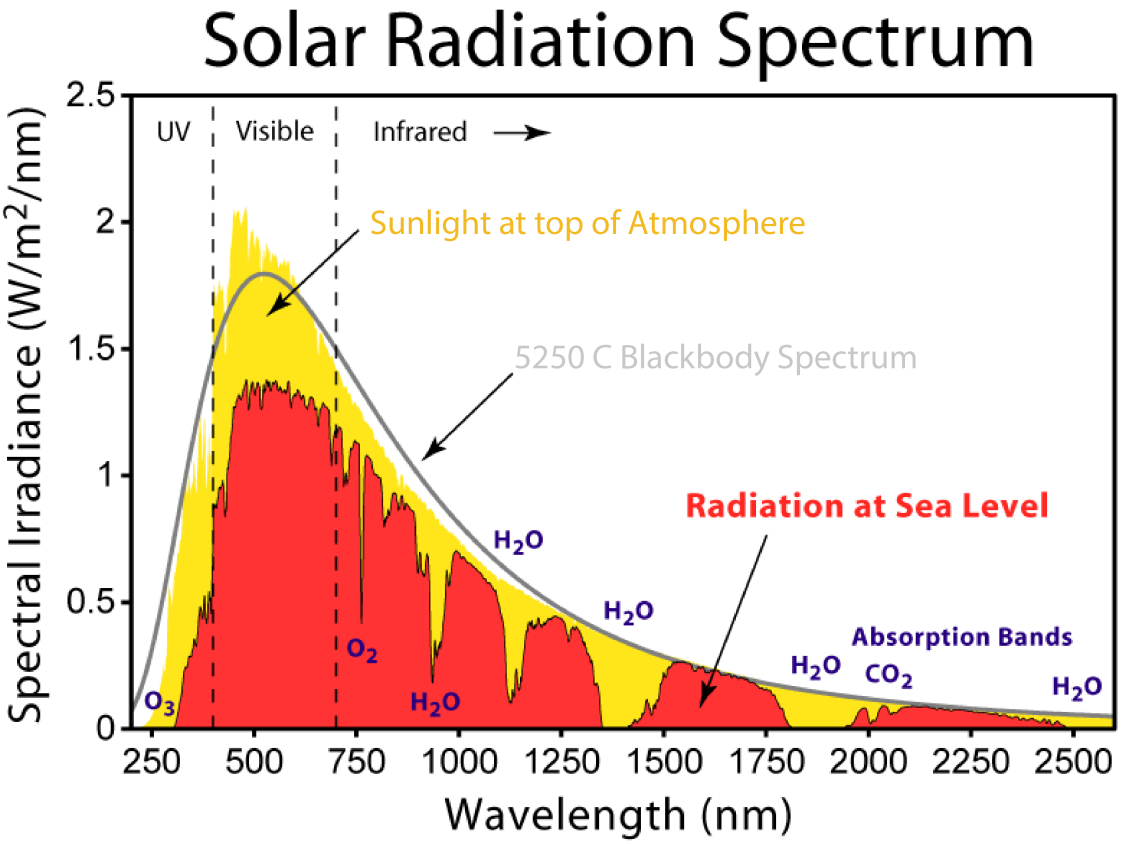

Figure 1.1: Total irradiance of solar spectrum as seen in vacuum and at the Earth's surface, as collected by the American Society for Testing and Materials (ASTM) Terrestrial Reference Standard. Important features of this spectrum include the absorption due to prevalent gases in the Earth's atmosphere as well as the redistribution of wavelengths due to Rayleigh and Mie scattering. Adapted from [11] within conditions set by Creative Commons license CC BY-SA 3.0.

enters an excited state, and this energetic state is transformed into an electron transfer mechanism through an electron donor-acceptor reaction. Following this primary electron transfer, the stabilization and separation of positive and negative charged species is necessary, and occurs through various secondary reactions. The final step of photosynthesis is the creation of stable bio-products, which typically involves the creation of NADPH from $NADP^+$. Overall, the entire process of photosynthesis from start to finish takes seconds to complete, although the initial absorption and energy transfer events only take femto- to picoseconds (10^{-15} to 10^{-12} s). As spectroscopists, we seek for design principles from the initial energy absorption and transfer events which lead to the remarkable stability and efficiency of photosynthesis.[12]

As expected, this over-simplification of photosynthesis hardly encompasses the vast array of organisms, from pond scum to redwood trees, that use it to stay alive. Similarly, energy transfer during the initial steps of photosynthesis varies widely from simpler funnel-like structure, to more rugged and complex landscapes which allow for multiple excitonic pathways and secondary quenching reactions.[13, 14, 15] Despite these wide differences, there are some common motifs which can be extracted from previous studies in photosynthesis and extrapolated towards our understanding of synthetic light harvesting systems. These include dense packing of the same chromophore to achieve directional energy transfer, the ability to handle differing levels of light, and constructive use of different energy transfer schemes based on inter-chromophore distance.

1.1.1 Placement of Chromophores and Directional Energy Transfer

Purple bacteria make ideal model systems for spectroscopically studying photosynthesis due to their inherent simplicity (at least when compared to higher plants) and the robust growth conditions. In particular, Light-Harvesting Complexes 1 and 2 (LH1 and LH2) of *Rhodobacter sphaeroides* have been studied due to their well-defined spectral signatures and facile

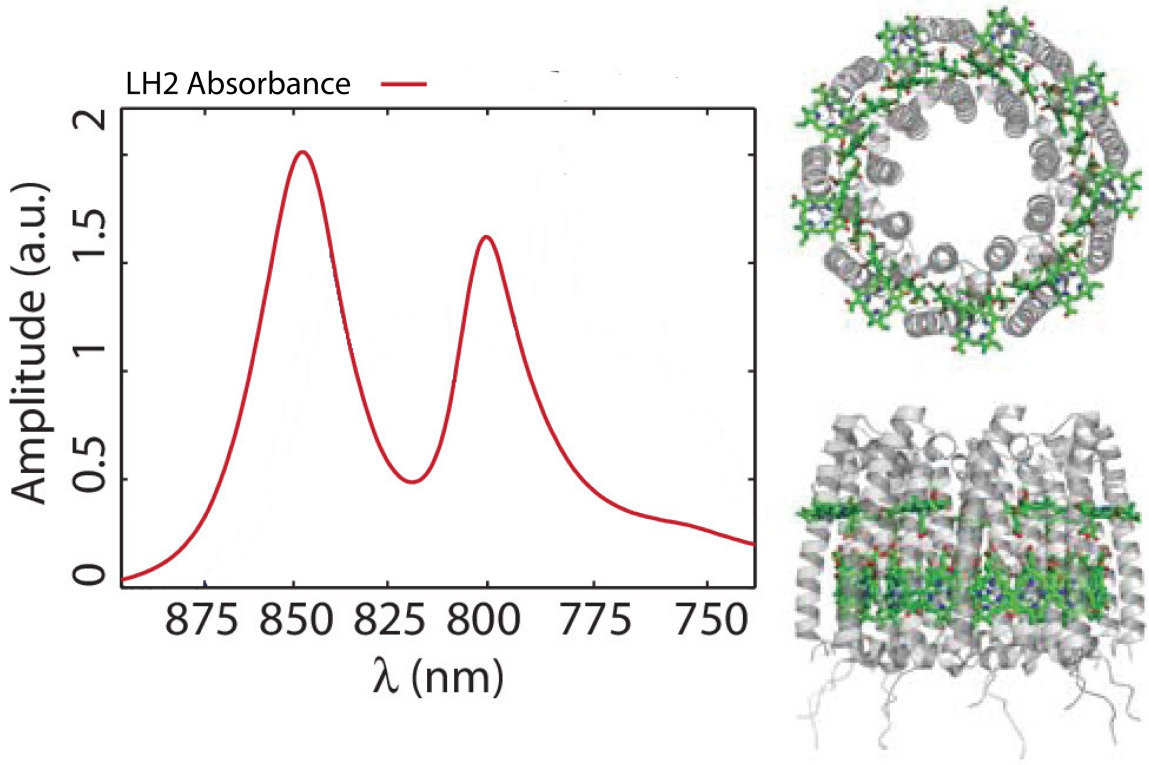

Figure 1.2: Linear absorption spectrum and cyrstal structures of the LH2 complex. The two bands in the absorption are due to two distinct rings of BChl *a*, one strongly coupled at 850 nm and another less strongly coupled at 800 nm. A higher-lying excited state of B850 is also responsible for the slight shoulder seen at 770nm. Figure adapted, with permission, from [17].

isolation.[16] LH2 is composed of two concentric rings of the pigment bacteriochlorophyll *a* (BChl *a*), the outermost having 9 weakly coupled pigments, while the inner is composed of 18 strongly coupled pigments. These two rings have optical signatures at 800 nm and 850 nm and are aptly known as the B800 and B850 rings. The optical spectrum and structural diagram are shown in Figure 1.2.

Within this simplest of organisms, many design principles begin to emerge. The ultimate goal of any peripheral light harvesting complex is to transfer energy to the reaction center, where actual electrochemical change can begin to occur. The logical way that *Rba. sphaeroides* achieves this is by using downhill energetics to ensure that exciton flow from

LH2 (absorption 800 nm or 850 nm) to LH1 (absorption at 875 nm) to the reaction center (absorption at 870 nm) is energetically favorable or at least, in the final LH1 to RC case, not highly unfavorable. Although this simplicity can be masked in the more energetically rugged realm of higher plants, the same funneling can still be seen to occur, although it has been hypothesized that the energetics are optimized for photoprotection rather than efficiency.

Two important regimes of pigment placement are considered when spectroscopists look at photosynthetic compounds, system-system coupling and system-bath coupling. System-bath coupling can involve any number of interactions that the pigment (system) undergoes within its protein-scaffold (bath), such as vibrational damping and electrostatic effects brought on by hydrogen bonding.[18] System-system interactions involve energetic couplings brought on by dipole-dipole interactions, orbital mixing, and other electronic effects. In the following work, the energetic couplings between cooperative chromophores were the primary regime of study, and thus, although they are quite important, system-bath couplings will not be discussed in greater detail.

Since energy transfer within photosynthesis and light harvesting material is by its very definition the transfer of excited state energy (via a quasiparticle known as an exciton) from one system to another, it is important to consider different parameters that quantify this system-system coupling. Typically, coupling is quantified with an energetic constant which describes the cross terms in the excitonic Hamiltonian. One way to theoretically calculate inter-system coupling uses an excitonic Hamiltonian and reproduces absorption spectra. Practically, this inter-system coupling can describe how collectively a photosynthetic construct operates during energy transfer events. For example, in *Rba. sphaeroides*, the B800 ring is canonically described as weakly coupled due to each BChl *a* have a coupling strength of $\sim$20cm^{-1}, whereas the B850 ring consists of strongly coupled pigments at a value of $\sim$300 cm^{-1}. In part, the greater coupling of the B850 ring can in part explain the redshifting of the absorption.[19, 20]

A closer look at LH2 demonstrates several factors determining the strength of coupling. First, inter-chormaphore distance plays the most critical role in determining the strength of coupling. In LH2's red-shifted B850 ring, BChl *a* are separated by 3.4-3.9 Å, while the distance is almost an order of magnitude greater in the B800 ring, with around 22 Å separation. In addition to distance, orientation plays many roles within the inherent success of photosynthetic light harvesting. Recent discoveries by Massey et al. resolve the transfer of excitation between the B800 and B850 rings using polarization-controlled two-dimensional electronic spectroscopy (2DES) to find that excitations originally on the B800 ring have access to be transferred to an excited state of B850 (termed B850*) through their orientational dynamics. [21]

While the full extent of chiral and orientational effects on the efficiency of energy transfer remains an open research question, many of the simplest of photosynthetic species still demonstrate great sensitivity to even minute perturbations. Photosynthetic quenching, which is discussed in Section 1.1.2, also exhibits dramatic sensitivity to orientation perturbations.[22, 23] Figure 1.3 shows such orientational effects in LH2, which shifts the placement of carotenoid when found in *Rhodopseudomonas acidophila* versus *Phaeospirillum molischianum*. Beyond differences in symmetry, where *Rps. acidophila* has nine-fold symmetry (the exact same as *Rba. sphaeroides*) while *Ph. molischianum* has eight-fold symmetry, a major deviation in these organism arises from the relative orientation of the BChl *a* in the ring. In the former case the B800 BChls are perpendicular to B850 BChls, the latter case has a less perpendicular arrangement. Additionally important is the fact that these orientations also impact the overlap with the carotenoid located in between the two rings.

From these quick case studies of the simplest of photosynthetic organisms a few design principles emerge. First, an energetic and spatial funneling is used to facilitate downhill energy transfer. This funnel is created often using the same pigments which are arranged in specific orientations and set distances to provide the necessary energetics to make this down-

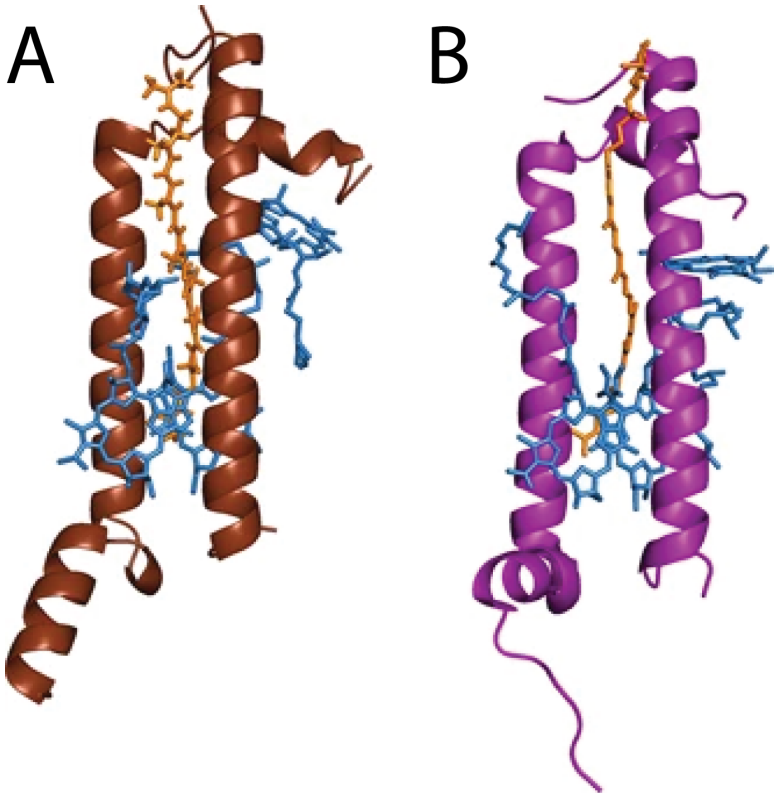

Figure 1.3: PDB structures of the LH2 α/β heterodimers from (A) *Ph. molischianum (left)* and (B) *Rps. acidophila (right)* in which BChl *a*'s are highlighted in blue and carotenoids are highlighted in orange. In each heterodimer, one carotenoid is in electrical contact with three BChl *a*. Figure adapted, with permission from [23].

hill transfer possible. Within this domain of specific orientation, dipole-dipole interactions are tuned along a spectrum between the strong and weak coupling limit. Finally, we have seen the use of orientational factors to couple higher lying excited states and also to create different schemes of photoprotection.

1.1.2 Ability to Handle Multiple Excitations

The robustness of any functional material can be seen as its ability to adapt to changing conditions and environmental stressors. In photosynthesis, the changing conditions are mainly due to increased and decreased light fluence. Given the previously discussed spatial and energetic funneling into RCs exhibited in many photosynthetic organisms, the development of photoinhibition mechanisms is necessary to prevent any unnecessary damage due to over-excitation. Damage due to over-excitation can usually be traced to highly reactive oxygenic species that may cause chemical change in the organism if they are not quenched.[24] Cyanobacteria contain an Orange Carotenoid Protein (OCP) which can provide a mechanism for non-photochemical quenching (NPQ).[25] Current research points to the OCP as functioning in a wide variety of roles, including as initial light sensor, a signal propagator for photoprotective measures, and the site of energy quenching.[26] It is clear from the wide variety of roles that one simple carotenoid molecule can fill that nature has carefully tuned the protein environment to adapt to a wide variety of conditions, and that for synthetic light harvesting materials to achieve any widespread utility, they should also seek similar capabilities.

Beyond simply photoprotection, multiple excitation dynamics (also termed fluence dependent dynamics) play a key role in studying photosynthetic material. Recent results from Dahlberg et al. have shown the utility of fluence-dependent measurements as a means of mapping ultrafast energy flow. Figure 1.4 shows fluence-dependent waiting time traces taken from the maximum of the positive feature of LH2 from *Rba. sphaeroides*. It is important to

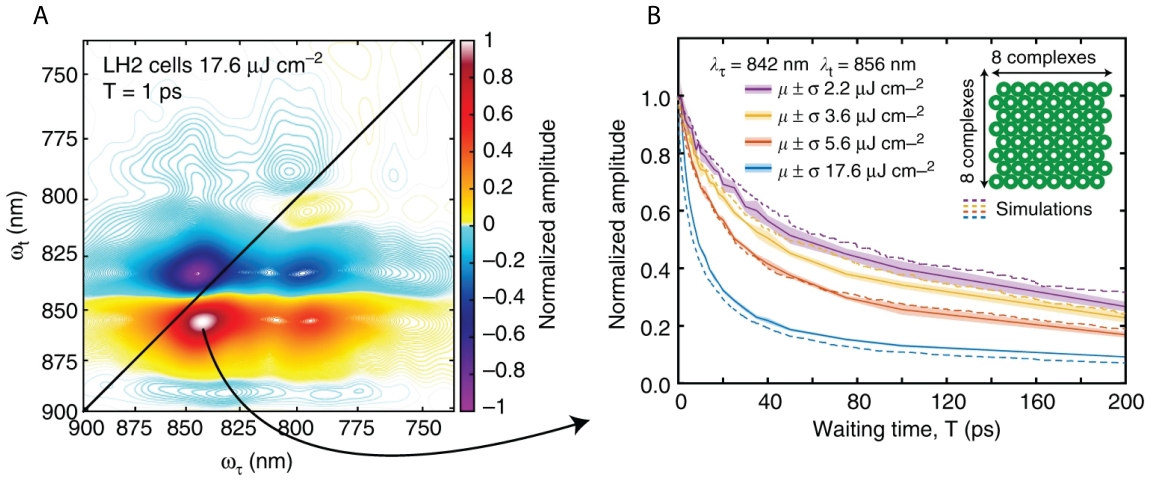

Figure 1.4: (A) Absorptive 2DES spectrum of LH2 at relatively high fluence. (B) Waiting time traces picked from the maximum ground state bleach/stimulated emission feature. Shaded regions represent mean plus one standard deviation. The anticorrelation between increased fluence and resulting lifetime is emblematic of exciton-exciton annihilation. Dashed traces represent a random walk simulation made from a sheet of 8-by-8 LH2 molecules, where fluorescence lifetime is 250 ps and average energy transfer time is 2.7 ps. Adapted with permission from [27] and within Creative Commons Attribution 4.0 International License.

note the clear anti-correlation between increased fluence and excited state lifetime, or in other words, the fact that as fluence is increased, lifetime decreases. This is due to, in most part, the prevalence of exciton-exciton annihilation (EEA) in strongly coupled multi-chromophore systems as excited state species increase.

Dissipative measures such as photoprotection and EEA are just some examples of multi-photon effects, as many different events can take place prior to fluorescence, which include internal conversion (IC) among many others.[28] It has been theorized that the rugged excited state terrain in the light harvesting complexes of higher plants has been tuned to deal with multiple excitations in these different ways. Indeed, in many cases, science's understanding of molecular aggregates aids in the understanding of chlorophyll-chlorophyll interactions, which in turn aids the creation of synthetic light harvesting systems. Similarly, the use of fluence-dependent ultrafast spectroscopy in the same sense opens up photosynthetic media to changing environments while also informing the underlying energy transfer mechanics.

1.1.3 Use of Different Energy Transfer Mechanisms

Excitation energy transfer (EET) encompasses the initial step of photosynthesis in which photonic energy is captured by antenna complexes. Modeling and understanding EET has been the fundamental research topic into photosyntehsis for the past fifteen years, and as is usually the case, as more work is put in, more questions emerge. In this section, I will introduce two energy transfer models, Förster Resonance Energy Transfer (FRET) and Redfield Theory, and briefly explain a third, coherent energy transfer. The first two theories represent opposite sides of the inter-chromophore coupling spectrum, with FRET being used to describe energy transfer between distinct chromophores with little excited state mixing whereas Redfield Theory describes energy transfer when inter-chromophore coupling is much stronger when compared to chromophore-bath coupling. Even within the simple structure of the LH2 of *Rba. sphaeroides*, both these mechanisms play important roles, where Redfield

Theory more accurately describes energy transfer within the individual rings, particularly the B850 ring, and FRET describes inter-LH2 hopping.[29] Coherent energy transfer represents a case where coupling between environment and chromophores is roughly equal and it is neceassary to treat the system quantum mechanically. Although there have been repeated experimental observations and theoretical descriptions of coherent energy transfer, the nature of the coherences and their overall impact on photosynthetic efficiency has been fiercely debated over the past decade.

Förster Resonance Energy Transfer

FRET is an incoherent, nonradiative energy transfer mechanism. FRET describes energy transfer which occurs between distinct chromophores and typically occurs in the single nanometer regime (approximately 2-10 nm for most chromophores). The rate of energy transfer is determined by dipole-dipole interactions and is characterized by a strong distance dependence (r^6).[30] In the simplest case, FRET can be described as a first order kinetics equation describing the following situation:

$$\frac{1}{\tau_{DA}} = k_{DA} = k_{D,f} + k_{D,nr} + k_{ET} \tag{1.1}$$

where in Equation 1.1, τ_{DA} is the excited state lifetime of the donor-acceptor moiety, and $k_{D,f}$, $k_{D,nr}$, and k_{ET} are the rates of fluorescence, nonradiative excited state quenching, and energy transfer, respectively. While the key aspect of Equation 1.1 is the competition between corresponding rates of nonradiative pathways and fluorescence with the energy transfer rate, it is important to describe the energy transfer rate in greater detail, particularly with respect to distance between donor and acceptor. This equation is as follows:

$$k_{ET} = \frac{1}{\tau_D} \times \left(\frac{R_0}{r}\right)^6 \tag{1.2}$$

where τ_D is the fluorescent lifetime of the donor and the $\frac{R_0}{r}$ is the quotient between the nominal FRET distance where efficiency is 50% (R_0), and the donor-acceptor distance (r). The r^6 dependence on this quotient makes for a steep drop-off in FRET rate as the distance between donor-acceptor exceeds the FRET distance. The nominal FRET distance itself is determined from Fermi's Golden Rule and can be expressed in the following equation:

$$R_0^6 = \frac{2.07}{128\pi^5 N_A} \frac{\kappa^2 Q_D}{n^4} \int F_D(\lambda)\epsilon_A(\lambda)\lambda^4 d\lambda \tag{1.3}$$

where N_A is Avogadro's number, κ^2 is the orientation factor for the transition dipoles (typically set at 2/3 for freely rotating species), Q_D is fluorescence quantum yield of the donor absent the acceptor, n is the refractive index, and the integral represents the spectral overlap of the donor's fluorescence and the acceptor's absorbance as a function of wavelength, where $F_D(\lambda)$ is the overlap spectrum normalized to an area of one, $\epsilon_A(\lambda)$ is the acceptor molar extinction coefficient, and λ itself is the wavelength. The full integrand from equation 1.3 is commonly referred to as the J-integrand and is the metric by which different fluorophore pairs are compared for FRET efficacy.

In practice, beyond simply being a model to understand energy transfer in the weak-coupling limit, FRET is also a tool used in many fields, but most notably biology, to measure distances with single nanometer resolution.[32] FRET networks have also been constructed to manipulate photonic energy on the nanoscale.[33] To best utilize FRET as a means of energy transfer, orientation, distance, and energetics have to be considered. Figure 1.5 shows various configurations of FRET's viability, including spectral overlap (a), distance (b), and orientation (c).

Redfield Theory

Whereas FRET can best describe states where localized energetics of single chromophores transferring energy between one another, Redfield Theory better describes delocalized en-

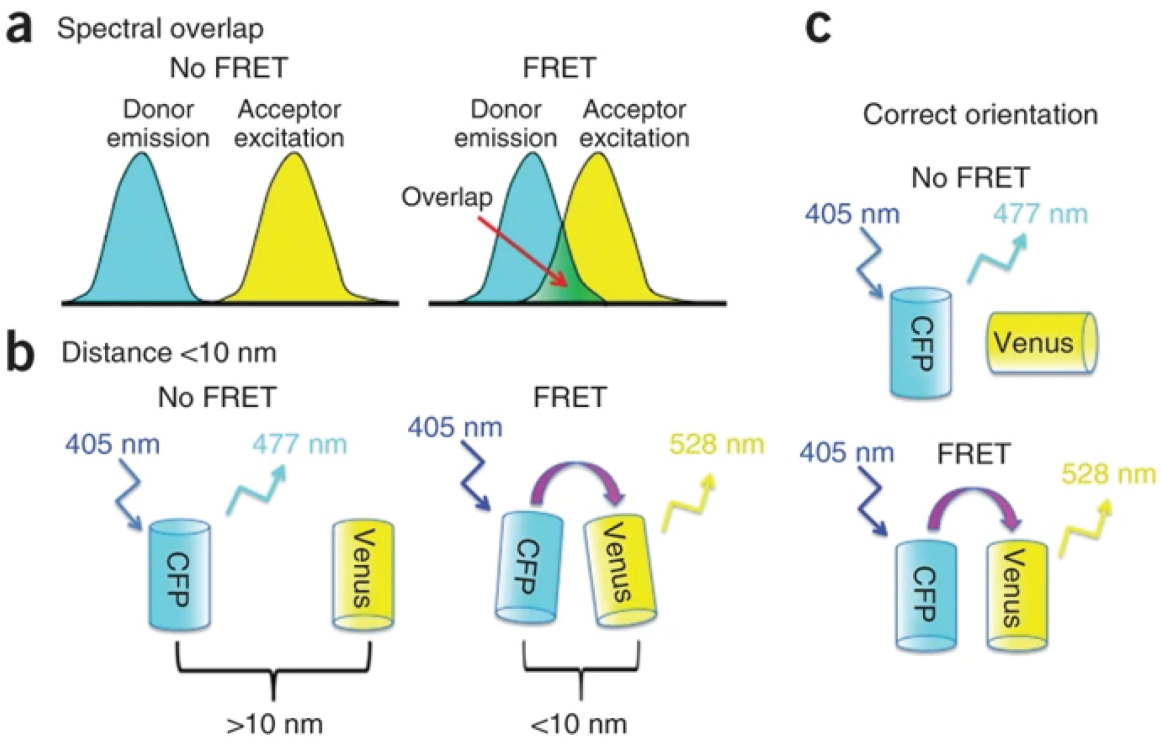

Figure 1.5: (a) Spectral overlap between donor emission and acceptor absorbance must exist. This overlap is quantitatively described by the J-integrand in Equation 3. (b) Typically, nominal FRET distances are between 2 - 10 nm. When distance is less than 2 nm, strong electronic coupling causes other transfer schemes to become much more prevalent. Above 10 nm, typically dipole-dipole coupling falls significantly. (c) Perpendicular arrangement of transition dipoles will lead to no energy transfer. Adapted with permission from [31]

.

ergetic states occupying sites of multiple chromophores. Redfield Theory is originally used to describe coupling terms in Nuclear Magnetic Resonance spectroscopy (NMR), and has since been applied to strongly coupled optical systems, such as photosynthetic organisms. A key assumption in using Redfield Theory to explain NMR is that the relaxation times are several orders of magnitude longer than the correlation times driving relaxation processes. Typical NMR relaxation times could be on the order of milliseconds, whereas water-sample correlation times due to tumbling and vibrational damping are on the picosecond timescale, so overall, Redfield Theory would be valid. Moving by analogy over to the optical regime, when system-bath interactions (such as proteins damping photonic energy, or solvent effects) are much slower than system-system interactions, a major source of the relaxation could be described by Redfield Theory.[34]

The rate describing relaxation between two delocalized states $|A\rangle$ and $|B\rangle$ is described by the following equation:

$$k_{A\to B} = 2\gamma_{AB}\widetilde{C}^{Re}(\omega_{AB}) \tag{1.4}$$

where important parameters include the energy mismatch between states $|A\rangle$ and $|B\rangle$, ω_{AB}, spatial overlap and vibrational correlation of these delocalized states, γ_{AB}, and purturbative treatment of the surrounding environment, $\widetilde{C}^{Re}$. This perturbative treatment of coupling to the surrounding environment is one of the key aspects of Redfield Theory, and should a more advanced treatment of the environment be necessary, as is often the case in modeling spectroscopic results in photosynthesis research, modified Redfield theory can be used. Modified Redfield Theory invokes both strong excitonic coupling as well as strong vibronic coupling without treating either as a perturbation. Additionally, FRET (see section 1.1.3) can be expanded into Generalized FRET Theory, which applies to domains of delocalized states that are weakly coupled to one another. While another theory other than Generalized FRET would be necessary to explain energy transfer within the domains themselves,

Generalized FRET can account for inter-domain energy transfer and is useful in the study of molecular aggregates as well as photosynthetic pigment clusters.[35]

Coherent Energy Transfer

Coherent energy transfer expands on any of the previously discussed theories of energy transfer by treating every portion of the excitation quantum mechanically. Using FRET or Refield Theory to accurately describe empirical evidence of spectroscopy on photosynthetic organisms is inaccurate, failing to account for the rapid energy transfer rate. In the intermediate regime of electronic coupling, the dynamics of donor-acceptor electronic energy exchange can be explained by quantum coherence. While the degree to which quantum coherence affects overall photosynthetic efficiency is still debated in the field,[36] quantum coherence has been shown in both theory and experiments to be a major factor in overall energy transfer when electronic coupling is similar in magnitude to exciton-bath coupling.[37] The excitonic wavefunction will evolve phase due to resonance between different pathways and interference from the bath. Whereas a more classical approach deals with single excitonic paths, under coherent energy transfer theory many paths can be sampled at the same time and the resulting exciton dephases. In contrast to random, diffusive motion such as FRET hops, coherent energy transfer is based on quantum probability amplitudes, and thus points to a more directed and controllable method of energy manipulation.[38, 39]

Dexter Energy Transfer

Beyond singlet energy transfer, it is important to consider other excited state species such as triplets. A new theory for energy transfer of "forbidden" transitions (or optical transitions not reachable in the dipole-approximation) was proposed by D.L. Dexter from the Metallurgy Division of the U.S. Naval Research Lab (NRL) to describe energy transfer within crystalline lattices of phosphors. The distance dependence of Dexter Energy Transfer is much more

stringent than even FRET, with an exponential ($e^{-\alpha r}$) dependence. The factor α concerns orbital overlap, so spatial arrangement and proximity becomes the overwhelming factor for Dexter Energy Transfer. This theory can be used to describe close range transport of triplets in crystalline pentacene, but taken together with FRET, it does not present a unified theory.[40]

Overall, in terms of photosynthetic design principles, we have seen the use of multiple energy transfer schemes used to describe the initial steps of photon capture and transfer. It would thus stand to reason that any synthetic materials would follow such an example and seek to multiplex over many regimes, from strong to weak coupling and from short to long range transfer.

1.2 Current State of Synthetic Light Harvesting Systems

The history of chemistry has seen the synthesis of new molecules being one of the key methods to overcome challenges. Photosynthesis, by contrast, manipulates the arrangement of a small array of pigments around a protein scaffold to achieve near unity quantum efficiency. In LH2, two distinct rings of BChl *a* were used to create an energetic and spatial funnel. Synthetic, or artificial, light harvesting systems stand to benefit from both our fields understanding of how to *create* new chromophores along with insight from physical chemists on how to *arrange* these molecules into efficient light harvesting manifolds. Although the field of artificial photosynthesis is vast and encompasses light harvesting, charge separation, and catalysis, for the purposes of this thesis I will only discuss the first step, light harvesting.

Within synthetic light harvesting, two families of molecules first came to the forefront for use as active chromophores, porphyrins and phthalocyanines.[41, 42] Both are planar, conjugated hydrocarbon dye molecules which closely resemble chlorophyll and its derivatives. Long chains of these molecules were some of the earliest test cases for light harvesting due to efficient $\pi \rightarrow \pi^*$ energy transitions. Indeed, this is the same transition which drives exciton

diffusion in organic photovoltaic (OPV) devices.[43] Unfortunately, such simplicity comes at a cost. While this means of exciton diffusion is efficient and effective in pristine samples, any structural defect or break in conjugation can lead to a collapse in device performance.[44] Indeed, the very issue which photosynthesis excels at (namely the spatial manipulation of chromophores to ensure effective exciton transport) is the stumbling block for many emergent technologies.

Spatial funneling also plays an important role within artificial light harvesting media, similar to purple bacteria. Simple arm-like structures towards a 'reaction center' at the center have been employed as well as dendrimeric structures. Similarly, metal coordination compounds utilize metal-to-ligand charge transfer (MLCT) which facilitate low absorption excitation harvesting.[45] In summary, all the photosynthetic design principles outlined in previous sections have been found to play a role in constructing materials with desirable properties. Funneling is used in terms of geometric designs, multiple excitations are used to test robustness, and electronic and exciton-vibrational coupling are used as tools to understand which designs work, and which do not.

1.2.1 Dyes on DNA Scaffolds

Organic dyes (also named molecular dyes elsewhere) on double stranded (ds) DNA scaffolds have emerged as a useful intermediate step between effective synthetic light harvesting materials and biological photosynthesis.[46, 47] The ds-DNA scaffold acts analogously to the protein environment of light harvesting modules of photosynthetic organisms, while chemistry's vast array of dye molecules can function as the photoactive pigments. Many attractive qualities, such as commercial availability, base-pair specificity for placing dyes, and facile solubility, make using ds-DNA scaffolds with dyes an active research area for both applied photonics as well as fundamental properties of energy transfer. B-form DNA is the most common structural base component of dye-DNA structures, and its important features are

Geometry Feature	B-DNA Value
Helix orientation	right-handed
Rotation/bp	34.3°
Base pair separation	3.4 Å
Diameter	20 Å

Table 1.1: Basic geometrical parameters for B-DNA, as reported from [48]

shown in the following table.

The field of DNA based nanotechnology is vast and encompasses research from bio-therepeutics[49] to logical nanocomputing[50]. First emerging during the 1980s,[51] the field has seen a boom in research interest due to the commercial viability and sheer amount of malleability in terms of both the DNA structures themselves as well as the positioning of photonically active media. Figure 1.6 shows the wide array of research interests within DNA nanostructures. A wide variety of material can be conjugated or attached to DNA scaffolds, ranging from small organic dyes to much larger nanocrystals (NCs). Figure 1.6 also displays some of the possibilities using structural DNA nanotechnology, from the simple ds-DNA strands to cubes that can function similarly to construction blocks. Small dye fluorophores can be attached in a variety of ways, namely direct synthetic insertion, intercalation, and the DNA labeling. Direct synthetic insertion occurs at phosphoramidite bases on the DNA and requires a fluorescent analog to bind to it.[52] Modified DNA will display a thiol or other reactive binding site with a complementary fluorophore being used,[53] and intercalation involves native DNA and the insertion of planar dyes between adjacent base pairs.[54, 55]

Beyond fluorescent dyes, larger nanocrystals (NCs) such as quantum dots (QDs) and gold plasmonic NCs have been used to create networks of increasing photonic complexity.[56] These networks often involve multiple domains including FRET-based transfer between fluorescent dyes terminating in a NC. The ability to bind these materials, as well as ds-DNA's intrinsic chiral properties have made the construction of chiral plasmonic materials a possibility.[57]

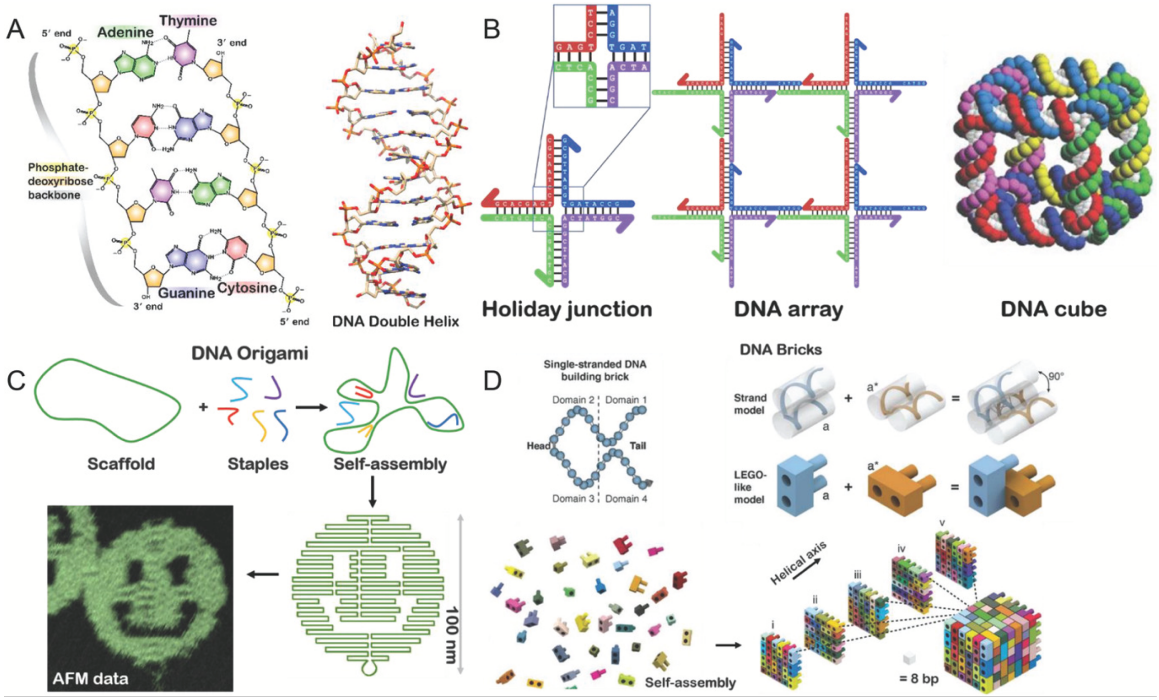

Figure 1.6: (A) Hydrogen bonding dictates the pairing of DNA's bases which forms its well-known double-helix shape. (B) Junctions and aggregates allow for the close tuning of fluorophores and the creation of larger scale cubes. (C) DNA origami creates structures many orders of magnitude greater than a single DNA strand reliably and without added energy. (D) Taking it a step further, smaller repeatable structures can be combined into large-scale constructs through simple addition. Figure from [47] and used with permission within Creative Commons Attribution-NonCommercial 4.0 International (CC BY-NC 4.0) License.

One of the most important areas of DNA nanostructure research, however, is with regards to the attachment of small fluorophores. As the technology has greatly improved since the 1980s, nanometer specificity and great orientational control are now possible. This makes the construction of aggregates and long, highly- efficient molecular photonic wires (MPWs) an area of increased study. MPWs allow for sub-diffraction limit manipulation of light and give repeatable and highly stable structures. These nanostructures can be self-assembled and a wide array of designs are possible. One such design includes a four-arm star which is extended upon in a later chapter. This structure involves long stretches of homoFRET MPWs at blue wavelenghts (around 500 nm), which terminates in a cluster of Cy 6.5 dyes for emission in the NIR.[58]

Although efficiency remains a top concern, these technologies are inherently limited by the very thing that makes them function, FRET. To increase FRET efficiency, distance between fluorophores must decrease, but at a certain point, FRET theory breaks down and the dyes begin to exhibit strongly coupled dynamics which unfortunately includes novel nonradiative traps. This issue is expanded upon in my research into a family of ds-DNA homoFRET MPWs consisting of Cy 5 dyes.

1.2.2 Other Synthetic Systems

Although my research has solely focused on the light harvesting properties of synthetic systems, it is important to emphasize that the initial light harvesting step is only the first step in artificial photosynthesis. Once light has been harvested, it can be transported as a means to produce electrical current through photovoltaic devices, or be used to catalyze reactions through photocatalysis. Both of these aims have strategic strengths and weaknesses.

For photovoltaics, harvesting and harnessing energy has been studeied and optimized, but storage remains an outstanding issue.[59] Renewable battery sources and large-scale electric grid studies have been used to confront this issue, however the crucial factor remains

that batteries are far less dense energetically when compared to chemical fuels.[60, 61] Photocatalysis seeks to use solar energy to drive chemical reactions towards the synthesizing of stable fuel products. Within this artificial photosynthesis (AP) community, issues remain with regards to stability and efficiency of devices.There is also a dearth of fundamental understanding of the photodynamics in these devices, which makes it an intriguing space for physical chemists and ultrafast spectroscopists.

REFERENCES

[1] Robert E. Blankenship, David M. Tiede, James Barber, Gary W. Brudvig, Graham Fleming, Maria Ghirardi, M. R. Gunner, Wolfgang Junge, David M. Kramer, Anastasios Melis, Thomas A. Moore, Christopher C. Moser, Daniel G. Nocera, Arthur J. Nozik, Donald R. Ort, William W. Parson, Roger C. Prince, and Richard T. Sayre. Comparing photosynthetic and photovoltaic efficiencies and recognizing the potential for improvement. *Science*, 332(6031):805–809, 2011.

[2] BP Statistical Review 2019. Statistical review of world energy - all data, 1965-2018. `https://www.bp.com/en/global/corporate/energy-economics/statistical-review-of-world-energy.html`, 2018. [Online; accessed 15-April-2020].

[3] Nathan S. Lewis and Daniel G. Nocera. Powering the planet: Chemical challenges in solar energy utilization. *Proceedings of the National Academy of Sciences*, 103(43):15729–15735, 2006.

[4] Jorge Davila, Anthony Harriman, and Lionel R. Milgrom. A light-harvesting array of synthetic porphyrins. *Chemical Physics Letters*, 136(5):427 – 430, 1987.

[5] Douglas J. Orr, Auderlan M. Pereira, Paula da Fonseca Pereira, Ítalo A. Pereira-Lima, Agustin Zsögön, and Wagner L. Araújo. Engineering photosynthesis: progress and perspectives. *F1000Research*, 6:1891–1891, 2017.

[6] Lili Wang, Marco A. Allodi, and Gregory S. Engel. Quantum coherences reveal excited-state dynamics in biophysical systems. *Nature Reviews Chemistry*, 3(8):477–490, 2019.

[7] Peter D. Dahlberg, Po-Chieh Ting, Sara C. Massey, Elizabeth C. Martin, C. Neil Hunter, and Gregory S. Engel. Electronic structure and dynamics of higher-lying excited states in light harvesting complex 1 from rhodobacter sphaeroides. *The Journal of Physical Chemistry A*, 120(24):4124–4130, 2016.

[8] Brian S. Rolczynski, Haibin Zheng, Ved P. Singh, Polina Navotnaya, Alan R. Ginzburg, Justin R. Caram, Khuram Ashraf, Alastair T. Gardiner, Shu-Hao Yeh, Sabre Kais, Richard J. Cogdell, and Gregory S. Engel. Correlated protein environments drive quantum coherence lifetimes in photosynthetic pigment-protein complexes. *Chem*, 4(1):138 – 149, 2018.

[9] David J. Lockwood. *Rayleigh and Mie Scattering*, pages 1097–1107. Springer New York, New York, NY, 2016.

[10] Miroslaw Jonasz and Georges R. Fournier. Chapter 4 - measurements of light scattering by particles in water. In Miroslaw Jonasz and Georges R. Fournier, editors, *Light Scattering by Particles in Water*, pages 145 – 265. Academic Press, Amsterdam, 2007.

[11] Wikimedia Commons. File:solar spectrum.png — Wikimedia Commons, the free media repository. `https://commons.wikimedia.org/w/index.php?title=File:Solar_Spectrum.png&oldid=369356051`, 2019. [Online; accessed 13-May-2020].

[12] Robert E. Blankenship. *Molecular Mechanisms of Photosynthesis*. John Wiley& Sons, Ltd, Chinchester, West Sussex, 2nd edition, 2014.

[13] Olle Björkman. Chapter 1 - comparative studies on photosynthesis in higher plants**ciw dpb publication no. 492. In Arthur C. Giese, editor, *Photophysiology*, pages 1 – 63. Academic Press, 1973.

[14] Dmitry Shevela, Lars Olof Bjorn, and Govindjee. Oxygenic photosynthesis. pages 13–63, 2013.

[15] Christoph Kreisbeck and Alán Aspuru-Guzik. Efficiency of energy funneling in the photosystem ii supercomplex of higher plants. *Chem. Sci.*, 7:4174–4183, 2016.

[16] C. Neil Hunter, Jamey D. Tucker, and Robert A. Niederman. The assembly and organisation of photosynthetic membranes in rhodobacter sphaeroides. *Photochem. Photobiol. Sci.*, 4:1023–1027, 2005.

[17] Andrew F. Fidler, Ved P. Singh, Phillip D. Long, Peter D. Dahlberg, and Gregory S. Engel. Probing energy transfer events in the light harvesting complex 2 (lh2) of rhodobacter sphaeroides with two-dimensional spectroscopy. *The Journal of Chemical Physics*, 139(15):155101, 2013.

[18] Marco A. Allodi, John P. Otto, Sara H. Sohail, Rafael G. Saer, Ryan E. Wood, Brian S. Rolczynski, Sara C. Massey, Po-Chieh Ting, Robert E. Blankenship, and Gregory S. Engel. Redox conditions affect ultrafast exciton transport in photosynthetic pigment–protein complexes. *The Journal of Physical Chemistry Letters*, 9(1):89–95, 2018. PMID: 29236502.

[19] Villy Sundström, Tõnu Pullerits, and Rienk van Grondelle. Photosynthetic light-harvesting: Reconciling dynamics and structure of purple bacterial LH2 reveals function of photosynthetic unit. *The Journal of Physical Chemistry B*, 103(13):2327–2346, 1999.

[20] Sergei Tretiak, Chris Middleton, Vladimir Chernyak, and Shaul Mukamel. Exciton hamiltonian for the bacteriochlorophyll system in the lh2 antenna complex of purple bacteria. *The Journal of Physical Chemistry B*, 104(18):4519–4528, 2000.

[21] Sara C. Massey, Po-Chieh Ting, Shu-Hao Yeh, Peter D. Dahlberg, Sara H. Sohail, Marco A. Allodi, Elizabeth C. Martin, Sabre Kais, C. Neil Hunter, and Gregory S. Engel. Orientational dynamics of transition dipoles and exciton relaxation in lh2 from ultrafast two-dimensional anisotropy. *The Journal of Physical Chemistry Letters*, 10(2):270–277, 2019.

[22] O. N. Lebedeva, A. F. Titov, E. B. Stafeeva, and T. S. Nikolaevskaya. Photoprotection strategy in higher plants. *Russian Agricultural Sciences*, 33(4):229–232, 2007.

[23] Erling Thyrhaug, Craig N. Lincoln, Federico Branchi, Giulio Cerullo, Václav Perlík, František Šanda, Heiko Lokstein, and Jürgen Hauer. Carotenoid-to-bacteriochlorophyll energy transfer through vibronic coupling in lh2 from phaeosprillum molischianum. *Photosynthesis Research*, 135(1):45–54, 2018.

[24] Thomas Renger and Volkhard May. Theory of multiple exciton effects in the photosynthetic antenna complex lhc-ii. *The Journal of Physical Chemistry B*, 101(37):7232–7240, 1997.

[25] Diana Kirilovsky and Cheryl A. Kerfeld. The orange carotenoid protein: a blue-green light photoactive protein. *Photochem. Photobiol. Sci.*, 12:1135–1143, 2013.

[26] Adjele Wilson, James N. Kinney, Petrus H. Zwart, Claire Punginelli, Sandrine D'Haene, François Perreau, Michael G. Klein, Diana Kirilovsky, and Cheryl A. Kerfeld. Structural determinants underlying photoprotection in the photoactive orange carotenoid protein of cyanobacteria. *The Journal of biological chemistry*, 285(24):18364–18375, 2010.

[27] Peter D. Dahlberg, Po-Chieh Ting, Sara C. Massey, Marco A. Allodi, Elizabeth C. Martin, C. Neil Hunter, and Gregory S. Engel. Mapping the ultrafast flow of harvested solar energy in living photosynthetic cells. *Nature Communications*, 8(1):988, 2017.

[28] W. Arnold and J. R. Oppenheimer. Internal conversion in the photosynthetic mechanism of blue-green algae. *The Journal of general physiology*, 33(4):423–435, 1950.

[29] Melih Şener, Johan Strümpfer, Jen Hsin, Danielle Chandler, Simon Scheuring, C. Neil Hunter, and Klaus Schulten. Förster energy transfer theory as reflected in the structures of photosynthetic light-harvesting systems. *Chemphyschem : a European journal of chemical physics and physical chemistry*, 12(3):518–531, 2011.

[30] Th. Förster. Zwischenmolekulare energiewanderung und fluoreszenz. *Annalen der Physik*, 437(1-2):55–75, 1948.

[31] Joshua A. Broussard, Benjamin Rappaz, Donna J. Webb, and Claire M. Brown. Fluorescence resonance energy transfer microscopy as demonstrated by measuring the activation of the serine/threonine kinase akt. *Nature Protocols*, 8(2):265–281, 2013.

[32] E. Sobakinskaya, M. Schmidt Am Busch, and T. Renger. Theory of fret "spectroscopic ruler" for short distances: Application to polyproline. *J Phys Chem B*, 122(1):54–67, 2018.

[33] Björn Hellenkamp, Philipp Wortmann, Florian Kandzia, Martin Zacharias, and Thorsten Hugel. Multidomain structure and correlated dynamics determined by self-consistent fret networks. *Nature Methods*, 14(2):174–180, 2017.

[34] John M. Jean, Richard A. Friesner, and Graham R. Fleming. Application of a multilevel redfield theory to electron transfer in condensed phases. *The Journal of Chemical Physics*, 96(8):5827–5842, 1992.

[35] M. Sener R.M. Clegg and Govindjee. From foerster resonance energy transfer to coherent resonance energy transfer and back (invited paper). *Proceedings of SPIE*, 7561:21, 2010.

[36] Hong-Guang Duan, Valentyn I. Prokhorenko, Richard J. Cogdell, Khuram Ashraf, Amy L. Stevens, Michael Thorwart, and R. J. Dwayne Miller. Nature does not rely on long-lived electronic quantum coherence for photosynthetic energy transfer. *Proceedings of the National Academy of Sciences*, 114(32):8493–8498, 2017.

[37] Alexandra Olaya-Castro and Gregory D. Scholes. Energy transfer from förster–dexter theory to quantum coherent light-harvesting. *International Reviews in Physical Chemistry*, 30(1):49–77, 2011.

[38] Tzu-Chi Yena and Yuan-Chung Cheng. Electronic coherence effects in photosynthetic light harvesting. *Procedia Chemistry*, 3(1):211 – 221, 2011. 22nd Solvay Conference on Chemistry.

[39] Seogjoo Jang, Yuan-Chung Cheng, David R. Reichman, and Joel D. Eaves. Theory of coherent resonance energy transfer. *The Journal of Chemical Physics*, 129(10):101104, 2008.

[40] D. L. Dexter. A theory of sensitized luminescence in solids. *The Journal of Chemical Physics*, 21(5):836–850, 1953.

[41] Kenji Sugou, Ken Sasaki, Koji Kitajima, Toru Iwaki, and Yasuhisa Kuroda. Light-harvesting heptadecameric porphyrin assemblies. *Journal of the American Chemical Society*, 124(7):1182–1183, 2002.

[42] Mohamed E. El-Khouly. Energy transfer between two light harvesting phthalocyanine derivatives as model for artificial photosynthetic antenna: Laser photolysis studies. *Spectrochimica Acta Part A: Molecular and Biomolecular Spectroscopy*, 205:508 – 513, 2018.

[43] Lei Zhu, Min Wang, Bowen Li, Chao Jiang, and Qifang Li. High efficiency organic photovoltaic devices based on isoindigo conjugated polymers with a thieno[3,2-b]thiophene pi-bridge. *J. Mater. Chem. A*, 4:16064–16072, 2016.

[44] Jiefei Wang, Yong Zhong, Liang Wang, Na Zhang, Ronghui Cao, Kaifu Bian, Leanne Alarid, Raid E. Haddad, Feng Bai, and Hongyou Fan. Morphology-controlled synthesis and metalation of porphyrin nanoparticles with enhanced photocatalytic performance. *Nano Letters*, 16(10):6523–6528, 2016. PMID: 27617350.

[45] Xianyong Wang, Andre Del Guerzo, Sujoy Baitalik, Gerald Simon, George B. Shaw, Lin X. Chen, and Russell Schmehl. The influence of bridging ligand electronic structure

on the photophysical properties of noble metal diimine and triimine light harvesting systems. *Photosynthesis Research*, 87(1):83–103, 2006.

[46] Fan Hong, Fei Zhang, Yan Liu, and Hao Yan. Dna origami: Scaffolds for creating higher order structures. *Chemical Reviews*, 117(20):12584–12640, 2017. PMID: 28605177.

[47] Hieu Bui, Sebastián A. Díaz, Jake Fontana, Matthew Chiriboga, Remi Veneziano, and Igor L. Medintz. Utilizing the organizational power of dna scaffolds for new nanophotonic applications. *Advanced Optical Materials*, 7(18):1900562, 2019.

[48] Richard E Dickerson. [5] dna structure from a to z. In *DNA Structures Part A: Synthesis and Physical Analysis of DNA*, volume 211 of *Methods in Enzymology*, pages 67 – 111. Academic Press, 1992.

[49] Muniza Zahid, Byeonghoon Kim, Rafaqat Hussain, Rashid Amin, and Sung Ha Park. Dna nanotechnology: a future perspective. *Nanoscale research letters*, 8(1):119–119, 2013.

[50] Tianqi Song, Abeer Eshra, Shalin Shah, Hieu Bui, Daniel Fu, Ming Yang, Reem Mokhtar, and John Reif. Fast and compact dna logic circuits based on single-stranded gates using strand-displacing polymerase. *Nature Nanotechnology*, 14(11):1075–1081, 2019.

[51] Nicholas E. Geacintov, Jurg Waldmeyer, Vladimir A. Kuzmin, and Tatiana Kolubayev. Dynamics of the binding of acridine dyes to dna investigated by triplet excited state probe techniques. *The Journal of Physical Chemistry*, 85(24):3608–3613, 1981.

[52] Venkatesan Natarajan, Kim Su Jeong, and Kim Byeang Hyean. Novel phosphoramidite building blocks in synthesis and applications toward modified oligonucleotides. *Current Medicinal Chemistry*, 10(19):1973–1991, 2003.

[53] Lorenzo Berti, Jin Xie, Igor L. Medintz, Alexander N. Glazer, and Richard A. Mathies. Energy transfer cassettes for facile labeling of sequencing and pcr primers. *Analytical Biochemistry*, 292(2):188 – 197, 2001.

[54] Haukur Gudnason, Martin Dufva, D.D. Bang, and Anders Wolff. Comparison of multiple DNA dyes for real-time PCR: effects of dye concentration and sequence composition on DNA amplification and melting temperature. *Nucleic Acids Research*, 35(19):e127–e127, 09 2007.

[55] Alexander N. Glazer and Hays S. Rye. Stable dye–dna intercalation complexes as reagents for high-sensitivity fluorescence detection. *Nature*, 359(6398):859–861, 1992.

[56] J. Christopher Love, Lara A. Estroff, Jennah K. Kriebel, Ralph G. Nuzzo, and George M. Whitesides. Self-assembled monolayers of thiolates on metals as a form of nanotechnology. *Chemical Reviews*, 105(4):1103–1170, 2005. PMID: 15826011.

[57] Alexander J. Mastroianni, Shelley A. Claridge, and A. Paul Alivisatos. Pyramidal and chiral groupings of gold nanocrystals assembled using dna scaffolds. *Journal of the American Chemical Society*, 131(24):8455–8459, 2009. PMID: 19331419.

[58] William P. Klein, Sebastián A. Díaz, Susan Buckhout-White, Joseph S. Melinger, Paul D. Cunningham, Ellen R. Goldman, Mario G. Ancona, Wan Kuang, and Igor L. Medintz. Utilizing homofret to extend dna-scaffolded photonic networks and increase light-harvesting capability. *Advanced Optical Materials*, 6(1):1700679, 2018.

[59] A. Chaurey and S. Deambi. Battery storage for pv power systems: An overview. *Renewable Energy*, 2(3):227 – 235, 1992.

[60] Iain McConnell, Gonghu Li, and Gary W. Brudvig. Energy conversion in natural and artificial photosynthesis. *Chemistry and biology*, 17(5):434–447, 2010.

[61] Biaobiao Zhang and Licheng Sun. Artificial photosynthesis: opportunities and challenges of molecular catalysts. *Chem. Soc. Rev.*, 48:2216–2264, 2019.

CHAPTER 2

EXPERIMENTAL METHODS IN ULTRAFAST SPECTROSCOPY

2.1 Overview

The use of ultrafast spectroscopy to study the variety of biological and material samples is only possible due to the theoretical framework given it from time-dependent quantum mechanics and statistical mechanics. Although a full treatment is not the aim of this section, basic tenets and formalisms will be presented to explain design implementations in the laser lab. My research was evenly distributed between pump-probe and two dimensional electronic spectroscopy (2DES), so I will first present the formalisms of a third-order four-wave-mixing experiment and then delve into the experimental attributes of each experiment. This chapter will then conclude with a brief section concerning data workup and analysis.

2.2 Theory of Nonlinear and Ultrafast Spectroscopy

2.2.1 Time-Dependent Quantum Mechanics

The study of complex materials using spectroscopy necessitated the development of two fields, time-dependent quantum mechanics and statistical mechanics. In condensed phase systems, samples for study will necessarily be an ensemble, which is most efficiently treated with statistical mechanics. The light-matter interaction which defines spectroscopy can only formally be treated with an understanding of time-dependent quantum mechanics. The central equation for time-dependent quantum mechanics is the time-dependent Schrödinger Equation[1]

$$i\hbar\frac{d}{dt}|\Psi\rangle = \widehat{H}|\Psi\rangle \tag{2.1}$$

where $\widehat{H}$ is the Hamiltonian operator of the system and Ψ is the overall wave-function of the system. To analyze this equation, it is necessary to first understand the time-independent Schrödinger Equation, where molecular eigenstates $|n\rangle$ of $\widehat{H}_0$ are found by solving

$$\widehat{H}_0|n\rangle = E_n|n\rangle. \tag{2.2}$$

When subject to no laser pulse, the solution to the time-dependent Schrödinger Equation is

$$|\Psi(t)\rangle = \sum_n c_n e^{-iE_n t/\hbar}|n\rangle. \tag{2.3}$$

When there is a laser pulse hitting a sample, the Gaussian pulse-shape of light (or a Gaussian perturbation) constructs a coherent linear superposition of states within the molecule which has its own time dependence, which is called the molecular response, $R(t)$. When there are multiple molecular responses in phase with one another (such as from excitation *via* a laser pulse), the phenomenon of this collective behavior and its subsequent dynamics are known as the macroscopic polarization, $P(t)$. We can now begin to treat our system, Ψ, with a laser pulse, $E(t)$. A simplified laser pulse is given by the following equation:

$$E(t) = E'(t)cos(\omega t) \tag{2.4}$$

where $E'(t)$ is the pulse envelope function. Spectroscopy is the relation between the electric field and the molecular dipole, so we can write an interaction operator for the light matter interaction

$$\widehat{I}(t) = -\widehat{\mu}E(t) \tag{2.5}$$

where $\widehat{\mu}$ is the dipole operator. From here, following conventional quantum mechanics, we could calculate an expectation value of the transition dipole operator acting on our sample in a time dependent way, revealing the macroscopic polarization. The following equation

shows this formalism:

$$P(t) = \langle \mu \rangle = \langle \Psi(t) | \widehat{\mu} | \Psi(t) \rangle \tag{2.6}$$

which can be analytically written using equation 2.3 and assuming that the molecule can be expressed as a linear combination of eigenstates $|a\rangle$ and $|b\rangle$, a more complete macroscopic polarization can be written as

$$\begin{aligned} P(t) &= (c_a e^{iE_a t/\hbar} \langle a| - i c_b e^{iE_b t/\hbar} \langle b|) \widehat{\mu} (c_z e^{-iE_a t/\hbar} |a\rangle + i c_b e^{-1E_b t/\hbar} |b\rangle \\ &= c_a c_b \langle a|\widehat{\mu}|b\rangle sin(\omega_{ab} t) + {c_a}^2 \langle a|\widehat{\mu}|a\rangle + {c_b}^2 \langle b|\widehat{\mu}|b\rangle \end{aligned} \tag{2.7}$$

where ω_{ab} is defined as $\frac{E_a - E_b}{\hbar}$. Also, c_a and c_b are the coefficients representing population in the $|a\rangle$ and $|b\rangle$ states respectively.

2.2.2 Density Matrices

As shown, it quickly becomes difficult to treat our system as a state vector because it can be acted on by many operators and have many statistical states (including mixed state) possible. For this reason, when talking about three pulse experiments, the density matrix formalism has been adopted to describe the statistical state of a system, which in our case is the non-linear response function of our sample. The elements of a density matrix are defined by the following equation:

$$\rho = \sum_{i,j} p_{ij} |\psi_i\rangle \langle \psi_j| \tag{2.8}$$

where the probability of element $|\psi_i\rangle\langle\psi_j|$ is accordingly givein by p_{ij}. Some fundamental properties of density matrices include normalization, $Tr(\rho) = 1$, and being Hermitian, $\rho_{ij} =$

ρ_{ij}^* . The expectation value of an operator is likewise calculated by taking the trace:

$$\langle \widehat{A} \rangle = Tr(\widehat{\rho}\widehat{A}) \tag{2.9}$$

Time dependence is introduced to the treatment of a density matrix by taking the derivative of a density matrix in a basis representation, yielding two terms:

$$\dot{\rho}_{ij} = \sum_k \frac{dp_k}{dt} c_i {c_j}^* - \frac{i}{\hbar}[\widehat{H}, \rho]_{ij} \tag{2.10}$$

where the first term represents the statistical mechanical treatment of density matrices and leads to population relaxation and dephasing (controlled by off-diagonal elements of a density matrix) and the second term leads to the *Liouville-von Neumann equation*, which ends up being one of the central constructs in time-dependent perturbation theory.

A full treatment of time-dependent perturbation theory is beyond the scope of this thesis, but a more detailed mathematical treatment can prove useful when trying to theoretically model nonlinear events in spectroscopy. One of the most complete treatments can be found in Professor Shaul Mukamel's book, *Principles of Non-linear Optical Spectroscopy*, [2], while other sources such as *Concepts and Methods of 2D Infrared Spectroscopy*[1] and Professor Andrei Tokmakoff's online notes on nonlinear spectroscopy[3] provide a more curated approach towards the experimentalist in this admittedly dense topic.

2.2.3 Time-Dependent Perturbation Theory

The central equations needed to mathematically depict a non-linear spectroscopy experiment are the polarization and response function. The macroscopic polarization, which is the observable we are after, is found by calculating the expectation value of the dipole operator $\widehat{\mu}$,

$$P(t) = Tr(\widehat{\mu}\rho(t)) = \langle\widehat{\mu}\rho(t)\rangle \tag{2.11}$$

and the $n^t h$-order polarization is given by:

$$P^{(n)}(t) = \langle\widehat{\mu}\rho^{(n)}(t)\rangle \tag{2.12}$$

where $\rho^{(n)}$ is the $n^t h$-order density matrix created by perturbatively expanding in the interaction picture. The end result is that for light-matter interactions taking place at times $\{t_1, t_2, t_3\}$ the third-order polarization is:

$$P^{(3)}(t) \propto \int_0^\infty dt_3 \int_0^\infty dt_2 \int_0^\infty dt_1 E_3(t-t_3)E_2(t-t_3-t_2)\cdot E_1(t-t_3-t_2-t_1)\cdot R^{(3)}(t_1,t_2,t_3) \tag{2.13}$$

where

$$R^{(3)}(t_1,t_2,t_3) \propto -i\langle\widehat{\mu}(t_3+t_2+t_1)[\widehat{\mu}(t_2+t_1),[\widehat{\mu}(t_1,[\widehat{\mu}(0),\rho(-\infty)]]]\rangle. \tag{2.14}$$

2.2.4 Feynman Diagrams

This mathematical treatment has the array of timings and laser pulses (represented by electric field $E(t)$) necessary to explain ultrafast experiments. It however obscures the range of interactions that can occur during a four-pulse experiment. To make the interactions of light and matter during a multipulse experiment more clear, Feynman diagrams are used, which in a ladder-like manner illustrate the passing of time as demarcated by light matter interactions. Momentum is seen by the direction at which the arrows are pointing, and the status of the system at each moment is seen through the use of *ket* and *bra* components of the density matrix.

A brief enumeration of conventions for reading and drawing Feynman diagrams follows, which is adapted from [1].

1. The left and right vertical bars represent time evolution which passes in the upwards direction. Horizontal rungs represent time points when light matter interactions occur.

2. The electric fields creating the light matter interactions themselves are represented by arrows, where an arrow heading from left-to-right has positive wave-vector and phase, whereas the opposite is true for arrows heading from the right-to left.

3. Excitation into the system is represented by an inwards arrow while de-excitation is represented by an outwards pointing arrow.

4. A population state (in the case of a two state system, when either $|0\rangle\langle 0|$ or $|1\rangle\langle 1|$) must be the final state, and it must be preceded by an emission.

Figure 2.1 shows six primary Feynman pathways, with arrows showing the progression of time on the left. These pathways are divided into nonrephasing and rephasing pathways, and are differentiated by whether phase is continued to be acquired in the same direction or reversed during time periods τ and t. Whereas a photon echo is emitted following rephasing time, a free induction decay will be emitted at $t = 0$ in a nonrephasing pathway. In most cases, experimentally, it is useful to convert to from absolute time $\{t_0 \rightarrow t_3\}$ to relative time $\{\tau, T, t\}$ as this gives the time evolution of each state. These three time periods are named coherence time, waiting time, and rephasing time respectively and are shown in the lower arrow in Figure 2.1.

In certain techniques that focus to lines rather than a point (such as GRadient Assisted Photon Echo Spectroscopy, GRAPES),[4][5] the issue of independently acquiring, phasing, and analyzing these different types of signal is much more important than in a typical point-by-point BoxCARS setup.

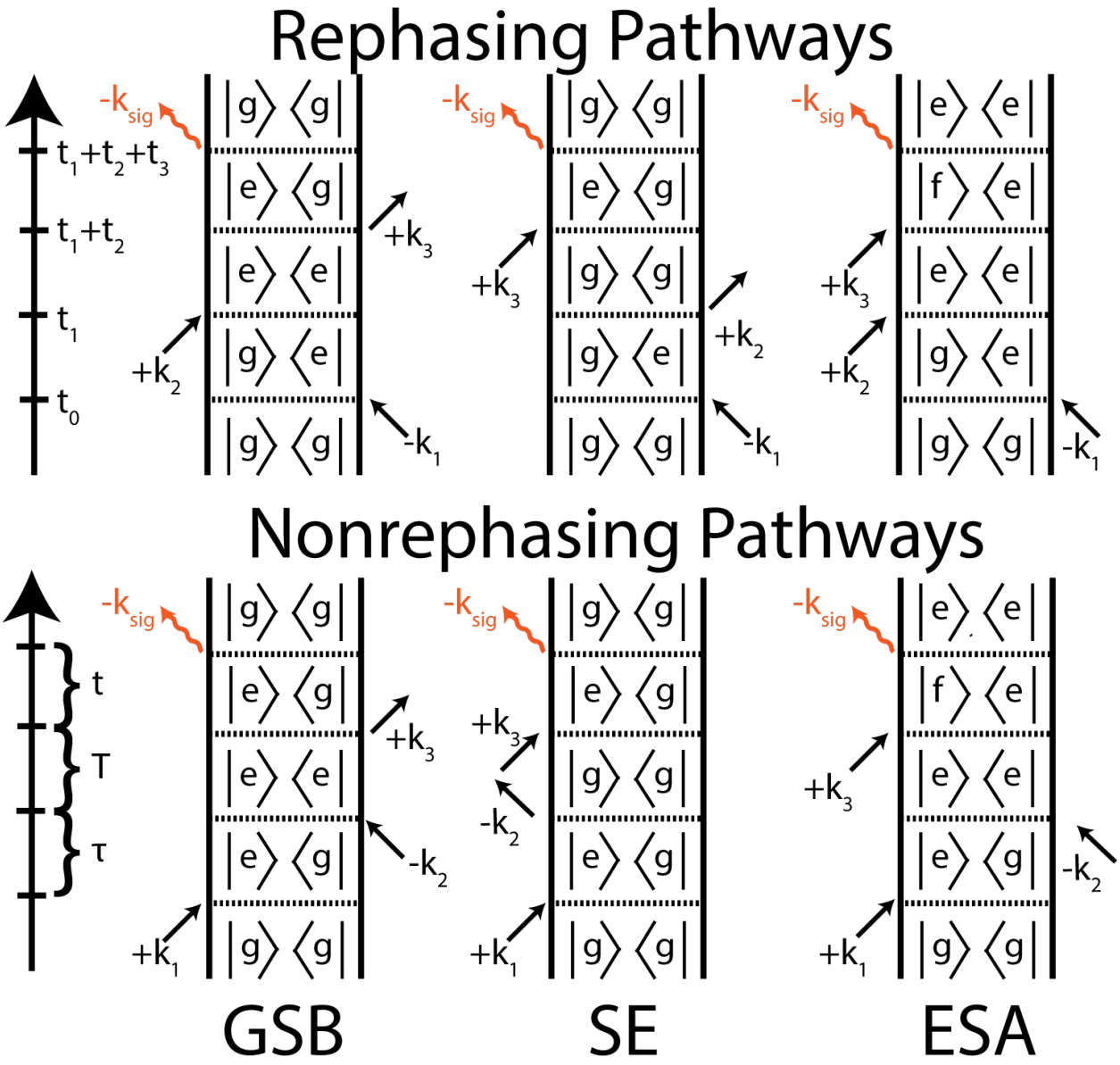

Figure 2.1: (Top) Rephasing pathways that emit a photon echo (Bottom) Nonrephasing pathways which result in a free-induction decay (Left) Ground state bleach pathways, in which an evacuated ground state population is allowed to evolve during waiting time T (Center) Stimulated emission pathways, also a positive pathway and distinguishable from GSB only through waiting time dynamics. (Right) Excited state absorption pathways, in which an excited state is probed. Yields a negative signal.

2.3 Experimental Realization of Two-Dimensional and Pump-Probe Spectroscopy

To experimentally achieve ultrafast spectroscopy, the requirement is to have laser pulses as close to the impulsive limit (as in, their duration is instantaneous) as possible. To achieve this, broadband laser pulses are used due to the Fourier relationship between time and energy. Broadband pulses have the additional benefit of exciting a broad manifold of states, making it possible to excite and probe many electronic states in our systems.

A second requirement is to have precise control over the timing of these pulses. Two-dimensional spectra, as well as pump-probe spectra, are built as arrays of different timings: $\{\tau, T, t\}$, and the coherence and rephasing time series are Fourier transformed to give the excitation and detection axes which constitute a traditional 2D heat-map. Waiting time itself is preserved as a time series typically, although it can also be Fourier transformed over to provide a 'beat map,' which shows any vibrational beating during the waiting time. This fine control over timings is achieved using optomechanical delay lines which can achieve femtosecond precision over laser pulses due to the fact that light travels in air at a known speed.[6] Light travels approximately $300nm/fs$, so having reliable coverage of 5 nm gives single-digit femtosecond control. An additional requirement is of course repeatability, which these optomechanical delay lines are also able to achieve.

All three beams, along with a fourth beam called the local oscillator (LO) are focused onto the sample from a 'box'-like shape, where the signal emerges in the direction of the local osciallator, as predicted by the conservation of momentum. As the signal emits at a direction absent the other beams, 2D in a BOXCARS geometry is said to be background free.[7] This is in stark contrast to pump-probe spectroscopy, where the signal will emit in the direction of the probe beam, so subtraction from the actual camera image needs to take place to get a full read on the data. Signal detection in 2DES is acquired on a commercially available spectrometer and CCD camera. First the signal and LO are passed through a slit

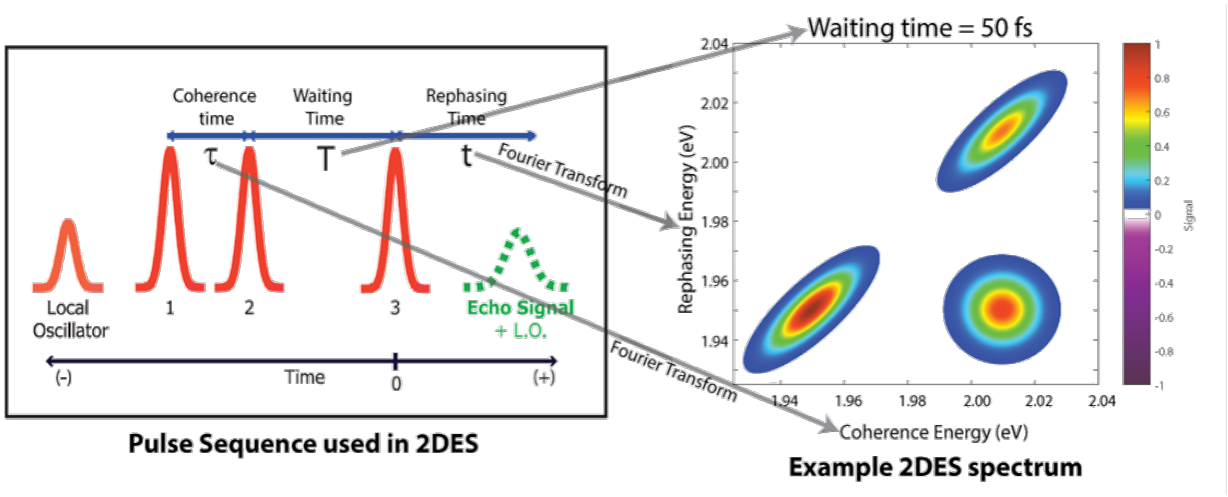

Figure 2.2: Mock 2D spectrum pointing out the Fourier pairs of Coherence Time with the horizontal axis and Rephasing Time with the vertical axis. Positive and negative signals are possible in 2D, although using the BOXCARS geometry requires phasing.

so as to reduce the amount of stray light enterring the spectrometer, then they are dispersed by a grating before being captured by pixels of the CCD camera. The signal and oscillator create an interferogram across frequency and this image is then saved. A new time delay is chosen (generally a spectrum at one waiting time will be taken before moving on to the next waiting time) and the process repeats itself.

Figure 2.2 shows a mock 2D spectrum. Important features of 2DES spectra include on-diagonal features, which represent energy-in being the same as energy-out, off-diagonal features represent some coupling between excited states, such as excited state absorption (ESA) or an energy transfer feature. Line width analysis also plays an important role within 2DES data analysis, as static variation in the sample can lead to broader signals along the diagonal. This would mean that there exist permanent subpopulations contributing to this broader signal. When spectral features do not feature such an elongation, this is referred to as homogenous broadening. In this case, environmental factors lead to the wider distribution of energy. [8]

Each point of a 2D spectrum, (ω_τ, ω_t), can reveal a waiting time trace. In this case, the

magnitude of that point is plotted against the waiting time slice it came from. Analysis of these traces can reveal energy transfer dynamics, ground state bleach recovery, and other dynamics. [9, 10] Line shape analysis also enables for measurements such as center line slope (CLS) analysis which allows for a closer look at frequency-frequency correlation as well as system-bath interactions.[11]

All of my ultrafast experiments were conducted on a point-by-point all reflective 2D spectrometer and pump-probe spectrometer as outlined by Zheng et al.[12]. Ultrafast pulses are generated in a commercial Coherent Legend Elite system using the chirped pulse amplification technique developed by Maine et al.[13]. Upon exiting the apparatus, the 5 kHz pulse train, centered at 800 nm and with a 38 fs pulse width, is focused into a 2-m-long tube of argon, where it undergoes self-phase modulation to produce a supercontinuum of light ranging from 500 nm to 900 nm.[14] Self-phase modulation is a uniquely non-linear optical effect which occurs when optical pulses propagate through dispersive, non-linear media.

A pulse emerging from a tube of Argon will be quite messy with respect to dispersion, so it is compressed trimmed using an optical filter and compressed using a pulse shaper, in our case a MIIPS made by Biophotonics Inc. Pulse-widths will typically be around 9 fs at the sample of our spectrometers, described in Fig 2.3.

2.4 Data Analysis in 2DES and Pump-Probe Spectroscopy

Data acquired on the CCD comes in the form of a wavelength-resolved plot which relates to the Rephasing Frequency axis of the final 2D plot. The first step of 2D data analysis is to Fourier Transform this Rephasing Frequency axis into a Rephasing Time axis. Once this has been achieved, a (τ, T, t) cube is seen and scatter can be subtracted by signal windowing. There are many resources on signal processing,[15, 16, 17] but our basic tenet is weighing on one hand the ability to create high-quality spectra while on the other not wanting to clip signal or manipulate the data.

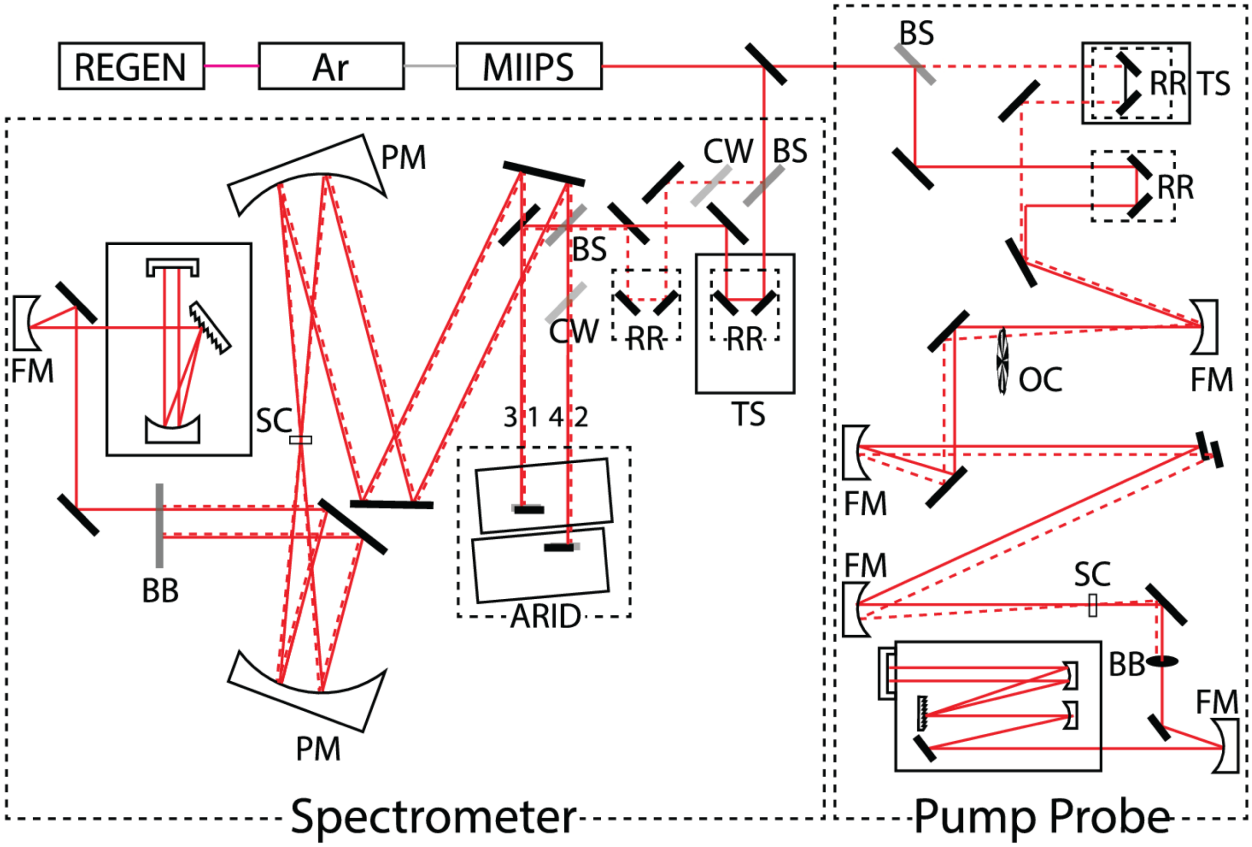

Figure 2.3: Following ejection from the MIIPS, for 2D, ultrafast pulses are split into four pulses by beam splitters (BS) and compensating glass (CW) is used to compensate for differing amounts of material dispersion. Retro-reflectors (RR) ensure that a beam will exit and enter a translation stage (TS) on the translation axis, to prevent walking. The innovation of this all-reflective design is the all-reflective interferometric delay system (ARID), which allows for sub-femtosecond precision in timing delay. Off-axis parabolic mirrors (PM) focus and collimate the beams before and after the sample cell (SC) respectively. Beam blocks block all pulses except for the emitted signal and the local oscillator. In pump-probe, a 90:10 beam splitter sends the pump (dashed) and much less powerful probe in different paths. The pump is sent to a delay line and eventually is sent through an optical chopper (OC), which allows for acquisition of probe-only spectra on every other laser shot. Pump and probe beams are focused onto a sample and signal along with the probe pulse are sent to a line scan camera. Figure adapted from [12] with permission.

Once 2D data has been processed, much analysis such as the methods prescribed above can follow, however, since our spectra are acquired in the BOXCARS geometry, they lose phase information and therefore need to be phased through independently acquired pump-probe. Fortunately, pump-probe is a much faster measurement compared to 2D, taking as little as 30 minutes to capture a full waiting time scan compared to 8 hours for 2D. Likewise, pump-probe data is fairly straight forward to process compared to 2D. For short time scans (for example, anything under a picosecond, e.g. waiting time from 0 to 1000 fs in steps of 10 fs) scatter can be used to find exact timings and signal can be windowed in the optical frequency domain. Otherwise, full pump-probe spectra are constructed fairly directly from the raw data.

Phasing itself involves the mapping a summed representation of the 2D data (which is summed onto the rephasing axis) to the pump-probe data. The theory behind this transformation comes from the Projection Slice Theorem, which is used in many medical imaging techniques such as CT scans.[18] The equation governing the Projection-Slice Theorem essentially states that the Fourier transform of a projection is the same as a slice of a higher dimensional Fourier transform, or put mathematically:

$$F_1 P_1 = S_1 F_2 \tag{2.15}$$

for a two-dimensional image, where F_1 and F_2 are one- and two-dimensional Fourier Transforms, respectively. For our case what this means is that a projection of the 2D spectrum should be matched to the slice of the corresponding pump-probe data. Many phasing algorithms exist in the literature,[19] and the uncertainty and time-sink of phasing makes 2DES in the pump-probe geometry an attractive alternative to the classic BOXCARS geometry.[20]

REFERENCES

[1] Peter Hamm and Martin Zanni. Concepts and methods of 2D infrared spectroscopy. 2011.

[2] S. Mukamel. Principles of nonlinear optical spectroscopy. 1995.

[3] Andrei Tokmakoff. Nonlinear spectroscopy. `http://tdqms.uchicago.edu/page/nonlinear-and-two-dimensional-spectroscopy-notes`, 2011.

[4] V. P. Singh, A. F. Fidler, B. S. Rolczynski, and G. S. Engel. Independent phasing of rephasing and non-rephasing 2d electronic spectra. *The Journal of Chemical Physics*, 139(8):084201, 2013.

[5] Sara H. Sohail, Peter D. Dahlberg, Marco A. Allodi, Sara C. Massey, Po-Chieh Ting, Elizabeth C. Martin, C. Neil Hunter, and Gregory S. Engel. Communication: Broad manifold of excitonic states in light-harvesting complex 1 promotes efficient unidirectional energy transfer in vivo. *The Journal of Chemical Physics*, 147(13):131101, 2017.

[6] H. Fizeau. The hypotheses relating to the luminous aether, and an experiment which appears to demonstrate that the motion of bodies alters the velocity with which light propagates itself in their interior. *Philosophical Magazine*, 2:245–260, 1851.

[7] B.D. Guenther and D. Steel. *Encyclopedia of Modern Optics*. Elsevier Science, 2018.

[8] A. Nitzan and Oxford University Press. *Chemical Dynamics in Condensed Phases: Relaxation, Transfer and Reactions in Condensed Molecular Systems*. Oxford Graduate Texts. OUP Oxford, 2006.

[9] S.E. Morgan. *Ultrafast Quantum Effects and Vibrational Dynamics in Organic and Biological Systems*. Springer Theses. Springer International Publishing, 2017.

[10] T. Buckup and J. Léonard. *Multidimensional Time-Resolved Spectroscopy*. Topics in Current Chemistry Collections. Springer International Publishing, 2018.

[11] František Šanda, Václav Perlík, Craig N. Lincoln, and Jürgen Hauer. Center line slope analysis in two-dimensional electronic spectroscopy. *The Journal of Physical Chemistry A*, 119(44):10893–10909, 2015. PMID: 26463085.

[12] Haibin Zheng, Justin R. Caram, Peter D. Dahlberg, Brian S. Rolczynski, Subha Viswanathan, Dmitriy S. Dolzhnikov, Amir Khadivi, Dmitri V. Talapin, and Gregory S. Engel. Dispersion-free continuum two-dimensional electronic spectrometer. *Appl. Opt.*, 53(9):1909–1917, Mar 2014.

[13] P. Maine, D. Strickland, P. Bado, M. Pessot, and G. Mourou. Generation of ultrahigh peak power pulses by chirped pulse amplification. *IEEE Journal of Quantum Electronics*, 24(2):398–403, 1988.

[14] R.W. Boyd. *Nonlinear Optics*. Elsevier Science, 2003.

[15] J.M. Blackledge. *Digital Signal Processing: Mathematical and Computational Methods, Software Development and Applications*. Woodhead Publishing Series in Electronic and Optical Materials. Elsevier Science, 2006.

[16] K.M.M. Prabhu. *Window Functions and Their Applications in Signal Processing*. CRC Press, 2018.

[17] C.S. Lessard. *Signal Processing of Random Physiological Signals*. Synthesis lectures on biomedical engineering. Morgan & Claypool Publishers, 2006.

[18] T.G. Feeman. *The Mathematics of Medical Imaging: A Beginner's Guide*. Springer Undergraduate Texts in Mathematics and Technology. Springer, 2009.

[19] Qiuxiang Meng, Yizhu Zhang, T.-M. Yan, and Y. H. Jiang. Post-processing phase-correction algorithm in two-dimensional electronic spectroscopy. *Opt. Express*, 25(6):6644–6652, Mar 2017.

[20] Zhengyang Zhang, Kym Lewis Wells, Edward William James Hyland, and Howe-Siang Tan. Phase-cycling schemes for pump–probe beam geometry two-dimensional electronic spectroscopy. *Chemical Physics Letters*, 550:156 – 161, 2012.

CHAPTER 3
ULTRAFAST ENERGY FLOW IN EXTENDED FRET NETWORKS

3.1 Introduction to FRET-based Dye-DNA Networks

Structural DNA technology allows for the construction of unique structures and the precise placement of fluorophores. Many of these structures can be used for applications such as biosensing and nanoscale computing.[1, 2, 3, 4, 5] Light harvesting is also an attractive possibility for DNA-based nanotechnologies, owing to advantageous properties such as scalability, self-assembled synthesis, and the diverse quantity of commercially-available fluorophores available for use.[6, 7, 8] Molecular photonic wires composed of double-stranded (ds) DNA with bound small molecular dyes have seen increased study as they are able to transfer excitonic energy up to 30 nm. HomoFRET, which involves Förster Resonance Energy Transfer between identical fluorophores, has been seen to increase effective excitation energy distance. Of course, using homoFRET will decrease the overall efficiency of transport, as adding a random walk component will decreases directionality of FRET, but adding these homoFRET areas makes longer excitation energy transfer distances possible. [9]

One strategy to increase overall efficiency is to add redundant paths in a device. Figure 3.1 shows one such design, from Klein et al., which makes use of four identical arms leading on a downward energy gradient towards a Cy5.5 nexus. The redundancy of adding The overarching goal of this structure would be to capture blue light and down-convert toward red fluorescence of a Cy5.5 dye. In work by Klein et al. [10], the observed anywhere-to-end efficiency of the Four-Arm Star measured experimentally under-performed the efficiency calculated theoretically using semi-empirical models. Additionally, multiexcitonic effects within the realm of dye-DNA structures are still not understood. While fluorescence and absorption work to explain coupling of spectral features, such as the J-integrand for each

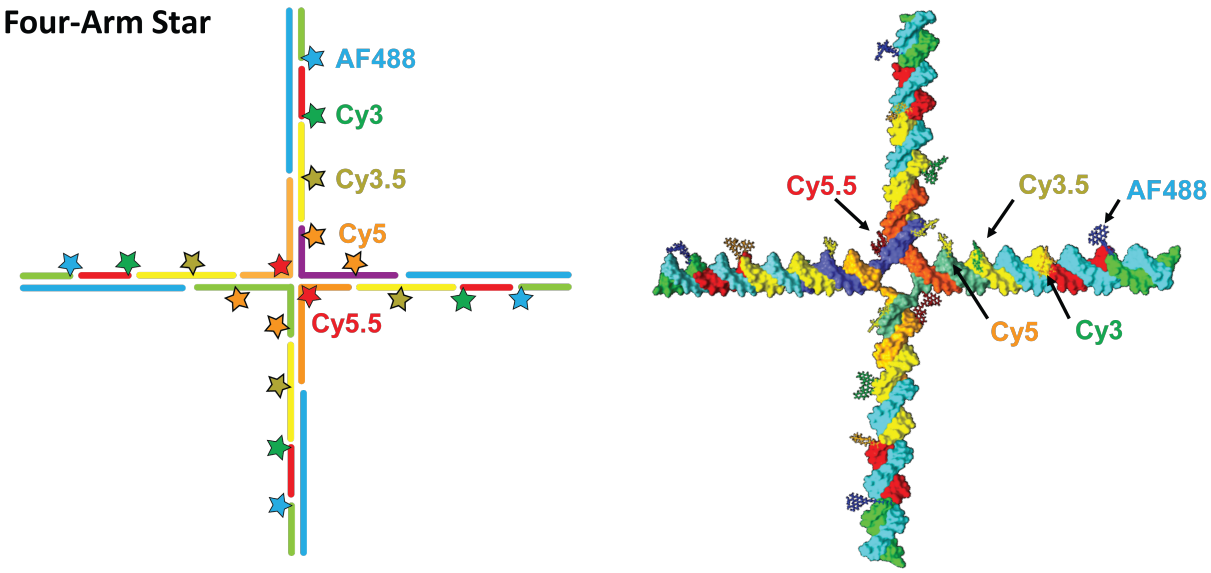

Figure 3.1: (Right) Double-stranded DNA is represented as parallel where dyes are represented by stars. (Left) Space-filling diagram showing the same progression of dyes. The number of dyes (Cy3-Cy3.5-Cy5-Cy5.5) is (4-4-4-2).

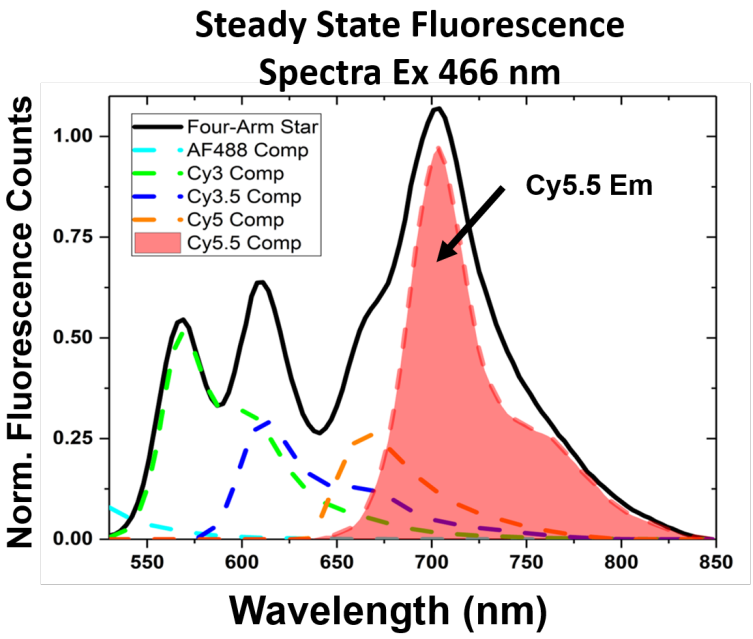

Figure 3.2: The Four-Arm Star is found to have $16.5 \pm 2.4\%$ end-to-end efficiency. This is found by exciting the sample at 466 nm and studying the resulting steady-state fluorescence.

step of FRET, the mechanics of transfer efficiency such as dye-to-dye energy transfer, can be disentangled from final fluorescence using ultrafast spectroscopy. Given the wide bandwidth of dyes visible, the potential coupling between each adjacent dye, and the desire to see what multiple excitations would detail about overall device robustness (such as possible exciton-exciton annihilation), two-dimensional electronic spectroscopy (2DES) was performed on a samples of the Four-Arm Star (Figure 3.1) at multiple fluences.

3.2 Spectroscopic Results and Discussion

Figure 3.2 shows one piece of optical characterization, steady-sate fluorescence. End-to-end transfer efficiency in the samples is a parameter describing their transmitting capabilities, or in other words, how well do they move excited state energy from blue wavelengths to red wavelengths. Anywhere-to-end transfer efficiency is a measure of the sample's collecting, or

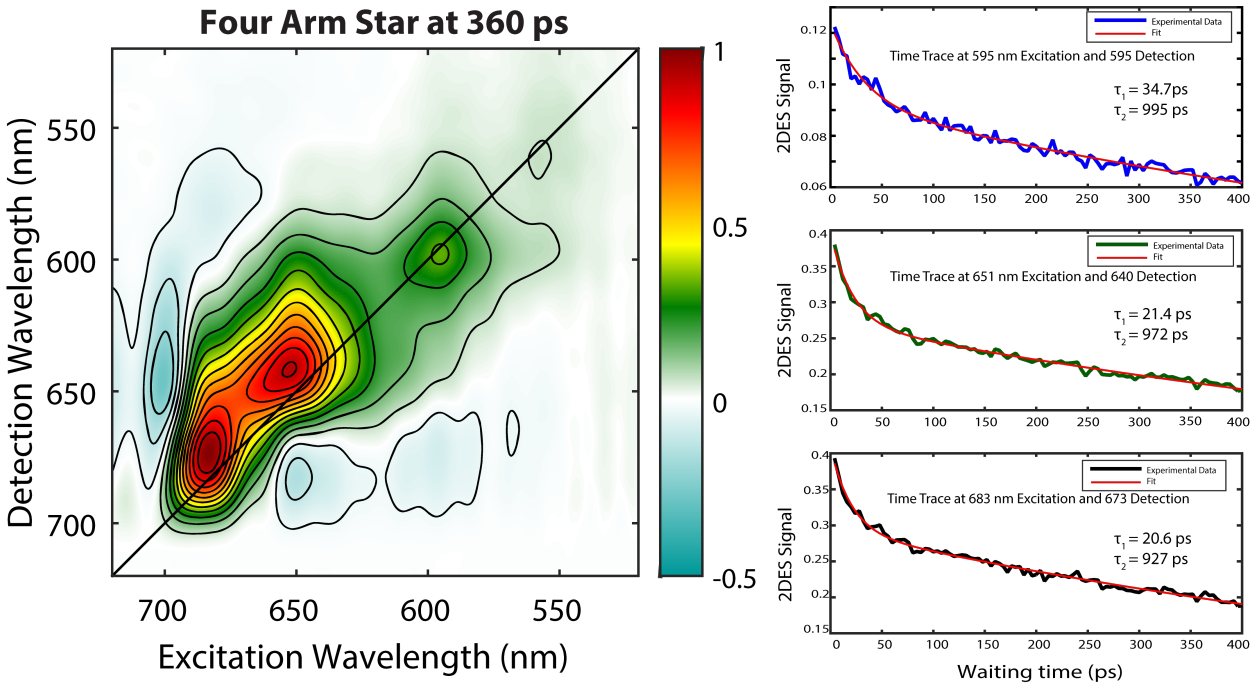

Figure 3.3: Three time traces and a 2DES frame of the Four-Arm Star taken on the picosecond timescale. Negative features below the diagonal indicate double-excitations on the same Four-Arm Star, indicating that the fluence this measurement was carried out at (around 20 nj/pulse) was sufficient to begin to see multiexcitonic behavior

harvesting, capabilities. Typically these measurements are carried out under white light, giving another reason to use 2DES, which is a broadband technique.

In this work, we use 2DES to study the energy transfer dynamics of a novel dye-DNA construct, a Four-Arm Star. Figure 3.3 shows waiting time traces taken over the picosecond regime of three primary diagonal peaks corresponding to the main absorption feature of Cy5.5, Cy5, and Cy3.5, taken from $(\omega_\tau, \omega_t) = (595nm, 595nm)$, $(651nm, 640nm)$, and $(683nm, 673nm)$. Initial fitting to a biexponential ($R^2 > .95$) reveals two time constants, the first lasting around 20-30 ps and the second about 1 ns. The first is attributed to non-radiative relaxation, while the second is the fluorescence liftetime. Many different fluences were taken at these long times, and all revealed roughly the same dynamics, with very little to no energy transfer seen between the dyes. The potential to take 2D which probed mul-

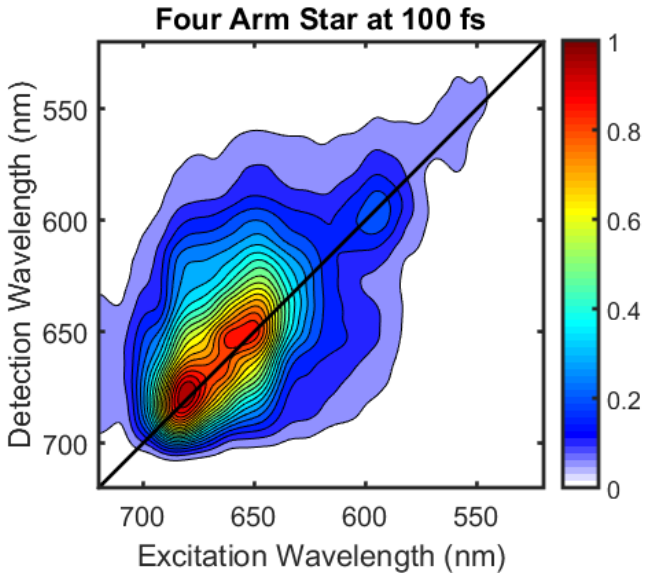

Figure 3.4: Frame taken at waiting time 100 fs when overall pulse power was 28 nj/pulse.

tiexcitonic behavior was confirmed by the presence of a negative peak below the diagonal, which is emblematic of a doubly-excited sample.

Having confirmed that these constructs could sustain higher fluences, and to better understand the nature of coupling (if any exists) between the different cyanine dyes, short-time fluence-dependent 2DES was taken from -100 to 1000 fs waiting time in 10-fs step-sizes. Three data runs were completed at fluences of 5, 10, and 28 nj/pulse. Analysis of 2D frames was inconclusive, although crosspeaks were visible to grow in on the 50 fs timescale in the higher fluence runs. Figure 3.4 shows a sample 2D frame, at 100 fs Waiting Time, showing such cross peaks. It should be noted that phasing, an integral part of 2D data work up where the absolute phase of a BOXCARS 2D acquisition is corrected with the phase of pump probe was not possible for the short time runs.

Preliminary comparison between time traces was completed, and centered around the Cy5-Cy5.5 nexus due to the strength of the overall signal at that region. Figure 3.5 shows two fluence-dependent traces from the Cy5.5 diagonal peak and the Cy5-Cy5.5 lower diagonal peak. While these results are preliminary and would need to be supported with repeat 2D

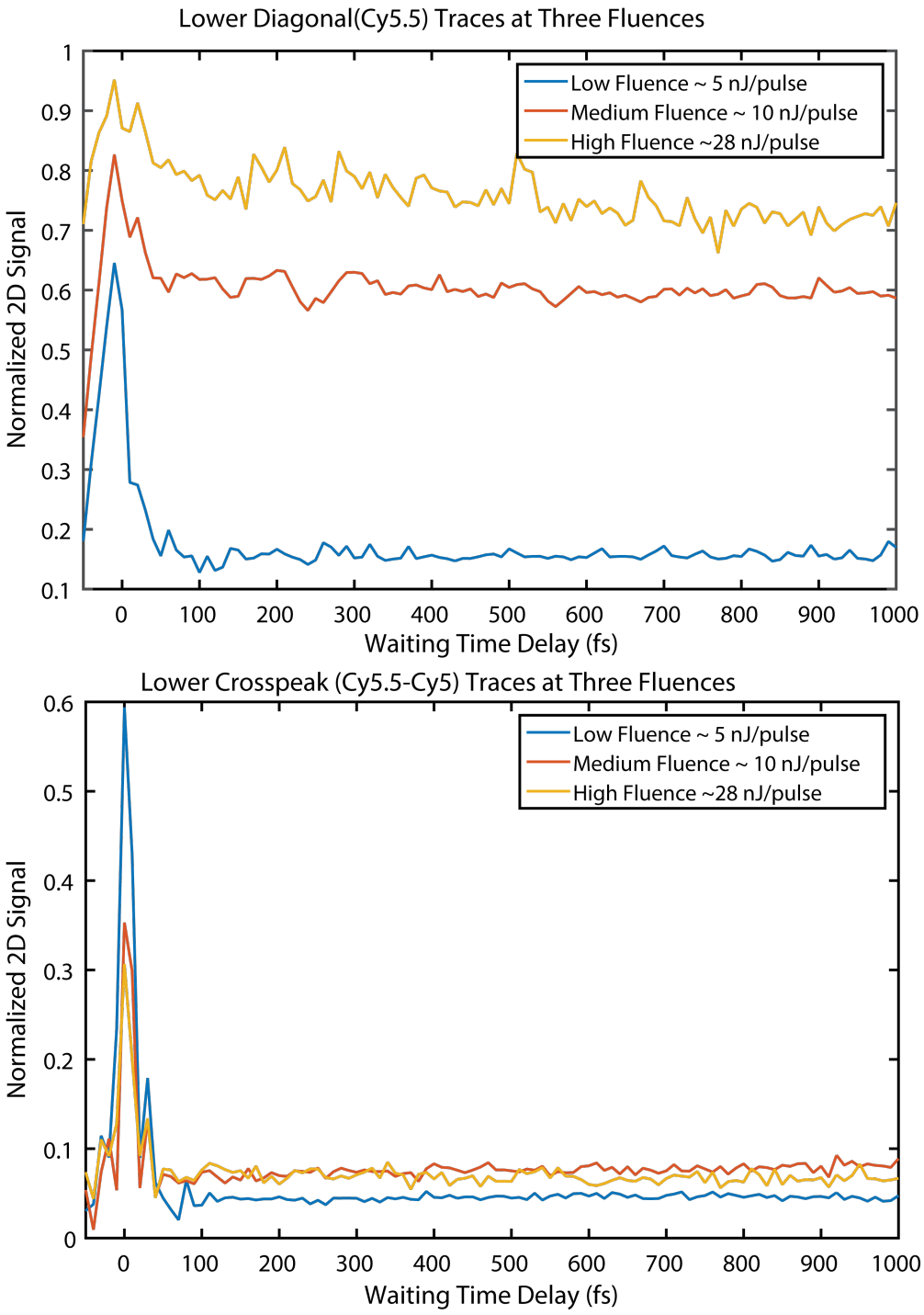

Figure 3.5: Fluence dependent waiting time traces taken at the the Cy5.5 diagonal peak and the Cy5-Cy5.5 lower crosspeak. A much steeper decay with Cy5.5 lifetime is seen for the low fluence measurement, while a more rise is seen in the crosspeak traces

acquisitions, there does seem to be some underlying dynamical differences between the lowest power run and the two higher power runs, namely, a less steep drop-off of Cy 5.5 excited state liftetime and a slight rise within the crosspeak. Whether these are inherent differences or run-dependent needs to be verified, but it could point an ultrafast mechanism within the Cy 5.5 nexus which is sensitive to the number of excited Cy5 dyes. This would have implications for the principle of redundancy within the Dye-DNA construction community, as perhaps cramming more dyes next to each other within the desired core of transmission might hurt more than it helps.

This result correlates with work from which this sample is derived by Klein et al. [10] where an eight-arm star was seen to have poorer energy transfer properties compared to a Four-Arm Star. In that publication, this phenomenon was explained by the poor formation yield of the eight-arm star (around 30% compared to 90% for the Four-Arm Star). While formation yield could certainly explain decreased transfer efficiencies, the clustering of Cy5.5 dyes around the core could also lead to novel non-radiative decay pathways. This area is further explored in my MPW project (Chapter 6) whereas next steps for this research are explored in Future Directions (Chapter 7).

REFERENCES

[1] Huabing Chen, Zhanjun Gu, Hongwei An, Chunying Chen, Jie Chen, Ran Cui, Siqin Chen, Weihai Chen, Xuesi Chen, Xiaoyuan Chen, Zhuo Chen, Baoquan Ding, Qian Dong, Qin Fan, Ting Fu, Dayong Hou, Qiao Jiang, Hengte Ke, Xiqun Jiang, Gang Liu, Suping Li, Tianyu Li, Zhuang Liu, Guangjun Nie, Muhammad Ovais, Daiwen Pang, Nasha Qiu, Youqing Shen, Huayu Tian, Chao Wang, Hao Wang, Ziqi Wang, Huaping Xu, Jiang-Fei Xu, Xiangliang Yang, Shuang Zhu, Xianchuang Zheng, Xianzheng Zhang, Yanbing Zhao, Weihong Tan, Xi Zhang, and Yuliang Zhao. Precise nanomedicine for intelligent therapy of cancer. *Science China Chemistry*, 61(12):1503–1552, 2018.

[2] Keyao Pan, Etienne Boulais, Lun Yang, and Mark Bathe. Structure-based model for light-harvesting properties of nucleic acid nanostructures. *Nucleic Acids Research*, 42(4):2159–2170, 12 2013.

[3] Jing Pan, Feiran Li, Tae-Gon Cha, Haorong Chen, and Jong Hyun Choi. Recent progress on dna based walkers. *Current Opinion in Biotechnology*, 34:56 – 64, 2015. Systems biology Nanobiotechnology.

[4] Gourab Chatterjee, Neil Dalchau, Richard A. Muscat, Andrew Phillips, and Georg Seelig. A spatially localized architecture for fast and modular dna computing. *Nature Nanotechnology*, 12(9):920–927, 2017.

[5] Rabeka Alam, Liliana M. Karam, Tennyson L. Doane, Kaitlin Coopersmith, Danielle M. Fontaine, Bruce R. Branchini, and Mathew M. Maye. Probing bioluminescence resonance energy transfer in quantum rod–luciferase nanoconjugates. *ACS Nano*, 10(2):1969–1977, 2016. PMID: 26760436.

[6] Palash K. Dutta, Symon Levenberg, Andrey Loskutov, Daniel Jun, Rafael Saer, J. Thomas Beatty, Su Lin, Yan Liu, Neal W. Woodbury, and Hao Yan. A dna-directed

light-harvesting/reaction center system. *Journal of the American Chemical Society*, 136(47):16618–16625, 2014. PMID: 25340853.

[7] Ivan L Volkov, Zakhar V Reveguk, Pavel Yu Serdobintsev, Ruslan R Ramazanov, and Alexei I Kononov. Dna as uv light–harvesting antenna. *Nucleic Acids Research*, 46(7):3543–3551, 11 2017.

[8] Francesca Nicoli, Anders Barth, Wooli Bae, Fabian Neukirchinger, Alvaro H. Crevenna, Don C. Lamb, and Tim Liedl. Directional photonic wire mediated by homo-förster resonance energy transfer on a dna origami platform. *ACS Nano*, 11(11):11264–11272, 2017. PMID: 29063765.

[9] Sebastián A. Díaz, Susan Buckhout-White, Carl W. Brown III, Anirban Samanta, William P. Klein, Mario G. Ancona, Chris L. Dwyer, Ellen R. Goldman, Joseph S. Melinger, Paul D. Cunningham, Chris M. Spillmann, and Igor L. Medintz. Using dna nanostructures to harvest light and create energy transfer and harvesting systems. In Mark R. Hutchinson and Ewa M. Goldys, editors, *SPIE BioPhotonics Australasia*, volume 10013, pages 44 – 53. International Society for Optics and Photonics, SPIE, 2016.

[10] William P. Klein, Sebastián A. Díaz, Susan Buckhout-White, Joseph S. Melinger, Paul D. Cunningham, Ellen R. Goldman, Mario G. Ancona, Wan Kuang, and Igor L. Medintz. Utilizing homofret to extend dna-scaffolded photonic networks and increase light-harvesting capability. *Advanced Optical Materials*, 6(1):1700679, 2018.

CHAPTER 4

ULTRAFAST EXCITATION TRANSFER IN CY5 DNA PHOTONIC WIRES DISPLAYS DYE CONJUGATION AND EXCITATION ENERGY DEPENDENCY

4.1 Overview

The following chapter is adapted from Mazuski et al.[1] with full permission.

While our studies on the four-arm star showed little coherent transfer of energy, we redesigned the homoFRET portion into singular MPWs and took new strategies to account for differing ligature and binding techniques. The most interesting sample we ended up with was a 10-dye MPW consisting of four strongly energetically coupled dimers (eight dyes total) along with vestigial dyes (two in total) on either side. Using two more complete MPWs (five dyes each) in differing attachment chemistries along with smaller controls, a series of fluence dependent pump probe measurements were taken. We adjusted temperature and solvent to control for system-bath interactions and were able to show evidence for a non-radiative trap dissipating energy in our dimeric MPW. Finally, we hypothesize that FRET frustration, which until now has only been seen in multiphoton microscopies, may play a role in the increased lifetimes seen in the dimeric MPW at higher fluences.

4.2 Introduction to Molecular Photonic Wires

DNA-based nanophotonics, which utilize a DNA scaffold with bound organic dyes, have emerged in the past decade as a useful medium for both biologically compatible applications[2, 3, 4, 5, 6] and easily tunable platforms for photophysical research into the effects of aggregation and strong electronic coupling on excitation energy transfer.[7, 8] Interest in these devices encompasses a breadth of applied photophysics, including optoelectronics,[5, 9, 10]

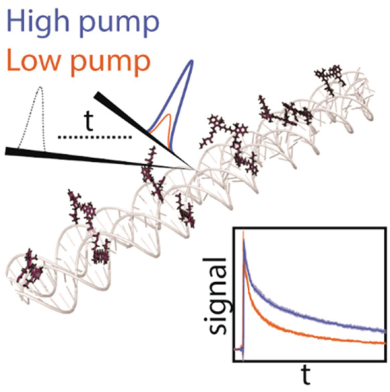

Figure 4.1: Fluence based pump probe spectroscopy reveals novel dynamics in which increased fluence is correlated with increased excited state lifetime. This is in stark contrast to conventional materials and photosynthesis research in which fluence and lifetime are anti-correlated.

sensing,[11, 12] biocommunications,[13] and logic-based computing,[14, 15] among others. Given the recent boom of research into DNA-based nanostructures, these complexes now range in size from simple double-stranded (ds) DNA wires displaying single dyes to large constructs interspersed with a wide variety of photonic materials.[2, 16] Analogous chemical model systems in which chromophores are covalently linked are useful for fundamental studies[17, 18] but limited in the expanse of structures that can be efficiently synthesized. In contrast, DNA as a template more closely approximates the biological medium found in nature and further allows for programmable designer structures of any arbitrary two- or three-dimensional shape with a multitude of chromophores placed with up to 1 nm precision based on a variety of bioconjugation strategies.[19, 20] DNA molecular photonic wires (MPWs) represent an optimal structure to begin to study the interplay of strongly and weakly coupled regimes. These one-dimensional arrays have been used for directional energy transfer from one end to the other and are used to extend the effective energy transfer length of devices of increasing architectural complexity.[21, 22]

As this field advances, evidence is growing that the positioning of the dye molecules, in the way they interact with the DNA[23] and, perhaps more importantly, with other dye

molecules,[24, 25] is the crucial variable in producing efficient light conducting systems. Most DNA-based photonic systems to date have exploited Förster resonance energy transfer (FRET) between different dyes to control the energy migration. More recent advancements have implemented FRET between chromophores of the same type (HomoFRET) to extend the effective energy transfer distance using one-dimensional excitonic diffusion in a random hop process.[26, 27] As the spectral overlap remains constant in HomoFRET, the process is not energetically lossy, allowing energy transfer to continue until a nonradiative trap is reached or the radiative lifetime of excitation has elapsed. Here the distance between fluorophores and the orientation of their dipole moments remain as key parameters to tune the HomoFRET efficiency.

Although numerous dye families have been developed over the years for all manner of biological applications, cyanine dyes remain one of the most popular families of organic dyes for use with DNA photonics. They have optimal photophysical properties, are readily conjugated using a multitude of linkage strategies, function as prime FRET pairs, and perhaps most pertinently, DNA strands incorporating cyanine dyes are commercially available from multiple vendors.[28] The more recent developments include the observation that cyanine dimers can form J-like or H-like dimers and that these result in drastically different properties (e.g., fluorescence lifetimes and spectral shapes) between the two types of dimers as well as in comparison with the monomer.[8, 29] Our current interest lies in deciphering whether the conjugation strategy of identical dye molecules, in our case Cy5, can modify the ET efficiency, particularly if we can create strongly coupled systems for improved ET. Within the literature there are multiple studies of the photophysics of Cy5 dye molecules[30, 31, 32] but an extremely limited number of studies of DNA-scaffolded Cy5 dimers[8, 29] with almost no insight into their ET properties. Additionally, experimentation on similar systems to date has remained ambiguous with regard to multi- and single excitonic behaviors, even though relevant studies on biological light-harvesting complexes and synthetic photonic materials

systems have shown key fluence-dependent photophysical discrepancies.[33] It is important to note that the former are the very types of function that DNA-based nanophotonics seek to emulate. Multiexcitonic effects within light-harvesting media are being increasingly studied to derive insights into fundamental principles of light harvesting, including measurement of the robustness of a light-harvesting material's performance, the ability of excitons to explore the material's vibronic potential energy surface, and effects, if any, on nonradiative decay mechanisms that may govern the exciton diffusion length and lifetime.[34, 35, 36]

Here we utilized an MPW as a linear DNA nanostructure designed in the form of five identical units of a double-crossover motif. Within each motif, Cy5 dye molecules were conjugated either on the 3' end, internally, or as a double-labeled DNA dimer (see the schematics in Figure 1). We found a large discrepancy in the maximum energy transfer efficiency along the wire, with the end-labeled MPW being 3 times more efficient than the internally labeled version and the dimer system having only trace transfer because of ultrafast nonradiative decay mechanisms. Utilizing ultrafast pump–probe spectroscopy, we observed control over the trap-mediated decay of excited-state energy transfer in the dimer with increased excitation density. This result was atypical because in classic multiphoton materials systems, increasing the excitation density results in shorter lifetimes of excited states as second-order and multibody effects dominate the excited-state dynamics.[35, 37, 38] Suppression of the ultrafast relaxation channel with increased excitation density, which was also observed at cryogenic temperatures, and subsequent analysis point toward a manifold of control mechanisms for modifying the FRET processes within the Cy5 MPWs. In the MPW configuration, multiexcitation fluences can increase the apparent excited-state lifetimes through an inherent mechanism of individual Cy5 dimers and the collective Cy5 dimer effect of HomoFRET frustration. This HomoFRET frustration arises at greater excitation fluence since multiple excitons occur on a single wire and excited Cy5 or Cy5 dimers are not efficient FRET acceptors.

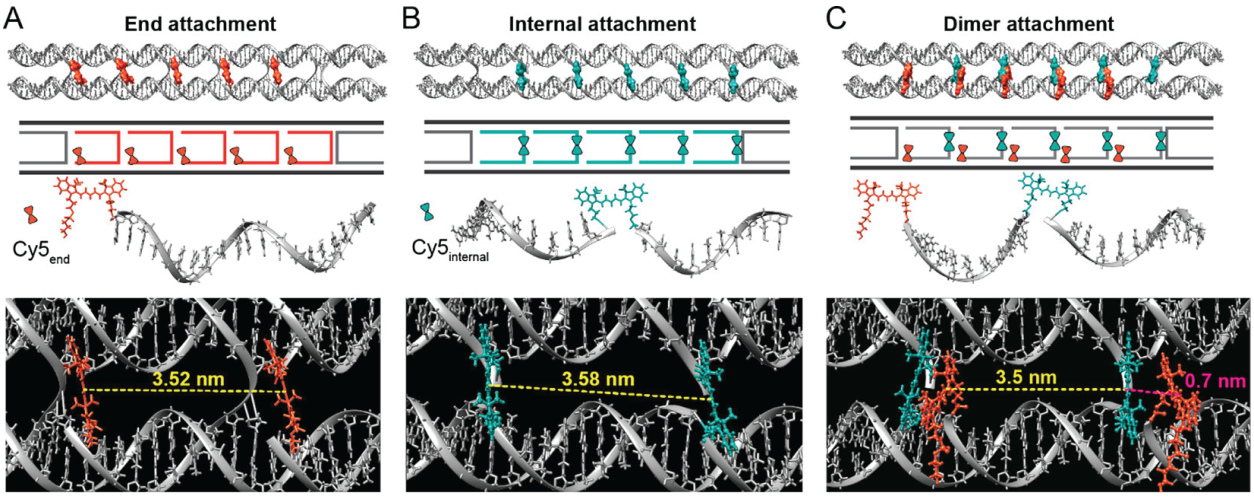

Figure 4.2: Schematics of the experimental DNA MPWs and dye-labeled DNA strand for (A) End attachment, (B) Internal attachment, and (C) Dimer attachment. (top) Molecular renderings of the MPWs with space-filled Cy5 molecules shown in orange for 3' end-conjugated dye molecules. (middle) Two-dimensional renderings of the MPWs showing the five repeating motifs within each structure and the associated Cy5 molecules. (bottom) Molecular structures of the Cy5-conjugated oligomers with zommed-in atomic structures denoting the dye-dye distances within the DNA MPWs.

4.3 Steady-State Specroscopy Results

The MPWs were designed exploiting a double-crossover motif originally proposed by Seeman[39] and used previously when studying HomoFRET systems.[21, 24, 40] The full list of strands, structural formulations, and modifications can be found in Tables 4.3 and 4.4 and Figure 4.7. The MPW is designed to be a two-helix-wide DNA structure containing five copies of Cy5-containing crossover motifs (see Figure 4.2). Within each motif, Cy5 could be either conjugated to the 3' end through a three-carbon-linker phosphodiester bond to the end nucleotide (End attachment), inserted between the middle bases via a double phosphodiester linkage (Internal attachment), or a double-labeled DNA strand with both an end and internal Cy5 (Dimer attachment). Samples were prepared in 2× phosphate-buffered saline (PBS) supplemented with 5 mM Mg^{2+}. Glycerol was added in a 3:1 ratio with buffer when realizing cryogenic measurements. Characterization of the freely diffusing strands not bound

Attachment:	**End**	**Internal**	**Dimer**
No. attached Cy5	5	5	10
Distance [nm][a]	2.8-3.6	3.4-4.0	3.5/0.9[b]
Exptl Distance [nm]	3.9 ± 0.5	4.5 ± 1.0	-[c]
Quantum Yield[d]	0.48	0.35	0.07
Lifetime (τ)	1.90 ± 0.10	1.29 ± 0.11	1.12 ± 0.11

Table 4.1: [a]Based on PDB structures. [b]Intradye/interdimer distance. [c]Determination of distances was not feasible with fluorescence lifetime anisotropy. [d]QY estimates have uncertainties of ∼5%. [e]Values are amplitude-averaged lifetimes.

within the MPWs is available in Figure 4.9 and 4.10 and shows the change in anisotropy and lifetime upon incorporation into the DNA MPW. Determination of the MPW formation efficiency was confirmed spectroscopically as well as through polyacrylamide gel electrophoresis (PAGE) (Figure 4.8). We estimate ∼90% MPW formation for all three structures, with ∼10% imperfectly or partially formed MPWs and trace amounts of free dye-labeled DNA observed in the gels. Using basic molecular models of the structures, we could determine the dye separations within the MPWs (see Table 4.1), which were compared to the values obtained by fluorescence lifetime anisotropy (values in Table 4.1, decay curves in Figure 4.9, and fitting parameters in Table 4.5). The Dimer MPW has a similar separation for the dye molecules with the same conjugation strategy, i.e., the internal Cy5s are 3.5 nm apart and the end-labeled Cy5s are 3.5 nm apart, but the end label of one motif within a structure is in close proximity (<1 nm) to the internal label of the previous motif, allowing coupled Cy5 dimers to form. The Dimer MPW can be particularized as four Cy5 dimers with single internal and end labels on the extreme ends of the MPW.

Room temperature (RT) steady-state spectra of the three MPW structures were obtained as part of the initial characterization (see Figure 4.3). The absorbance spectra in Figure 4.3A show that the End and Internal Cy5 had equivalent absorbance characteristics, while the coupling of the Cy5 dye molecules in the Dimer MPW is clearly observed in the enhanced vibronic shoulder at 600 nm. The lack of any observable excitonic splitting of the 0–0 absorp-

tion peak suggests that the Cy5–Cy5 dimers are inhomogeneous in distance and orientation. The heterogeneity of the dimers obscures sharp features (e.g., the splitting) as a result of the spectral broadening. The steady-state RT fluorescence spectra of the three MPWs are shown in Figure 4.3B. The normalized spectra overlapped almost perfectly, and the difference in the relative intensities is quantified in Table 4.1 by the difference in quantum yields (QYs). The End MPW had the brightest fluorescence of the three, with the Dimer MPW being the least fluorescent by a considerable margin. The fact that the spectra overlapped, even in the case of the Dimer MPW, suggests that much of the observed fluorescence came from monomeric Cy5. On the basis of the recent work of Huff et al. on coupled Cy5 pairs, the decrease in QY to the point of almost complete quenching is the result of a strong increase in nonradiative pathways (which they postulated to be nonadiabatic S_1–S_0 and S_0–S_0 transitions).[8]

Additionally, we determined the amplitude-averaged fluorescence lifetimes,$\langle\tau\rangle$, and as would be expected, $\langle\tau\rangle$ was correlated with the QY of Cy5 in the different MPWs, in that the lifetimes were ordered as End MPW Internal MPW Dimer MPW (see Figure 4.3C). However, compared with the difference in the QYs, we observed a longer $\langle\tau\rangle$ for the Dimer MPW than we would have predicted and that we later observed in the pump–probe experiments (*vida infra*). All of the lifetimes were best fit with biexponential functions, but the Dimer MPW demonstrated distinct short (<300 ps) and long (1.7 ns) τ components, while the End and Internal MPWs presented τ components in the 1.0–2.0 ns range. The longer than expected $\langle\tau\rangle$ and distinct τ components provide additional support for the heterogeneous nature of the Cy5 dimers in the Dimer MPW, and the small proportion of higher-QY monomers in the sample likely caused the deviation of the determined $\langle\tau\rangle$ to larger values.

For a greater understanding, we looked at control structures containing only one or two copies of the repeating Cy5 motif (not technically MPWs but similar in the DNA microenvironment around the Cy5), labeled as Control 1R and 2R, respectively (see Figure 4.6 for a schematic, Figures 4.9 and 4.10 for data, and Tables 4.5 and 4.6 for fitting values). Un-

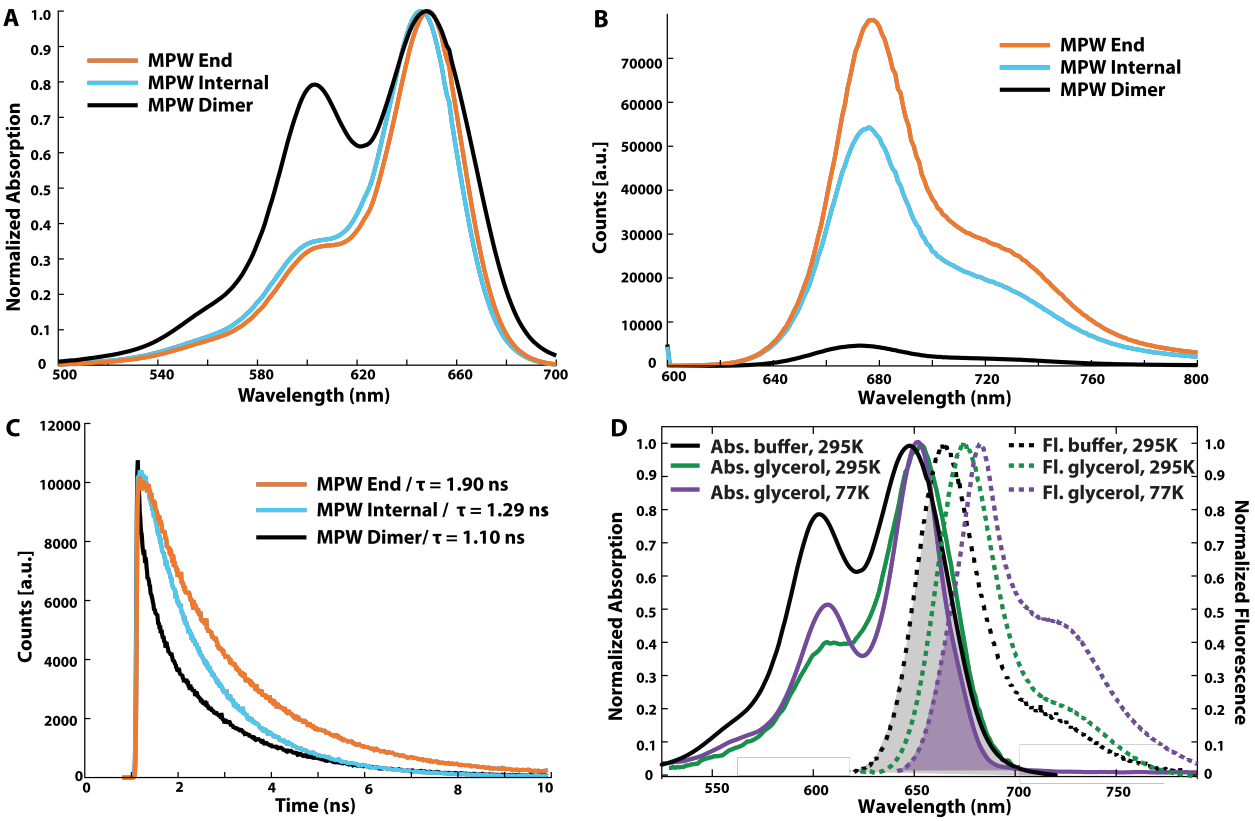

Figure 4.3: Samples were at RT and in aqueous buffer, unless otherwise noted. (A) Absorbance spectra (normalized to the Cy5 peak). (B) Steady-state fluorescence spectra, with excitation at 590 nm. (C) Fluorescence lifetime decay curves and $\langle\tau\rangle$ values. Samples were excited at 532 nm, and detection was centered at 680 nm. (D) Normalized absorbance spectra (solid curves) and fluorescence spectra (excitation at 560 nm; dashed curves) of the MPW dimer structure at 295 K in PBS (black), at 295 K in 3:1 glycerol/buffer (green), and at 77 K in 3:1 glycerol/buffer (purple). The shaded areas denote the respective spectral overlaps.

der the elementary assumptions of HomoFRET, transfer within the structure's equivalent Cy5 dye molecules should not modify the fluorescence output. However, when the control structures were tested, the addition of more dye molecules was found to decrease the relative steady-state fluorescence. We interpret this to occur because the presence of additional dye molecules increased the probability that one of the dye molecules within the MPW would act as a nonradiative trap, and the HomoFRET allowed this trap to be sampled by all excitations. The Internal and End MPWs underwent similar decreases in fluorescence, ∼10% in going from one to two Cy5 molecules and ∼40% in going from one Cy5 to the full MPW, while the fluorescence of the Dimer system decreased almost 90% in going to the full MPW (see Figure 4.12). For the Dimer system, the changes were even more marked: in the absorbance spectra, the vibronic shoulder increased as the number of dimer motifs within each structure increased (MPW > 2R > 1R), while the normalized absorbance spectra of the End and Internal systems were unmodified (see Figure 4.11).

These initial characterizations provided considerable information and allowed quantitative estimates of the theoretical transfer efficiency. On the basis of work by Cunningham et al.[41] and the Dimer MPW absorbance spectra, the overall distance between intradimer dye molecules was quantified to near 1 base pair (bp) separation, given that the ratio of the 0–1 to 0–0 absorption features was roughly 0.9 when the spectral components of the vestigial dye molecules were subtracted out (see Figure 4.13), though again we note that the Cy5 pairs were heterogeneous in their distance distribution. To provide quantitative estimates of the theoretical transfer efficiency, we utilized a random-walk model of HomoFRET[26] and determined the fluorescence lifetimes and FRET rates using data from fluorescence lifetime anisotropy. The fluorescence lifetimes and FRET rates for the End MPW were $\langle\tau\rangle$= 1.9 ns and $k_E T$ = 7.5 ns^{-1}, while the Internal MPW had values of 1.29 ns and 4.6 ns^{-1}, respectively. In this model, which measures an excitation entering at one end of the MPW and being extracted from the other, we assumed unity injection and extraction of an exci-

ton. Inputting the experimentally determined values resulted in a large discrepancy in the theoretical transfer efficiencies of the End and Internal MPWs (70% vs 23%, respectively) along the wire. The considerable difference between the efficiencies of the two MPWs arises from the shorter fluorescence lifetime of the Internal MPW along with the greater experimentally determined dye–dye distance, as shown in Table 4.1. Using similar assumptions for the Dimer MPW (though we recognize that treating the Cy5 dimers as single relays may not be fully valid) and the estimated values $\langle\tau\rangle = 1.1$ ns and $k_E T = 2.8$ ns^{-1}, we compute a transfer efficiency of less than 4%.

Previous work has shown an increase in MPW efficiency as well as Cy5 aggregate fluorescence lifetime under cryogenic conditions by suppression of phonon-mediated nonradiative relaxation pathways and the cis–trans isomerization of Cy5.[40] In Figure 4.3D we compare the ground-state absorption and fluorescence spectra of the Dimer MPW sample at RT in PBS and at 77 K in 3:1 glycerol/buffer to facilitate vitrification. We observe considerable spectral shifts, with the main peak of fluorescence shifting by 20 nm (from 662 to 682 nm). A portion of the shift ($\sim$10 nm) was due to the change in solvent, which had different viscosity and polarity due to inclusion of glycerol, yet further red shifting was observed upon cooling to 77 K. Of note is the change in the relative intensities of the two peaks observed in the absorption spectrum, which correspond to the 0–0 and 0–1 vibronic energy progression within Cy5 constructs. The intensity of the 0–1 peak is greater at RT than under cryogenic conditions. Conversely, the vibronic shoulder is much more pronounced in the cryogenic fluorescence spectrum relative to the RT spectrum, and this was independent of the solvent as it was not observed in the RT glycerol determination. This suggests considerable changes in the coupling of the dye molecules and the energetic pathways available to the Cy5 dimers between RT and 77 K. With regard to the increased energy transfer efficiency, it is important to note that the cryogenic conditions reduced the spectral overlap ($J = 2.02 \times 10^{16}$ and $6.30 \times 10^{15} nm^4 M^{-1} cm^{-1}$ at RT and 77 K, respectively). The QY of the dye is con-

siderably increased at cryogenic temperatures (0.07 to ∼0.25 on the basis of pump–probe lifetime determinations discussed below), but because of the diametric changes the Förster distance (R_0) was almost unchanged (5.5 ± 0.3 and 5.5 ± 0.5 nm for RT and 77 K, respectively). Since the dye–dye distances were on the order of ∼4 nm, this suggests that the theoretical dye–dye FRET efficiency was 0.87 ± 0.05 for both sets of conditions. Using the above-mentioned random-walk model, we would expect the transfer efficiency to increase only from 4% determined for RT to ∼12% for the Dimer MPW under cryogenic conditions.

4.4 Ultrafast Spectroscopy Results

Ultrafast pump-probe spectroscopy was used for further characterization, focusing on the Dimer MPW system. Ultrafast pump-probe spectroscopy provided the necessary spectral resolution to track the 0–0 and 0–1 vibronic peaks and temporal resolution to map the kinetics governing the sub-100 ps decay seen in the fluorescence lifetime. Furthermore, the pump power and therefore the number of excitations present on each MPW were varied to explore the excitation dynamics, which might be influenced by the energetic landscape. The fluence in terms of excitations per MPW was calculated as the product of the measured pump power at the focal spot size at the sample and the overlap of the absorption spectrum and the pump laser spectrum divided by the number of MPWs excited in the focal spot size. The full equation and measurement method are provided in the Supporting Information. Briefly, the excitation power measured by a coherent LabMAX-TOP power-meter was varied from 12 to 250 μW, and the diameter of the pump-probe overlap spot was measured to be 150 μm.[42] To fully excite the manifold of states within MPWs, broadband pump-broadband probe spectroscopy was used. Figure 4.4 shows a representative RT broadband pump-probe spectrum as well as kinetic maps taken from the major ground-state bleach (GSB) feature measured at 665 nm for the dimer MPW at RT and 77 K. Full sets of fluence-dependent pump-probe experiments for the other MPWs along with fits are available in Table 2 and in

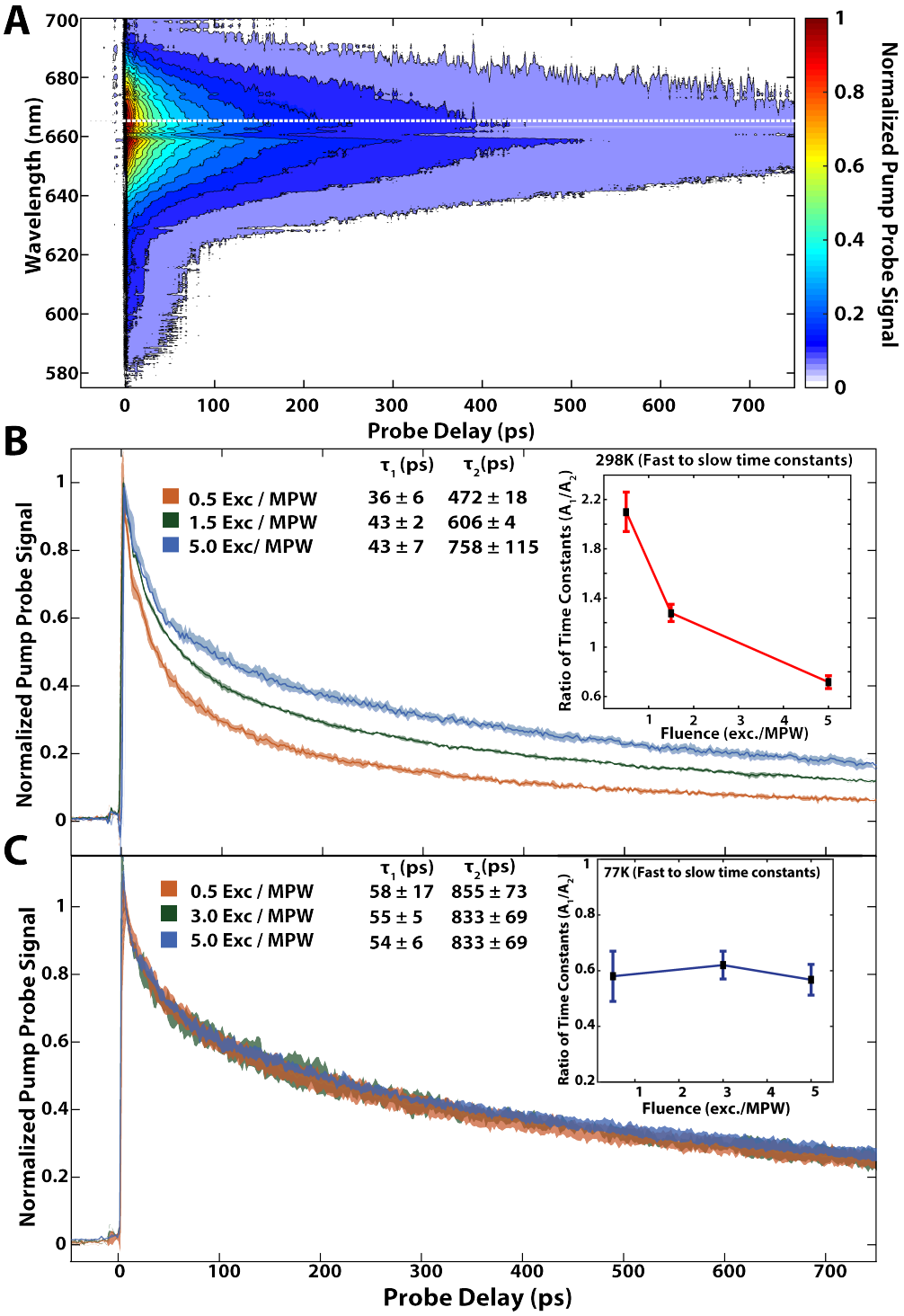

Figure 4.4: (A)Broadband pump-probe spectrum of the Dimer MPW at the lowest fluence. (B) Normalized pump-probe signal of the GSB at 665 nm for the Dimer MPW at RT in PBS. Inset: ratio of time constant weights (A_1/A_2) as a function of the number of excitations per MPW. (C) Normalized pump-probe signal of the GSB at 665 nm for the Dimer MPW at 77 K in 3:1 glycerol/buffer. Inset: ratio of time constant weights (A_1/A_2) as a function of the number of excitations per MPW.

Sample and Measurement Conditions	A_1 [%]	τ_1 [ps]	A_2 [%]	τ_2 [ps]	$\langle\tau_{GSB}\rangle$ [ps][a]
2× PBS + 5 mM Mg^{2+}					
Control 1R Iternal, RT, 0.5 excitations/MPW	12 ± 2	53 ± 8	88 ± 2	1136 ± 645	1001 ± 592
Dimer MPW, RT, 0.5 excitations/MPW	68 ± 13	36 ± 6	32 ± 13	472 ± 18	168 ± 64
Dimer MPW, RT, 5 excitations/MPW	43 ± 7	47 ± 9	57 ± 7	758 ± 115	450 ± 136
3:1 Glycerol/Buffer					
Dimer MPW, RT, 0.25 excitations/MPW	65 ± 13	150 ± 7	35 ± 13	1538 ± 947	642 ± 237
Dimer MPW, RT, 6 excitations/MPW	18 ± 6	100 ± 25	82 ± 6	1600 ± 64	1333 ± 126
Dimer MPW, 77 K, 0.5 excitations/MPW	42 ± 14	58 ± 17	58 ± 14	855 ± 73	522 ± 200
Dimer MPW, 77 K, 5 excitations/MPW	39 ± 8	54 ± 6	61 ± 8	833 ± 69	525 ± 132

Table 4.2: Biexponential fits of the GSB kinetic feature from pump-probe experiments on the Cy5 controls and MPWs. [a] $\langle\tau_{GSB}\rangle$ is the amplitude-averaged decay time of the GSB feature from the pump–probe experiments. This is to distinguish it from the fluorescence lifetime measurements.

Tables 4.7,4.8, and 4.9, and Figures 4.14, 4.15, 4.16, 4.17, 4.18, 4.19, 4.20, 4.21, and 4.22. No sample bleaching or destruction was observed even at the higher excitation powers, and this was confirmed by looking at the kinetic curves scanning the probe excitation from later to earlier times (i.e., looking at the 750 ps delay first and then observing the 5 ps delay first) and obtaining the same spectral results.

The resulting decay curves were best fit to a biexponential function ($R^2 > 0.99$), and the resulting constants revealed a sub-100 ps time constant (τ_1) along with a longer time constant ($\tau_2 > 400$ ps). Under the low-excitation-fluence conditions, we attribute the short (<60 ps) time constant to strongly coupled dimers with ultrafast nonradiative decay, whereas the longer time constant (400-800 ps) was tentatively attributed to Cy5 dimers that are more weakly coupled, i.e., with larger spacing and slower nonradiative relaxation. Cryogenic experiments (Figure 4.4C) were performed on a 3:1 glycerol/buffer solution of the Dimer MPW sample to analyze the nature of this ultrafast relaxation. The decay times τ_1 and τ_2 both were longer, and the ratio of the weights for the time constants (A_1/A_2) was 0.72 under the cryogenic conditions compared with 2.1 at RT. This slower decay suggests that under cryogenic conditions, the Cy5 dimer ultrafast nonradiative decay channel is suppressed. On the basis of the red shift in absorption and the more symmetrical nature of the absorption and fluorescence spectra, dimerlike photophysical behavior was essentially quenched at cryogenic

temperatures, with similar spectral properties as Cy5 monomers in glass.[30, 31, 43]

Within light harvesting and photosynthetic materials, the general understanding is that as the fluence is increased, no dependence on or a negative correlation with the excited-state lifetime should be observed because of the increased frequency of multiphoton effects such as exciton–exciton annihilation.[35, 37, 44, 45] Surprisingly, at RT for the Dimer MPW, as the fluence was increased, an increase in excited-state lifetime (as measured by the GSB signal) was observed (Figure 4.4B). There was a statistically significant increase in both the time constants and the A_1/A_2 ratio as the fluence was increased, as can be seen in Table 4.2. At fluences below one excitation per MPW, the excited-state populations of the Dimer MPWs would be twice as likely to exhibit sub-50 ps relaxation compared with the radiative lifetime, while at five excitations per MPW the longer time constant was almost twice as likely. This can be clearly observed by looking at the changes in the A_1/A_2 ratio shown in the inset. Similar studies of the End and Internal MPWs showed no fluence dependence, with the kinetic curves overlapping at all excitation powers (Figures 4.14 and 4.15).

RT fluence-dependent measurements were performed in the glycerol solution to account for the change in viscosity in the previous cryogenic experiments (see Figure 4.18). The fluence dependence was preserved, with a similar increase in relative lifetime (2.7-fold for buffer and 2.1-fold for the glycerol/buffer medium), indicating that the mechanism by which the nonradiative quenching was eliminated under cryogenic conditions was related to temperature and not a change in polarity or viscosity due to solvent effects. This supports the conclusion that when the two critical variables of temperature and excitation fluence are adjusted, two distinct mechanisms for inhibiting the ultrafast quenching occur.

The Control 2R Dimer structure, which consists of one electronically coupled dimer (see the schematic in Figure 4.6), showed fluence-dependent behavior similar to the Dimer MPW (Figure 4.19). In comparison, the response to increased fluence was less than that of Dimer MPW upon excitation at equivalent saturation ratios (i.e., taking into account the difference

in the number of dye molecules per DNA structure), as the relative lifetime increased 2-fold versus 2.9-fold for the Control 2R Dimer versus the Dimer MPW, respectively. Similarly the A_1/A_2 ratio changed by factors of 2.0 for the Control 2R Dimer and 3.0 for the Dimer MPW. This signifies that there are likely two mechanisms that modify the Dimer MPW decay times. The Cy5-dimer-specific decay mechanisms arise from J- and H-like dimer formation,[29, 46] which the Dimer MPW and Control 2R structures both experience. One possible hypothesis for this observation is that at greater fluence, double excitation of the Cy5 Dimers occurs,[47] which can frustrate the fast decay mechanism by inhibiting trans–cis conversions.[48, 49] Additional investigations that lie outside of the scope of the current report would be required to confirm this hypothesis.

4.5 Discussion of Mechanism Leading to Fluence-Dependence

To account for the additional increase in fluence dependence in a comparison of the Control 2R Dimer to Dimer MPW, we proposed an adaptive mechanism in which several kinetic routes compete for the transfer of excitation energy. These potential fluence-dependent mechanisms, which are schematically depicted in Figure 4.5, include Cy5-Cy5 HomoFRET (Cy5 dimers may also participate in HomoFRET transfer), Cy5 or Cy5 dimer fluorescence, nonradiative relaxation, and dimer-induced nonradiative decay pathways. On the basis of the relative increase in the excited-state lifetime (as measured by the GSB signal) at higher fluences for the Dimer MPW compared with the Control 2R Dimer, we hypothesize that ultrafast energy depletion arises from a portion of the dimers that act as high-efficiency traps. Moreover, because of the HomoFRET, almost all of the excitons across the energetic landscape sample the trap state independent of where the exciton arises. Upon multiple excitations per MPW, such as at the higher excitation fluences, the probability that a neighboring Cy5 or Cy5 dimer is in an excited state and therefore not able to function as an efficient FRET acceptor increases. The result of this is that excitons cannot sample the en-

tire MPW. Additionally, under cryogenic conditions the thermal quenching of the Cy5 dimer dark relaxation pathway was observed. Although the exact means by which this pathway is quenched has not been determined, previous research showed the marked temperature dependence of vibronic coupling between the separate components of cyanine homodimers.[41] The stabilization of fluorescence at lower temperatures is also consistent with the increased MPW performance that has been seen in cryogenic and solid-state applications.[40]

This investigation of the optimal conjugation strategy for a Cy5-dye-based HomoFRET MPW suggests two distinct observations of considerable interest. First, comparing the End and Internal conjugation strategies, we found that even at similar dye-dye distances, the more freely bound End label resulted in a more efficient FRET system. At just four HomoFRET steps, the maximal output decreased from 70% to 23% efficiency in going from End labeling to Internal labeling. Clearly, if the system were extended in length, this difference would increase even further. Also, creating closely packed dimers as transfer relays, at least in the case of Cy5 (and in this structural configuration), was completely counterproductive; any increase in extinction coefficient or other positive effect was greatly outweighed by ultrafast ($<$100 ps) nonradiative decay that was increasingly accessed in the Cy5 dimers. However, in a different system, one where the dimers were brought close enough together, it is possible that the FRET rate could compete with the nonradiative decay. The second set of observations was more surprising. Utilizing increased fluence as well as cryogenic temperatures, the Dimer MPW showed a marked decrease of the ultrafast decay, recovering fluorescence lifetimes, and therefore theoretical transfer efficiencies similar to those of the other MPWs. The ultrafast nonradiative relaxation unique to the Dimer systems could be overcome by three unique mechanisms: a cooling mechanism that quenched the Cy5 dimer decay mechanism, a fluence-dependent mechanism related to increasing probability of multiexcitation of Cy5 dimers (the distribution of this multiexcitation is not clear at this time), and a mechanism mediated by the impact of FRET frustration on the flow of energy through a molecular photonic system

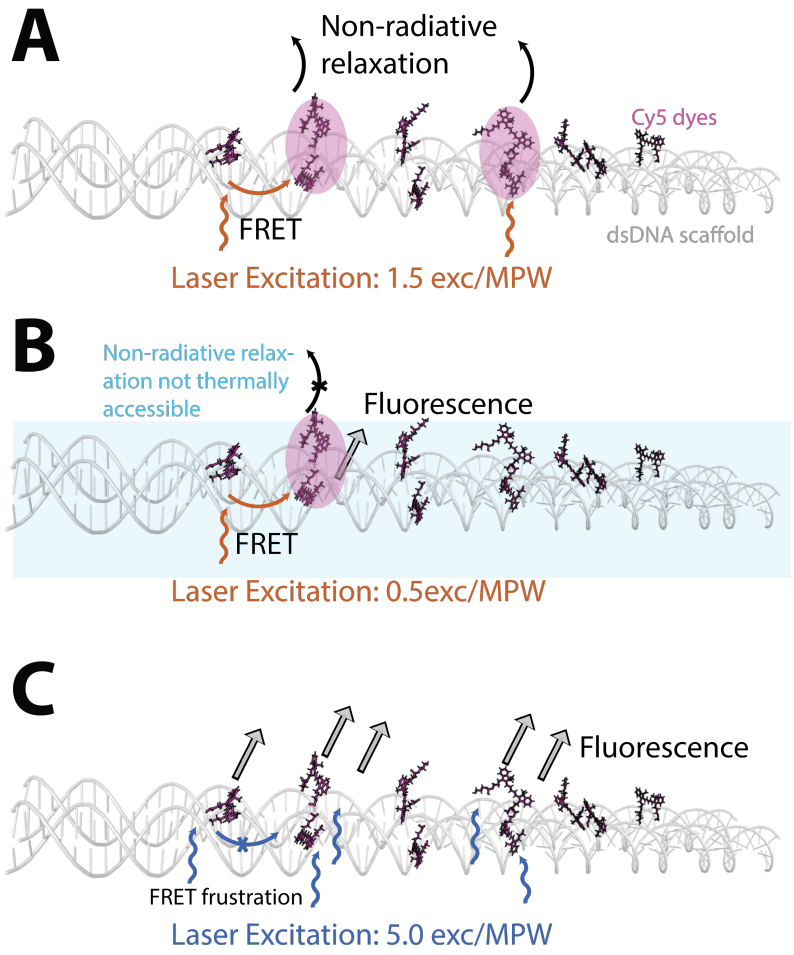

Figure 4.5: (A) RT aqueous buffer and low excitation fluence. Dimer MPWs (gray dsDNA scaffold and bolded Cy5 dye molecules) are characterized by efficient capture of excitation energy by trap sites (pink ovals). At low fluence, excitations of vestigial dye molecules can freely undergo FRET to a dimer trap. (B) 77 K 3:1 glycerol/buffer and low excitation fluence. Although excitations can freely undergo FRET throughout the MPW, nonradiative relaxation is not observed to occur, leading to longer lifetimes. (C) RT aqueous buffer and high excitation fluence. Dimer double excitation leads to inhibition of trap-site nonradiative relaxation, and excitation density leads to FRET frustration, allowing vestigial dye molecules to fluoresce.

as the excitation density is increased. The last of these effects seems to point to the fact that within the DNA nanostructure a nontrivial proportion of the Cy5 dimers are in fact in spatial conformations in which their coupling results in stronger dipoles without the appearance of the additional nonradiative decay.

Finding a way to isolate and utilize these dye conformations could be of considerable interest in many areas of bio/nanophotonics. The strongly coupled dye pairs, which maintain their radiative lifetime, could be exploited to utilize coherent transfer as opposed to the current FRET mechanism, and this should improve the transfer speed and efficiency in artificial light-harvesting systems as one example. The findings also promote consideration of the novel behavior of strongly coupled dye-based nanophotonics at elevated fluence, as this behavior may be useful in more applied settings such as excitonic engineering and optical computing.[50]

4.6 Experimental Methods

Sample Assembly: MPWs were assembled at a final concentration of 25 μM by combining the constituent oligomers in 2× PBS (0.276 M NaCl, 0.0054 M KCl, pH ∼7.4) + 5 mM $MgCl_2$ and thermally annealing the solution from 94 to 4 °C at -1 °C/min. The stoichiometric ratios of oligomers used in the different MPW conformations are specified in Table 4.4. Experiments were performed with the samples in 2× PBS + 5 mM Mg^{2+} or with the addition of glycerol for power and cryogenic measurements.

Sample Preparation for Ultrafast Measurements: For RT spectroscopy, samples were diluted using buffer solution to an optical density (OD) of ∼0.3 at λ_{max} (∼650 nm) in a 200 μm path length quartz cell. For cryogenic measurements, samples were diluted using a 3:1 mixture of glycerol to 2× PBS to an optical density of ∼0.3 at λ_{max} (650 nm) and cooled to 77 K in a liquid-nitrogen-cooled Oxford Optistat DN cryostat.

Absorption and Fluorescence Spectroscopy: Steady-state absorption spectra were mea-

sured on 60 μL samples in a 3 mm path length cuvette after 20-fold dilution using an Agilent 8453 diode array UV-vis spectrophotometer. Cryogenic absorption spectra were measured using a liquid-nitrogen-cooled Oxford Optistat DN cryostat in a Cary 5000 UV-vis-NIR spectrophotometer. Fluorescence spectra were measured with a multifunction microtiter plate reader (Tecan Infinite MR 1000 Pro) in a 96-well plate using 50 μL of sample with excitation at 590 nm. Cryogenic fluorescence was measured on a Horiba Fluorolog-3 fluorimeter. Fluorescence quantum yield determinations were realized on a Horiba-Jobin fluorimeter using cresyl violet as a standard. Fluorescence lifetimes $\langle\tau\rangle$ and lifetime anisotropies were measured with a time-correlated single photon counting (TCSPC) technique using a Becker-Hickl SPC-630 board. The excitation laser was an 80 MHz 7 ps pulsed 532 nm frequency-doubled diode-pumped Nd:YVO4 laser (High-Q picoTRAIN). Sample fluorescence was sent through a polarizer set to the magic angle for lifetime determinations and then filtered using a monochromator. The polarizers were adjusted to the pertinent parallel and perpendicular settings to obtain the anisotropy measurements.[24]

Ultrafast Pump-Probe Spectroscopy: The apparatus used to collect transient absorption spectra has been described in detail elsewhere.[51] Briefly, laser pulses used in transient absorption were generated from a Ti:sapphire regenerative amplifier (Coherent Legend Elite) seeded with a Ti:sapphire oscillator (Coherent Micra) to produce transform-limited pulses centered at 800 nm with a bandwidth of 28 nm at a repetition rate of 5 kHz and a power of 2.8 W. These pulses were focused into a 2-m long tube of argon gas held at 14 psig, producing a supercontinuum spanning 500 to 900 nm. This supercontinuum was filtered using a dichroic optic, rejecting all wavelengths greater than 700 nm. The filtered pulse was directed through a pulse shaper (Biophotonics Inc. MIIPS 640) and compressed to a duration of 10 fs measured at the sample position using a multiphoton intrapulse interference phase scan algorithm. The pulse was then directed into the pump–probe spectrometer, where it was split into pump and probe beams by a 90/10 beamsplitter. The probe was further attenuated

to a constant fluence of 1.5 μW while the pump fluence was varied from 12.5 to 150 μW. The pump was delayed relative to the probe by a mechanical delay stage (Aerotech ANT-130 L) and chopped by a mechanical chopper (New Focus Inc.). The pump and probe beams were then directed to the sample, which was held in a 200 μm path length cuvette (Starna Cells Inc.). The probe beam was then directed into a spectrometer (Horiba microHR), where it was spectrally resolved onto a CCD camera (Teledyne Dalsa Spyder3).

4.7 Supplementary Information

Pump Probe Spectroscopy Fluence Calculations:

Calculating the number of absorbed photons per MPW allows us to discretely assign multiexcitonic behavior. We adapt a method recently published (in SI) by Dostál et al. to retrieve pump photons per MPW.[42] Briefly, calculations were made using the following observables: cross-section of spatial overlap of the pump and probe pulses in our sample cell ($Area_{pump-probe}$), integrated power of the pump pulse measured with a Coherent LabMax-TOP (P_{pump}), absorbance of sample taken with Agilent 8453 (room temperature) or Cary 5000 UV/VIS/NIR Spectrophotometer (Liquid Nitrogen) ($A(\lambda)$), spectrum of pump pulses measured with Ocean Optics USB4000 Spectrometer ($Spec(\lambda)$), molar concentration of dyes (C) in solution, and sample cell thickness (d). Equation 4.1 shows the net equation to net excitations per MPW as reported in the paper and SI, where h is Planck's constant, c is the speed of light, λ is wavlength, N_A is Avogadro's number, and $Cy5/MPW$ is the number of Cy5 dyes bound to each MPW or control.

$$\frac{exc.}{MPW} = P_{pump} \times Area_{pump-probe} \times \frac{\int Spec(\lambda) \times \lambda(1-10^{-A(\lambda)})d\lambda}{hc\int Spec(\lambda)d\lambda} \times \frac{1}{CN_A d} \times Cy5/MPW \quad (4.1)$$

$$r(t) = r_0 - A_1 e^{t/\phi_1} - A_2 e^{t/\phi_2} \quad (4.2)$$

Name	Sequence	Tm [$^{\circ}C$]
Temp1	GCAGCTCAGGTTATTTCGTCTATATTCGTCTATATTCG TCTATATTCGTCTATATTCGTCTATAGGAGCAATTAAAGG	84.2
Temp2	AACTAGCAGTGACGTGATCGTCCTTGATCGTCCTTGAT CGTCCTTGATCGTCCTTGATCGTCCTAATTCGCTCGTAAC	84.2
Cap1	CCTTTAATTGCTCCCGTCACTGCTAGTT	77.2
Cap2	GTTACGAGCGAATTATAACCTGAGCTGC	75.6
Cy5-End	TATAGACGAAAGGACGATCA/3Cy5Sp/	66.2
Cy5-Internal	TATAGACGAA/iCy5/AGGACGATCA	66.2
Cy5-Dimer	TATAGACGAA/iCy5/AGGACGATCA/3Cy5Sp/	66.2
Temp1 R1	GCAGCTCAGGTTATTTCGTCTATAGGAGCAATTAAAGG	79.3
Temp2 R1	AACTAGCAGTGACGTGATCGTCCTAATTCGCTCGTAAC	79.3
Temp1 R2	GCAGCTCAGGTTATTTCGTCTATA TTCGTCTATAGGAGCAATTAAAGG	81.3
Temp2 R2	AACTAGCAGTGACGTGATCGTCCT TGATCGTCCTAATTCGCTCGTAAC	81.3

Table 4.3: **DNA sequences and melting temperatures.** All DNAs were obtained from IDT. Melting temperatures are estimated at 2× PBS+ 5 mM Mg^{+2} assuming dsDNA, though the structural design leads to decreases in T_m. We have demonstrated in very similar structures that the MPW is stable up to 50 °C.1 Dye insertion used a single phosphodiester labeling for /3Cy5sp/ and internal double phosphodiester labeling for /iCy5/.

Name	DNA Strands
End MPW	Temp1+Temp2+Cap1+Cap2+Cy5-End(5X)
Internal MPW	Temp1+Temp2+Cap1+Cap2+Cy5-Internal(5X)
Dimer MPW	Temp1+Temp2+Cap1+Cap2+Cy5-Dimer(5X)
Control 1R End	Temp1 R1+Temp2 R1+Cap1+Cap2+Cy5-End(1X)
Control 2R End	Temp1 R2+Temp2 R2+Cap1+Cap2+Cy5-End(2X)
Control 1R Internal	Temp1 R1+Temp2 R1+Cap1+Cap2+Cy5-Internal(1X)
Control 2R Internal	Temp1 R2+Temp2 R2+Cap1+Cap2+Cy5-Internal(2X)
Control 1R Dimer	Temp1 R1+Temp2 R1+Cap1+Cap2+Cy5-Dimer(1X)
Control 2R Dimer	Temp1 R2+Temp2 R2+Cap1+Cap2+Cy5-Dimer(2X)

Table 4.4: **Descriptions of MPW constituents utilized in the study** Parenthetical values represent differences in ratios. All other DNA's added in 1:1 ratios.

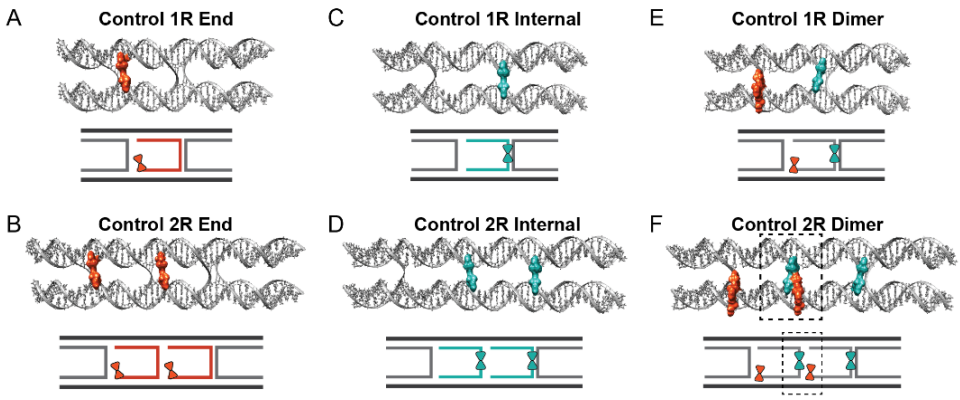

Figure 4.6: Schematic of Control 1R and 2R structures. Top: Molecular rendering. Bottom: 2D rendering and the associated Cy5 molecules. **(A,B)** End attachment. **(C,D)** Internal attachment. **(E,F)** Dimer attachment. The dashed box highlights the Cy5 dimer structure.

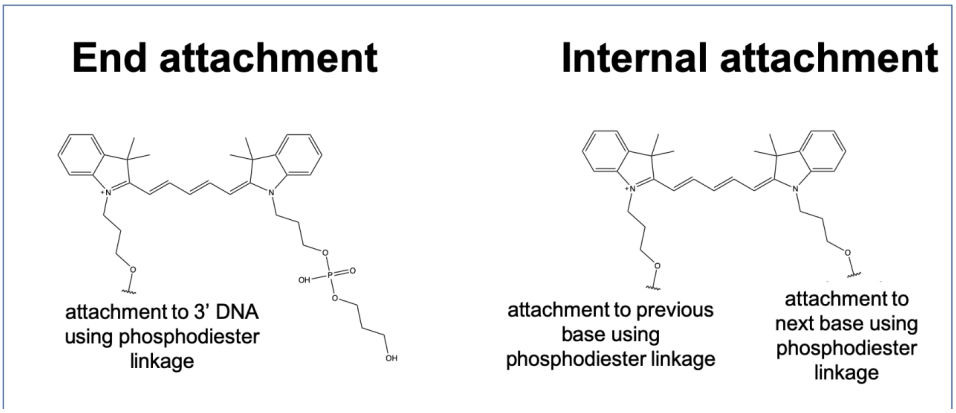

Figure 4.7: Attachment chemistries of End and Internal Cy5 DNA insertion.

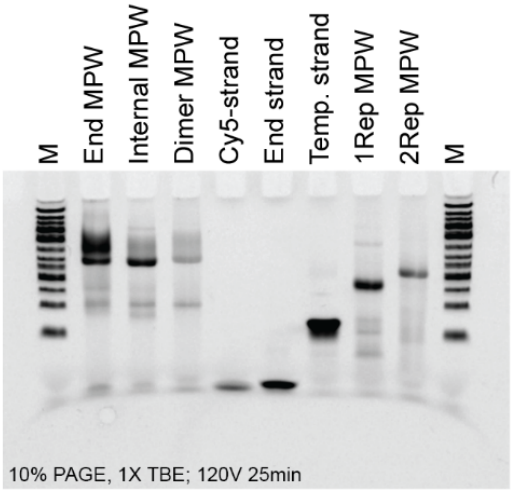

Figure 4.8: **10 % PAGE gel of MPW structures and individual DNA.** Gel ran in 1X TRIS/Borate/EDTA buffer at 120 V for 25 minutes. Stained with Gel Red. M: Molecular weight ladders.

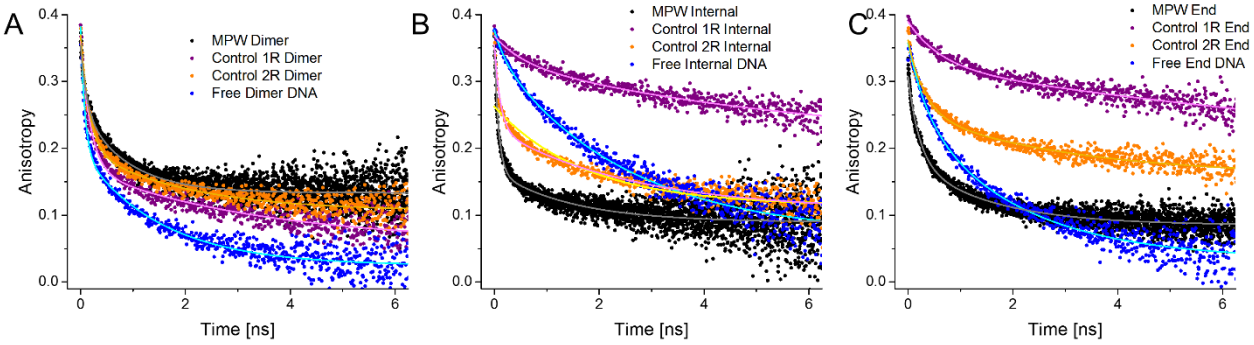

Figure 4.9: **Fluorescence lifetime anisotropy spectra.** MPW, control structures, and freely diffusing DNA at RT and in aqueous buffer. Solid lines are fits utilizing 2 exponential decays (values in tables below). **(A)** Dimer **(B)** Internal **(C)** End.

Cy5	r_0	Φ_1	A_1	Φ_1	A_2
MPW Dimer	0.1334±0.0005	0.11±0.02	0.093±0.006	0.87±0.04	0.126±0.005
Control 1R Dimer	0.058±0.003	0.19±0.02	0.192±0.009	3.4±0.4	0.111±0.003
Contro l2R Dimer	0.106±0.001	0.16±0.02	0.168±0.009	1.9±0.2	0.095±0.006
Free Dime rDNA	0.024±0.001	0.08±0.01	0.186±0.015	1.52±0.09	0.171±0.006
MPW Internal	0.089±0.001	0.081±0.006	0.189±0.007	1.52±0.09	0.171±0.006
Contro l1R Internal	0.21±0.01	0.53±0.18	0.037±0.007	5.9±1.3	0.126±0.006
Contro l2R Internal	0.106±0.002	0.11±0.02	0.125±0.009	2.6±0.2	0.122±0.003
Free Internal DNA	0.070±0.002	0.20±0.14	0.03±0.01	2.45±0.12	0.273±0.007
MPW End	0.085±0.001	0.22±0.01	0.124±0.003	1.53±0.07	0.098±0.003
Control 1R End	0.12±0.09	0.64±0.11	0.067±0.006	16±11	0.20±0.09
Control 2R End	0.158±0.002	0.31±0.04	0.106±0.006	3.0±0.3	0.097±0.004
Free End DNA	0.033±0.002	0.4±0.1	0.09±0.02	2.0±0.2	0.22±0.02

Table 4.5: Fitting parameters for anisotropy data. The fittings utilized a double exponential decay function

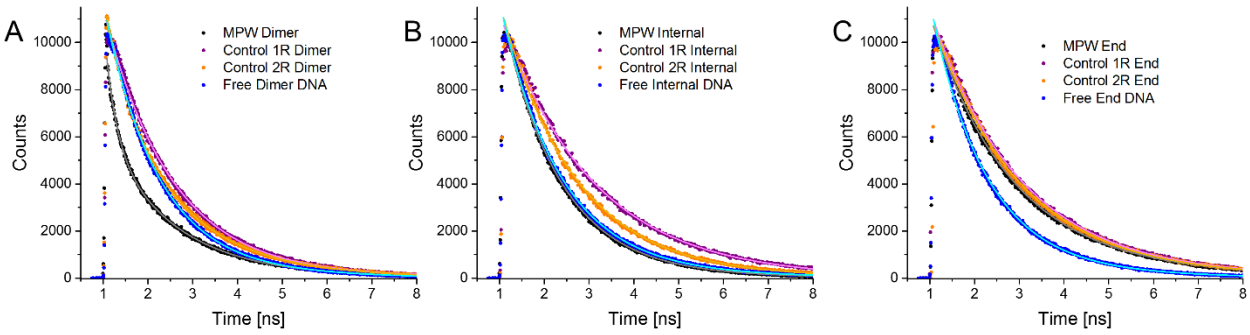

Figure 4.10: **Fluorescence lifetimes** Samples include MPW, control structures, and freely diffusing DNA at RT and in aqueous buffer. Samples excited at 532 nm. Solid lines are fits utilizing 2 exponential decays ($\langle\tau\rangle$ in tables below). **(A)** Dimer **(B)** Internal **(C)** End

	$\langle\tau\rangle$ [ns]		
Structure	Dimer	Internal	End
MPW	1.10 ± 0.11	1.29 ± 0.11	1.89 ± 0.10
Control 1R	1.50 ± 0.09	2.05 ± 0.05	2.01 ± 0.11
Control 2R	1.40 ± 0.09	1.66 ± 0.04	1.96 ± 0.09
Free DNA	1.25 ± 0.07	1.38 ± 0.08	1.28 ± 0.06

Table 4.6: Averaged fluorescence lifetimes.

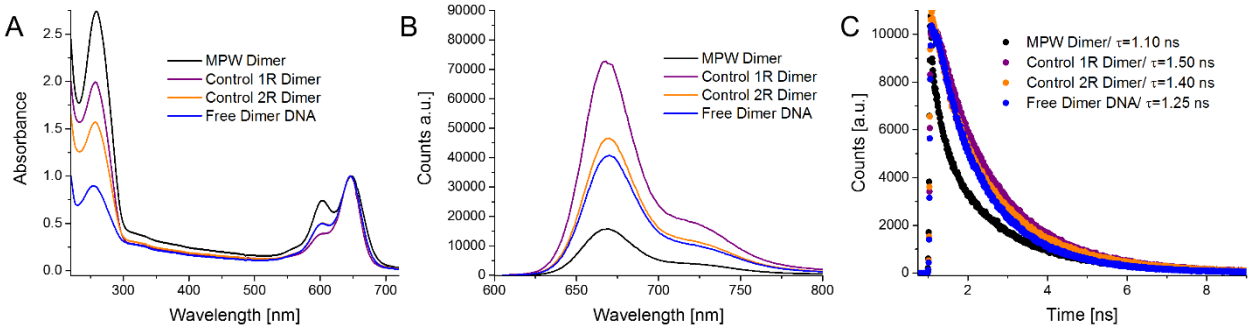

Figure 4.11: **Spectra of MPW and controls of Dimer dye structures.** **(A)** Absorbance (normalized to Cy5 peak) **(B)** Steady-state fluorescence, excited at 590 nm. All samples have equivalent concentrations of Cy5 dye. **(C)** Fluorescence lifetime spectra and $\langle\tau\rangle$. Excited at 532 nm.

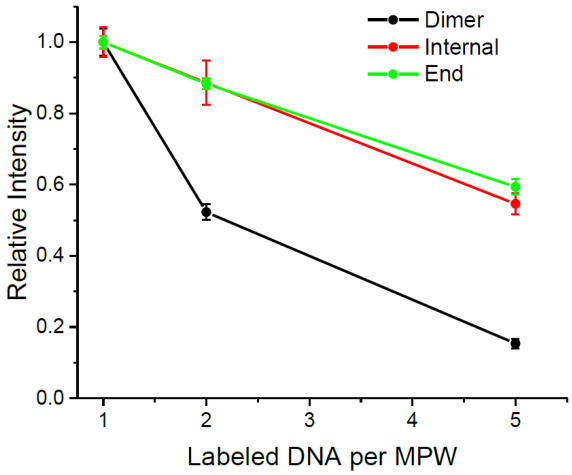

Figure 4.12: **Relative fluorescence intensity.** Data is normalized to Control 1R of a sample with increasing numbers of labeled DNA per nanostructure.

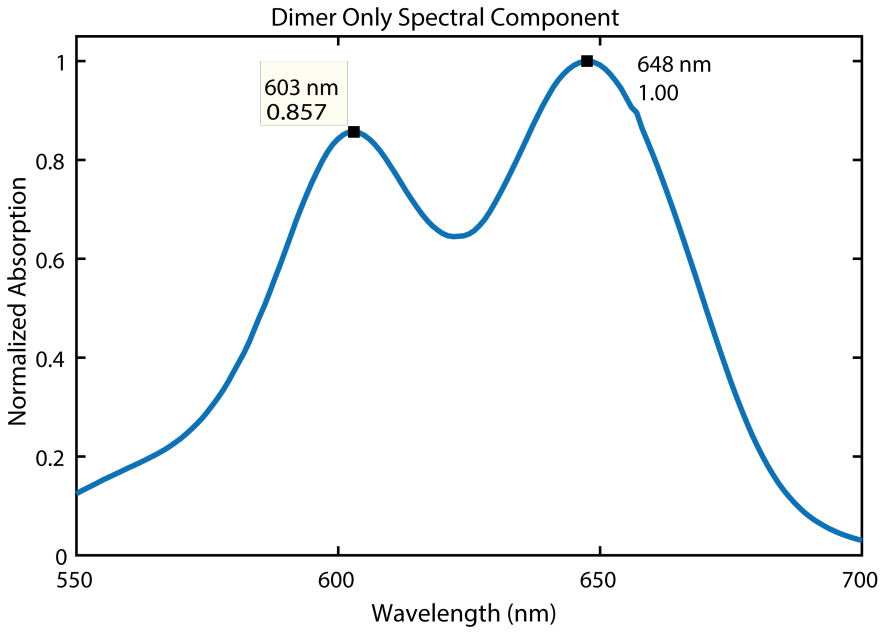

Figure 4.13: **Dimer absorption spectral components.** Data derived by subtracting vestigial dye spectrum (estimated as Control 1R Dimer) from Dimer MPW absorption spectrum. Taken at RT in aqueous buffer.

Fluence [exc/MPW] / Solvent; Temp	Φ_1 (ps^{-1})	A_1	Φ_2 (ps^{-1})	A_2
0.5 / Buffer; 295 K	0.028 ± 0.005	0.65 ± 0.12	0.00212 ± 0.00008	0.28 ± 0.05
1.5 / Buffer; 295 K	0.023 ± 0.001	0.47 ± 0.02	0.00165 ± 0.00001	0.31 ± 0.01
5.0 / Buffer; 295 K	0.021 ± 0.004	0.32 ± 0.05	0.00132 ± 0.00002	0.42 ± 0.04
10.0 / Buffer; 295 K	0.017 ± 0.003	0.31 ± 0.05	0.00122 ± 0.0001	0.42 ± 0.03
0.5 / Glycerol; 77 K	0.0173 ± 0.005	0.301 ± 0.01	0.00117 ± 0.0001	0.4 ± 0.1
3.0 / Glycerol; 77 K	0.018 ± 0.002	0.199 ± 0.004	0.0012 ± 0.0001	0.49 ± 0.02
5.0 / Glycerol; 77 K	0.018 ± 0.002	0.344 ± 0.07	0.0012 ± 0.0001	0.53 ± 0.03
0.25 / Glycerol; 295 K	0.0067 ± 0.0003	0.26 ± 0.05	0.0006 ± 0.0004	0.14 ± 0.03
2.5 / Glycerol; 295 K	0.0083 ± 0.0006	0.19 ± 0.02	0.0006 ± 0.0001	0.468 ± 0.002
6.0 / Glycerol; 295 K	0.010 ± 0.003	0.056 ± 0.002	0.00063 ± 0.00003	0.26 ± 0.02

Table 4.7: Fitting parameters for Dimer MPW GSB recovery (665 nm).

Fluence [exc/MPW] / Solvent; Temp	Φ_1 (ps^{-1})	A_1	Φ_2 (ps^{-1})	A_2
0.25 / Buffer; 295 K	0.0211 ± 0.0018	0.501 ± 0.005	0.00130 ± 0.00005	0.48 ± 0.02
0.5 / Buffer; 295 K	0.0100 ± 0.0018	0.288 ± 0.021	0.00093 ± 0.00002	0.51 ± 0.03
1.0 / Buffer; 295 K	0.023 ± 0.003	0.380 ± 0.017	0.00092 ± 0.00002	0.67 ± 0.03
1.5 / Buffer; 295 K	0.019 ± 0.006	0.275 ± 0.007	0.0008 ± 0.0001	0.52 ± 0.05
0.1 / Glycerol; 77 K	0.018 ± 0.005	0.09 ± 0.03	0.00059 ± 0.00006	0.44 ± 0.10
0.66 / Glycerol; 77 K	0.009 ± 0.002	0.12 ± 0.04	0.00052 ± 0.00003	0.49 ± 0.14
2.0 / Glycerol; 77 K	0.0161	0.155	0.000793	0.5383
0.1 / Glycerol; 295 K	0.016 ± 0.003	0.42 ± 0.05	0.0013 ± 0.0001	0.38 ± 0.05
0.7 / Glycerol; 295 K	0.014 ± 0.002	0.30 ± 0.05	0.00093 ± 0.00002	0.41 ± 0.05
1.5 / Glycerol; 295 K	0.014 ± 0.001	0.24 ± 0.01	0.00082 ± 0.00006	0.52 ± 0.08

Table 4.8: Fitting parameters for Control 2R Dimer GSB recovery (665 nm).

Fluence [exc/MPW] / Solvent; Temp	Φ_1 (ps^{-1})	A_1	Φ_2 (ps^{-1})	A_2
0.5 / Buffer; 295 K	0.019 ± 0.003	0.108 ± 0.003	0.00088 ± 0.00005	0.76 ± 0.02
1.0 / Buffer; 295 K	0.026 ± 0.005	0.140 ± 0.002	0.0011 ± 0.0001	0.75 ± 0.01
3.0 / Buffer; 295 K	0.0241 ± 0.0008	0.097 ± 0.003	0.0011 ± 0.0005	0.77 ± 0.02
5.0 / Buffer; 295 K	0.012 ± 0.002	0.10 ± 0.01	0.00092 ± 0.00008	0.74 ± 0.05
0.50 / Glycerol; 77 K	-	-	0.00049 ± 0.00002	0.90 ± 0.06
1.0 / Glycerol; 77 K	-	-	0.0006 ± 0.0001	0.81 ± 0.05
3.0 / Glycerol; 77 K	-	-	0.0006 ± 0.0001	0.871 ± 0.003
0.5 / Glycerol; 295 K	-	-	0.00072 ± 0.00003	0.85 ± 0.09
1.25 / Glycerol; 295 K	-	-	0.0008 ± 0.0001	0.78 ± 0.15
2.5 / Glycerol; 295 K	-	-	0.0008485	0.1987

Table 4.9: Fitting parameters for Control 2R Dimer GSB recovery (665 nm).

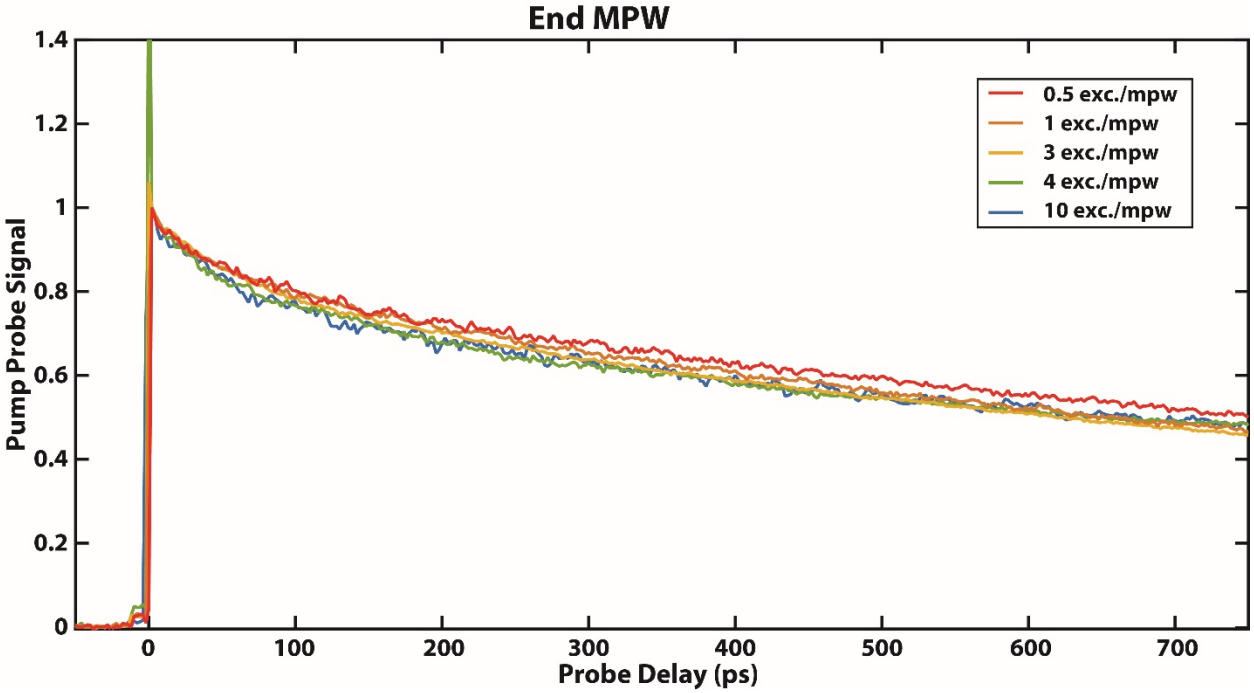

Figure 4.14: Fluence dependent kinetics of End MPW at room temperature, traces taken from 665 nm.

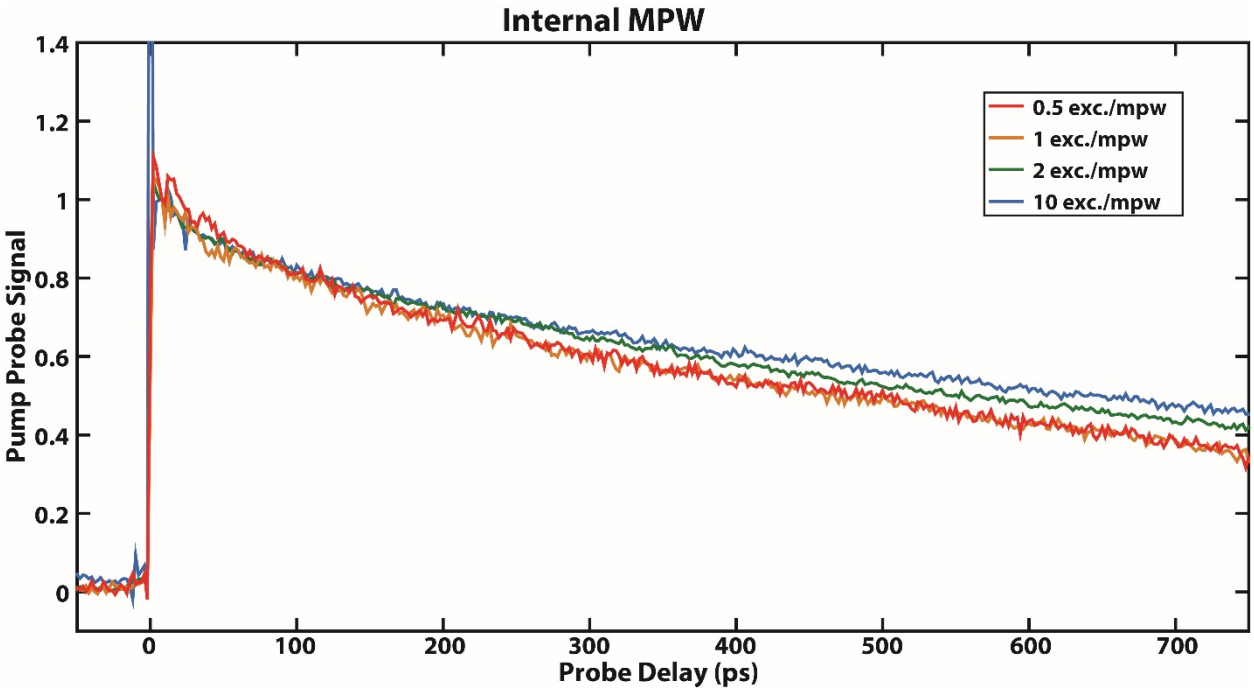

Figure 4.15: Fluence dependent kinetics of Internal MPW at room temperature, traces taken from 665 nm.

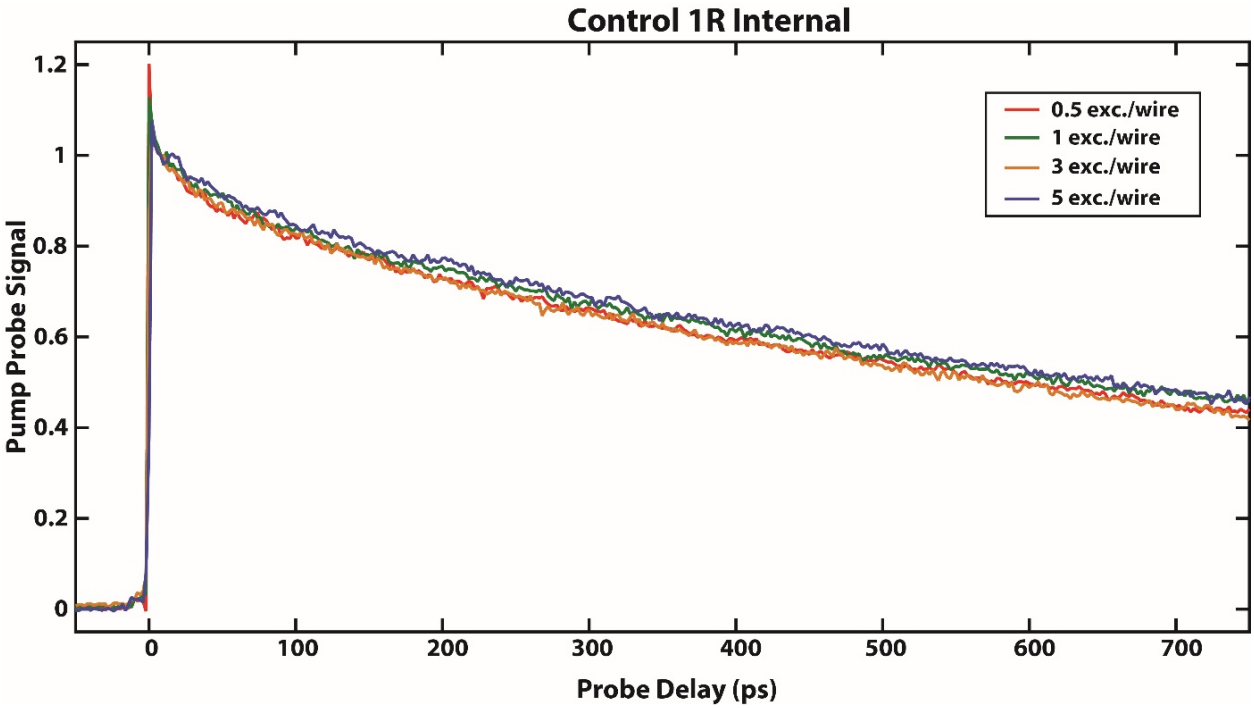

Figure 4.16: Fluence dependent kinetics of Control 1R Internal in buffer at room temperature, traces taken from 665 nm.

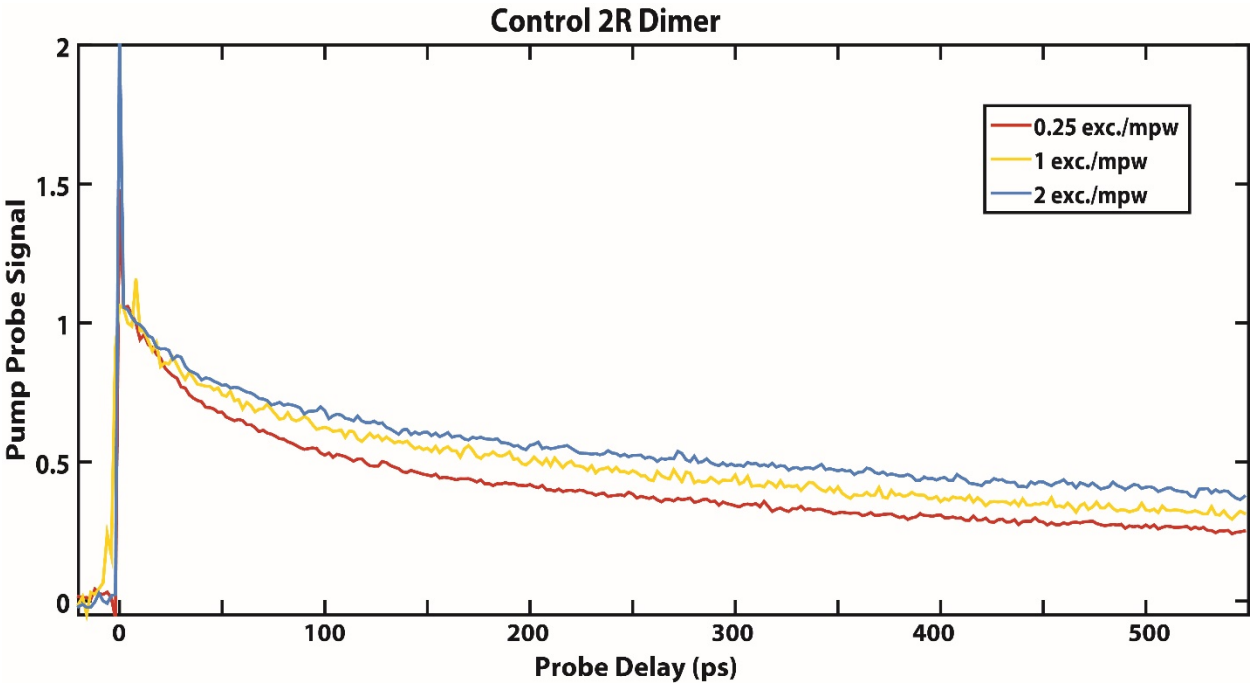

Figure 4.17: Fluence dependent kinetics of Control 2R Dimer in buffer at room temperature, traces taken from 665 nm.

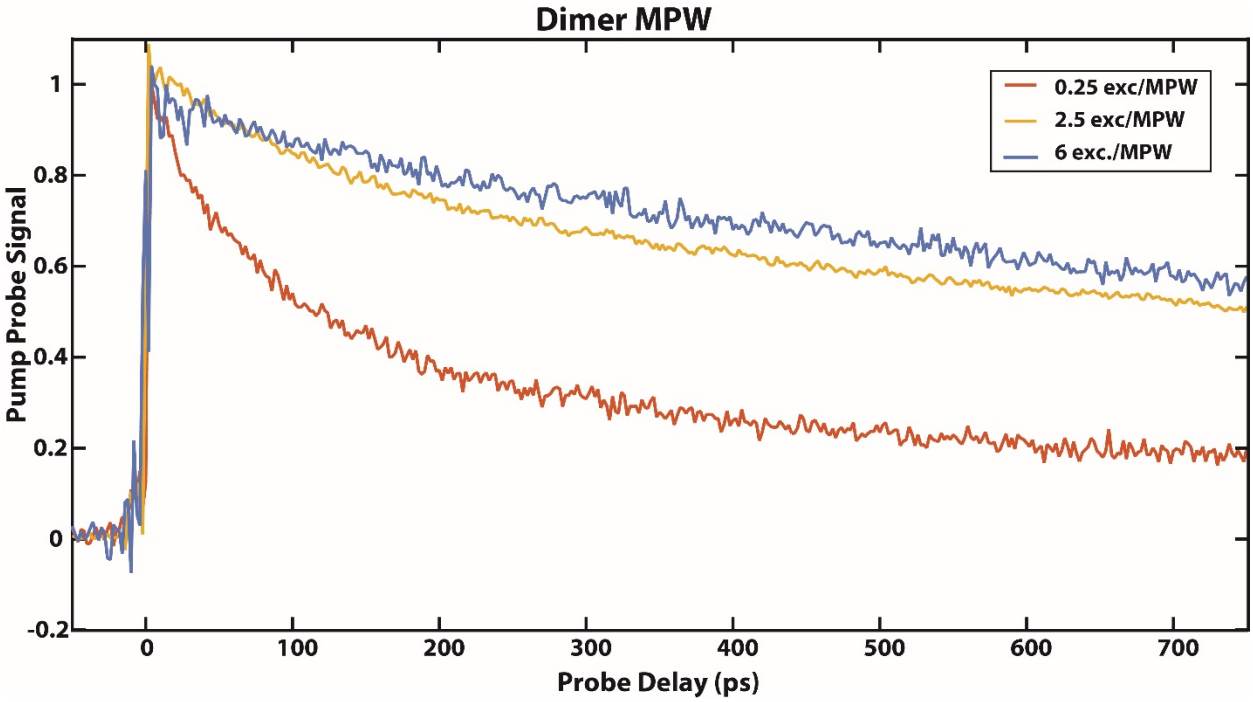

Figure 4.18: Fluence dependent kinetics of Dimer MPW in 3:1 glycerol:buffer at room temperature, traces taken from 665 nm.

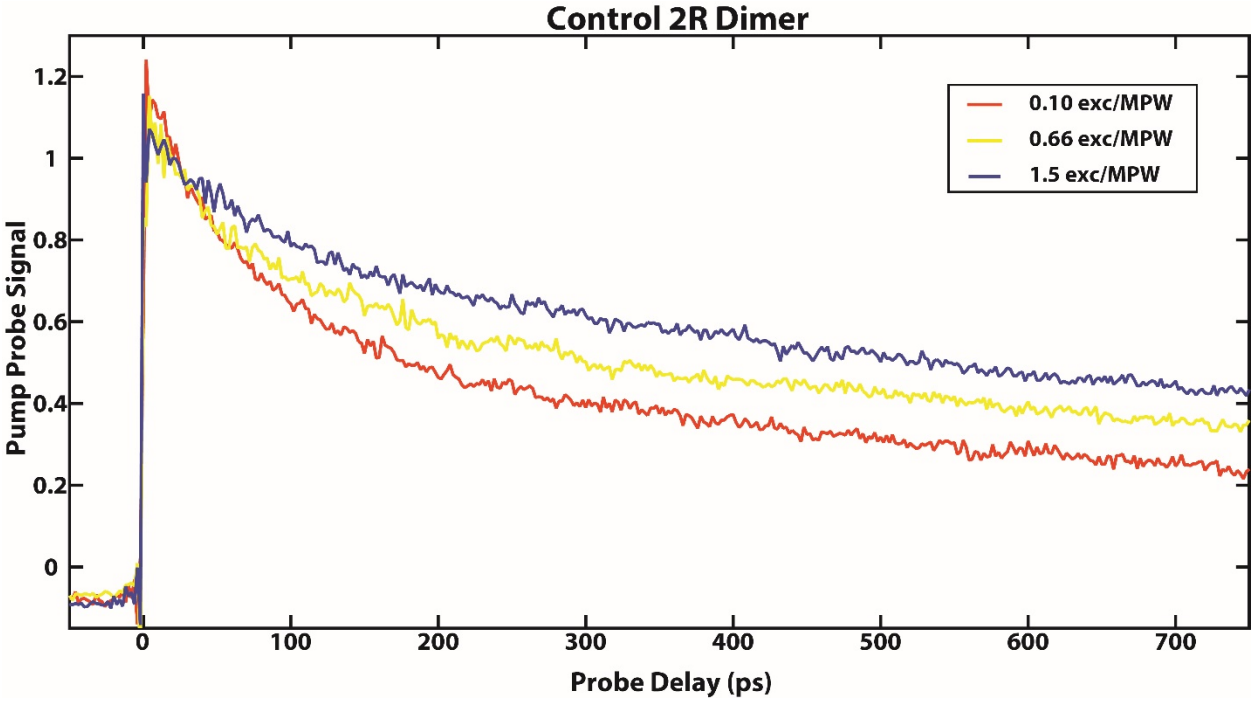

Figure 4.19: Fluence dependent kinetics Control 2R Dimer in 3:1 glycerol:buffer at room temperature, traces taken from 665 nm.

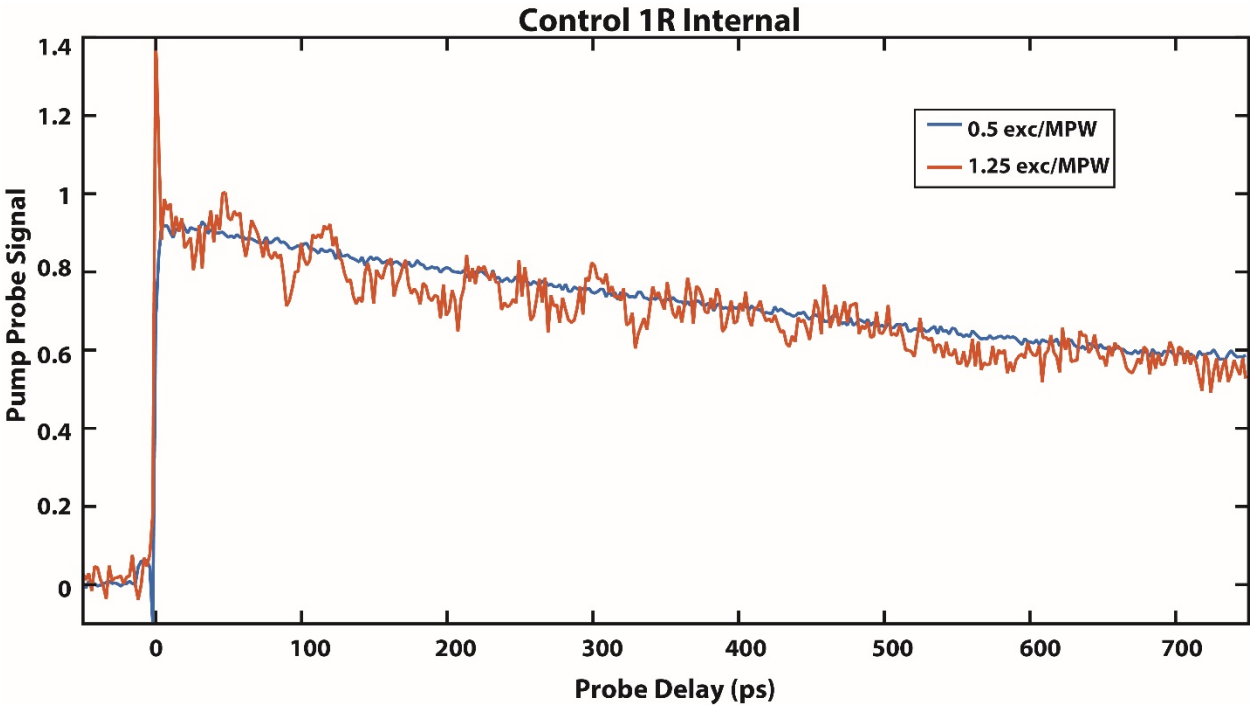

Figure 4.20: Fluence dependent kinetics of Control 1R Internal in 3:1 glycerol:buffer at room temperature, traces taken from 665 nm.

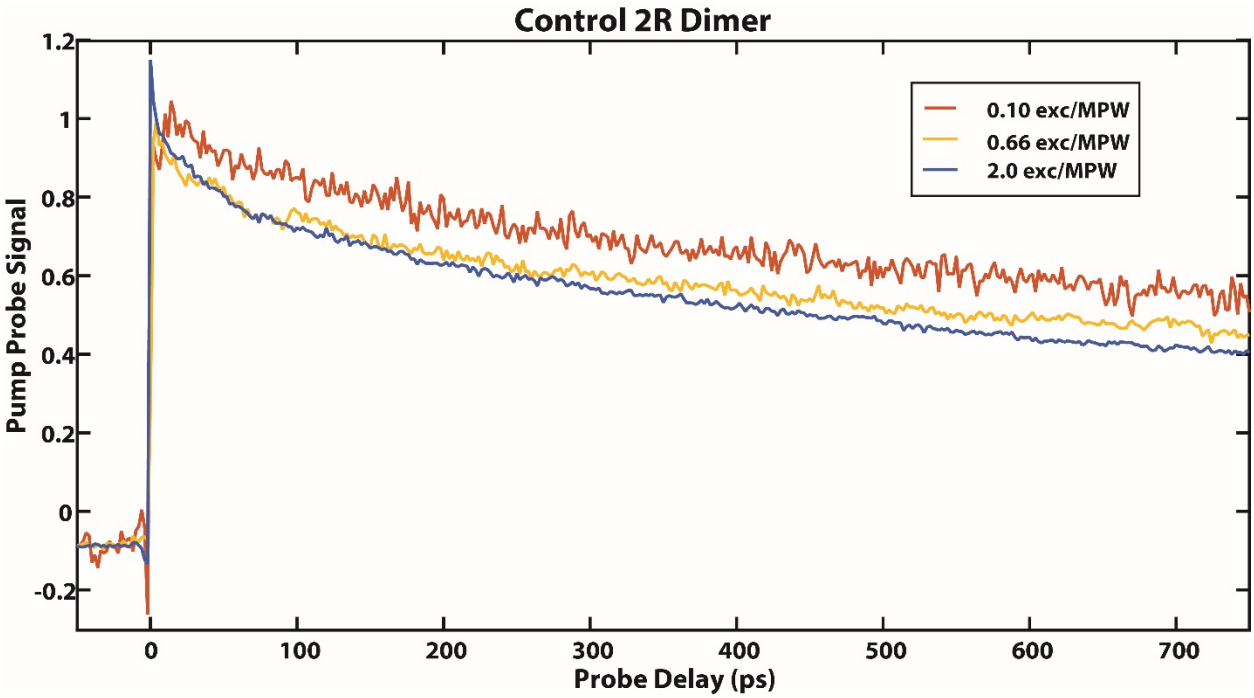

Figure 4.21: Fluence dependent kinetics of Control 2R Dimer in 3:1 glycerol:buffer at 77 K, traces taken from 665 nm.

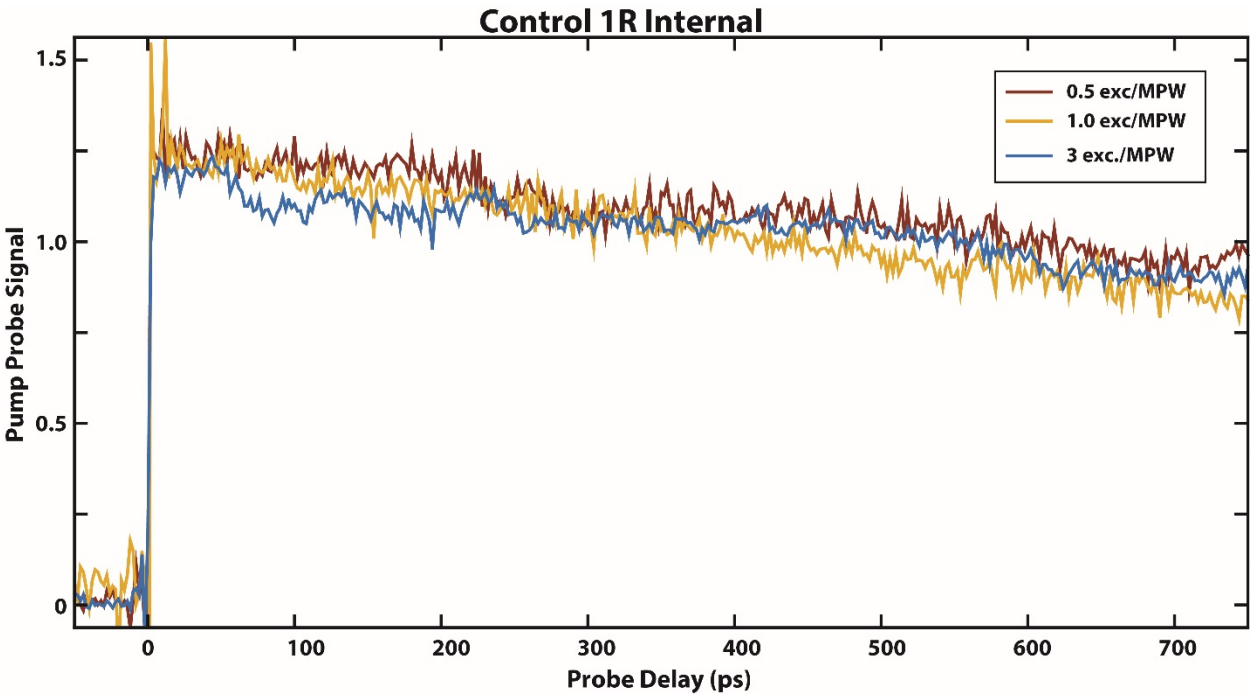

Figure 4.22: Fluence dependent kinetics Control 1R Internal in 3:1 glycerol:buffer at 77 K, traces taken from 665 nm.

REFERENCES

[1] Richard J. Mazuski, Sebastián A. Díaz, Ryan E. Wood, Lawson T. Lloyd, William P. Klein, Divita Mathur, Joseph S. Melinger, Gregory S. Engel, and Igor L. Medintz. Ultrafast excitation transfer in cy5 dna photonic wires displays dye conjugation and excitation energy dependency. *The Journal of Physical Chemistry Letters*, 0(0):4163–4172, 2020. PMID: 32391695.

[2] Hieu Bui, Sebastián A. Díaz, Jake Fontana, Matthew Chiriboga, Remi Veneziano, and Igor L. Medintz. Utilizing the organizational power of dna scaffolds for new nanophotonic applications. *Advanced Optical Materials*, 7(18):1900562, 2019.

[3] William P. Klein, Sebastián A. Díaz, Susan Buckhout-White, Joseph S. Melinger, Paul D. Cunningham, Ellen R. Goldman, Mario G. Ancona, Wan Kuang, and Igor L. Medintz. Utilizing homofret to extend dna-scaffolded photonic networks and increase light-harvesting capability. *Advanced Optical Materials*, 6(1):1700679, 2018.

[4] Mike Heilemann, Philip Tinnefeld, Gabriel Sanchez Mosteiro, Maria Garcia Parajo, Niek F. Van Hulst, and Markus Sauer. Multistep energy transfer in single molecular photonic wires. *Journal of the American Chemical Society*, 126(21):6514–6515, 2004. PMID: 15161254.

[5] Bo Albinsson, Jonas K. Hannestad, and Karl Börjesson. Functionalized dna nanostructures for light harvesting and charge separation. *Coordination Chemistry Reviews*, 256(21):2399 – 2413, 2012. Solar Fuels- by invitation only.

[6] Richard W. Wagner and Jonathan S. Lindsey. A molecular photonic wire. *Journal of the American Chemical Society*, 116(21):9759–9760, 1994.

[7] Tim Schröder, Max B. Scheible, Florian Steiner, Jan Vogelsang, and Philip Tin-

nefeld. Interchromophoric interactions determine the maximum brightness density in dna origami structures. *Nano Letters*, 19(2):1275–1281, 2019.

[8] Jonathan S. Huff, Paul H. Davis, Allison Christy, Donald L. Kellis, Nirmala Kandadai, Zi S. D. Toa, Gregory D. Scholes, Bernard Yurke, William B. Knowlton, and Ryan D. Pensack. Dna-templated aggregates of strongly coupled cyanine dyes: Nonradiative decay governs exciton lifetimes. *The Journal of Physical Chemistry Letters*, 10(10):2386–2392, 2019.

[9] Jonas K. Hannestad, Simon R. Gerrard, Tom Brown, and Bo Albinsson. Self-assembled dna-based fluorescence waveguide with selectable output. *Small*, 7(22):3178–3185, 2011.

[10] Jonas K. Hannestad, Peter Sandin, and Bo Albinsson. Self-assembled dna photonic wire for long-range energy transfer. *Journal of the American Chemical Society*, 130(47):15889–15895, 2008. PMID: 18975869.

[11] Carl W. Brown, Susan Buckhout-White, Sebastián A. Díaz, Joseph S. Melinger, Mario G. Ancona, Ellen R. Goldman, and Igor L. Medintz. Evaluating dye-labeled dna dendrimers for potential applications in molecular biosensing. *ACS Sensors*, 2(3):401–410, 2017.

[12] Hieu Bui, Carl W. Brown III, Susan Buckhout-White, Sebastián A. Díaz, Michael H. Stewart, Kimihiro Susumu, Eunkeu Oh, Mario G. Ancona, Ellen R. Goldman, and Igor L. Medintz. Transducing protease activity into dna output for developing smart bionanosensors. *Small*, 15(14):1805384, 2019.

[13] Seung Hyuk Back, Jin Hyuk Park, Chunzhi Cui, and Dong June Ahn. Bio-recognitive photonics of a dna-guided organic semiconductor. *Nature Communications*, 7(1):10234, 2016.

[14] Melissa Massey, Igor L. Medintz, Mario G. Ancona, and W. Russ Algar. Time-gated fret and dna-based photonic molecular logic gates: And, or, nand, and nor. *ACS Sensors*, 2(8):1205–1214, 2017. PMID: 28787151.

[15] Nicolas P. D. Sawaya, Dmitrij Rappoport, Daniel P. Tabor, and Alán Aspuru-Guzik. Excitonics: A set of gates for molecular exciton processing and signaling. *ACS Nano*, 12(7):6410–6420, 2018. PMID: 29920202.

[16] Susan Buckhout-White, Christopher M. Spillmann, W. Russ Algar, Ani Khachatrian, Joseph S. Melinger, Ellen R. Goldman, Mario G. Ancona, and Igor L. Medintz. Assembling programmable fret-based photonic networks using designer dna scaffolds. *Nature Communications*, 5(1):5615, 2014.

[17] Lili Wang, Graham B. Griffin, Alice Zhang, Feng Zhai, Nicholas E. Williams, Richard F. Jordan, and Gregory S. Engel. Controlling quantum-beating signals in 2d electronic spectra by packing synthetic heterodimers on single-walled carbon nanotubes. *Nature Chemistry*, 9(3):219–225, 2017.

[18] Dugan Hayes, Graham B. Griffin, and Gregory S. Engel. Engineering coherence among excited states in synthetic heterodimer systems. *Science*, 340(6139):1431–1434, 2013.

[19] Divita Mathur, William P. Klein, Matthew Chiriboga, Hieu Bui, Eunkeu Oh, Rafaela Nita, Jawad Naciri, Paul Johns, Jake Fontana, Sebastián A. Díaz, and Igor L. Medintz. Analyzing fidelity and reproducibility of dna templated plasmonic nanostructures. *Nanoscale*, 11:20693–20706, 2019.

[20] Luvena L. Ong, Nikita Hanikel, Omar K. Yaghi, Casey Grun, Maximilian T. Strauss, Patrick Bron, Josephine Lai-Kee-Him, Florian Schueder, Bei Wang, Pengfei Wang, Jocelyn Y. Kishi, Cameron Myhrvold, Allen Zhu, Ralf Jungmann, Gaetan Bellot, Yonggang

Ke, and Peng Yin. Programmable self-assembly of three-dimensional nanostructures from 10,000 unique components. *Nature*, 552(7683):72–77, 2017.

[21] Sebastián A. Díaz, Susan Buckhout-White, Mario G. Ancona, Christopher M. Spillmann, Ellen R. Goldman, Joseph S. Melinger, and Igor L. Medintz. Extending dna-based molecular photonic wires with homogeneous förster resonance energy transfer. *Advanced Optical Materials*, 4(3):399–412, 2016.

[22] Francesca Nicoli, Anders Barth, Wooli Bae, Fabian Neukirchinger, Alvaro H. Crevenna, Don C. Lamb, and Tim Liedl. Directional photonic wire mediated by homo-förster resonance energy transfer on a dna origami platform. *ACS Nano*, 11(11):11264–11272, 2017. PMID: 29063765.

[23] Nicole Kretschy, Matej Sack, and Mark M. Somoza. Sequence-dependent fluorescence of cy3- and cy5-labeled double-stranded dna. *Bioconjugate Chemistry*, 27(3):840–848, 2016. PMID: 26895222.

[24] Joseph S. Melinger, Ani Khachatrian, Mario G. Ancona, Susan Buckhout-White, Ellen R. Goldman, Christopher M. Spillmann, Igor L. Medintz, and Paul D. Cunningham. Fret from multiple pathways in fluorophore-labeled dna. *ACS Photonics*, 3(4):659–669, 2016.

[25] Francesca Nicoli, Matthias K. Roos, Elisa A. Hemmig, Marco Di Antonio, Regina de Vivie-Riedle, and Tim Liedl. Proximity-induced h-aggregation of cyanine dyes on dna-duplexes. *The Journal of Physical Chemistry A*, 120(50):9941–9947, 2016. PMID: 27934475.

[26] William P. Klein, Brian S. Rolczynski, Sean M. Oliver, Reza Zadegan, Susan Buckhout-White, Mario G. Ancona, Paul D. Cunningham, Joseph S. Melinger, Patrick M. Vora, Wan Kuang, Igor L. Medintz, and Sebastián A. Díaz. Dna origami chromophore scaffold

exploiting homofret energy transport to create molecular photonic wires. *ACS Applied Nano Materials*, 3(4):3323–3336, 2020.

[27] Hiromu Kashida, Hayato Kawai, Ryoko Maruyama, Yuta Kokubo, Yasuyuki Araki, Takehiko Wada, and Hiroyuki Asanuma. Quantitative evaluation of energy migration between identical chromophores enabled by breaking symmetry. *Communications Chemistry*, 1(1):91, 2018.

[28] Hiroyuki Asanuma, Taiga Fujii, Tomohiro Kato, and Hiromu Kashida. Coherent interactions of dyes assembled on dna. *Journal of Photochemistry and Photobiology C: Photochemistry Reviews*, 13(2):124 – 135, 2012. Photochemical Methodology Utilized in Chemical Biology.

[29] Brittany L. Cannon, Lance K. Patten, Donald L. Kellis, Paul H. Davis, Jeunghoon Lee, Elton Graugnard, Bernard Yurke, and William B. Knowlton. Large davydov splitting and strong fluorescence suppression: An investigation of exciton delocalization in dna-templated holliday junction dye aggregates. *The Journal of Physical Chemistry A*, 122(8):2086–2095, 2018. PMID: 29420037.

[30] Jerker Widengren and Petra Schwille. Characterization of photoinduced isomerization and back-isomerization of the cyanine dye cy5 by fluorescence correlation spectroscopy. *The Journal of Physical Chemistry A*, 104(27):6416–6428, 2000.

[31] Zhengxi Huang, Dongmei Ji, Sufan Wang, Andong Xia, Felix Koberling, Matthias Patting, and Rainer Erdmann. Spectral identification of specific photophysics of cy5 by means of ensemble and single molecule measurements. *The Journal of Physical Chemistry A*, 110(1):45–50, 2006. PMID: 16392838.

[32] Chaoyang Fan, Jung-Cheng Hsiang, and Robert M. Dickson. Optical modulation and selective recovery of cy5 fluorescence. *ChemPhysChem*, 13(4):1023–1029, 2012.

[33] Zixuan Hu, Gregory S. Engel, Fahhad H. Alharbi, and Sabre Kais. Dark states and delocalization: Competing effects of quantum coherence on the efficiency of light harvesting systems. *The Journal of Chemical Physics*, 148(6):064304, 2018.

[34] Peter D. Dahlberg, Andrew F. Fidler, Justin R. Caram, Phillip D. Long, and Gregory S. Engel. Energy transfer observed in live cells using two-dimensional electronic spectroscopy. *The Journal of Physical Chemistry Letters*, 4(21):3636–3640, 2013.

[35] Peter D. Dahlberg, Po-Chieh Ting, Sara C. Massey, Marco A. Allodi, Elizabeth C. Martin, C. Neil Hunter, and Gregory S. Engel. Mapping the ultrafast flow of harvested solar energy in living photosynthetic cells. *Nature Communications*, 8(1):988, 2017.

[36] Andrew F. Fidler, Ved P. Singh, Phillip D. Long, Peter D. Dahlberg, and Gregory S. Engel. Dynamic localization of electronic excitation in photosynthetic complexes revealed with chiral two-dimensional spectroscopy. *Nature Communications*, 5(1):3286, 2014.

[37] Andreas C. Jakowetz, Ture F. Hinrichsen, Laura Ascherl, Torben Sick, Mona Calik, Florian Auras, Dana D. Medina, Richard H. Friend, Akshay Rao, and Thomas Bein. Excited-state dynamics in fully conjugated 2d covalent organic frameworks. *Journal of the American Chemical Society*, 141(29):11565–11571, 2019. PMID: 31305073.

[38] Ryan E. Wood, Lawson T. Lloyd, Fauzia Mujid, Lili Wang, Marco A. Allodi, Hui Gao, Richard Mazuski, Po-Chieh Ting, Saien Xie, Jiwoong Park, and Gregory S. Engel. Evidence for the dominance of carrier-induced band gap renormalization over biexciton formation in cryogenic ultrafast experiments on mos2 monolayers. *The Journal of Physical Chemistry Letters*, 11(7):2658–2666, 2020. PMID: 32168454.

[39] Tsu Ju Fu and Nadrian C. Seeman. Dna double-crossover molecules. *Biochemistry*, 32(13):3211–3220, 1993. PMID: 8461289.

[40] Sebastián A. Díaz, Sean M. Oliver, David A. Hastman, Igor L. Medintz, and Patrick M. Vora. Increased transfer efficiency from molecular photonic wires on solid substrates and cryogenic conditions. *The Journal of Physical Chemistry Letters*, 9(13):3654–3659, 2018. PMID: 29893572.

[41] Paul D. Cunningham, Young C. Kim, Sebastián A. Díaz, Susan Buckhout-White, Divita Mathur, Igor L. Medintz, and Joseph S. Melinger. Optical properties of vibronically coupled cy3 dimers on dna scaffolds. *The Journal of Physical Chemistry B*, 122(19):5020–5029, 2018. PMID: 29698610.

[42] Jakub Dostál, Franziska Fennel, Federico Koch, Stefanie Herbst, Frank Würthner, and Tobias Brixner. Direct observation of exciton–exciton interactions. *Nature Communications*, 9(1):2466, 2018.

[43] Lili Wang, Adolfas K. Gaigalas, and Vytas Reipa. Optical properties of alexa™ 488 and cy™5 immobilized on a glass surface. *BioTechniques*, 38(1):127–132, 2005. PMID: 15679095.

[44] R. [van Grondelle], H. Bergström, V. Sundström, and T. Gillbro. Energy transfer within the bacteriochlorophyll antenna of purple bacteria at 77 k, studied by picosecond absorption recovery. *Biochimica et Biophysica Acta (BBA) - Bioenergetics*, 894(2):313 – 326, 1987.

[45] B. Gao, H. Wang, H. Wang, Z. Yang, L. Wang, Y. Jiang, Y. Hao, Q. Chen, and H. Sun. Investigation of polaron pair dynamics in poly(3-hexylthiophene) film by time resolved spectroscopy. *IEEE Journal of Quantum Electronics*, 48(3):425–432, 2012.

[46] Brittany L. Cannon, Donald L. Kellis, Lance K. Patten, Paul H. Davis, Jeunghoon Lee, Elton Graugnard, Bernard Yurke, and William B. Knowlton. Coherent exciton delo-

calization in a two-state dna-templated dye aggregate system. *The Journal of Physical Chemistry A*, 121(37):6905–6916, 2017. PMID: 28813152.

[47] Henk Fidder, Jasper Knoester, and Douwe A. Wiersma. Observation of the one-exciton to two-exciton transition in a j aggregate. *The Journal of Chemical Physics*, 98(8):6564–6566, 1993.

[48] Adelaida Sanchez-Galvez, Patricia Hunt, Michael A. Robb, Massimo Olivucci, Thom Vreven, and H. Bernhard Schlegel. Ultrafast radiationless deactivation of organic dyes: Evidence for a two-state two-mode pathway in polymethine cyanines. *Journal of the American Chemical Society*, 122(12):2911–2924, 2000.

[49] Srigokul Upadhyayula, Vicente Nuñez, Eli M. Espinoza, Jillian M. Larsen, Duoduo Bao, Dewen Shi, Jenny T. Mac, Bahman Anvari, and Valentine I. Vullev. Photoinduced dynamics of a cyanine dye: parallel pathways of non-radiative deactivation involving multiple excited-state twisted transients. *Chem. Sci.*, 6:2237–2251, 2015.

[50] Gregory D. Scholes, Graham R. Fleming, Alexandra Olaya-Castro, and Rienk van Grondelle. Lessons from nature about solar light harvesting. *Nature Chemistry*, 3(10):763–774, 2011.

[51] Haibin Zheng, Justin R. Caram, Peter D. Dahlberg, Brian S. Rolczynski, Subha Viswanathan, Dmitriy S. Dolzhnikov, Amir Khadivi, Dmitri V. Talapin, and Gregory S. Engel. Dispersion-free continuum two-dimensional electronic spectrometer. *Appl. Opt.*, 53(9):1909–1917, Mar 2014.

CHAPTER 5

OPTICAL RESONANCE IMAGING: AN OPTICAL ANALOG TO MRI WITH SUB-DIFFRACTION-LIMITED CAPABILITIES

5.1 Overview

The following chapter is adapted from [1] with full permission.

The following research is a theoretical description of an optical analog to magnetic resonance imaging. Once experimentally verified, this technique could revolutionize the way ultrafast mesoscale dynamics are examined. Currently, spectral signature need to be analyzed across time to see evolution, but the direct imaging of excitons would enable statistically distinct paths to be seen. While single nanometer resolution might outside current experimental viability, excitons with long path lengths could be visible within the micrometer regime.

5.2 Introduction to Ultrafast Subdiffraction-Limited Imaging

The diffraction limit theoretically constrains an imaging system's spatial resolution,[2, 3] and yet several approaches can resolve structures below the diffraction limit. Near-field techniques require having a small aperture, or scattering material in close proximity (<10 nm) to the sample to measure the electromagnetic fields before they propagate into the radiation zone [4, 5, 6], while in the far-field some techniques collect fluorescence from a diffuse array of emitters and localize the source to a sub-diffraction-limited spot [7, 8, 9]. Other far-field fluorescence techniques require illumination of the widefield image with a structured laser field to generate interference effects in the illumination that effectively illuminate a sub-diffraction limited slice of the sample.[10, 11] All approaches require milliseconds to seconds

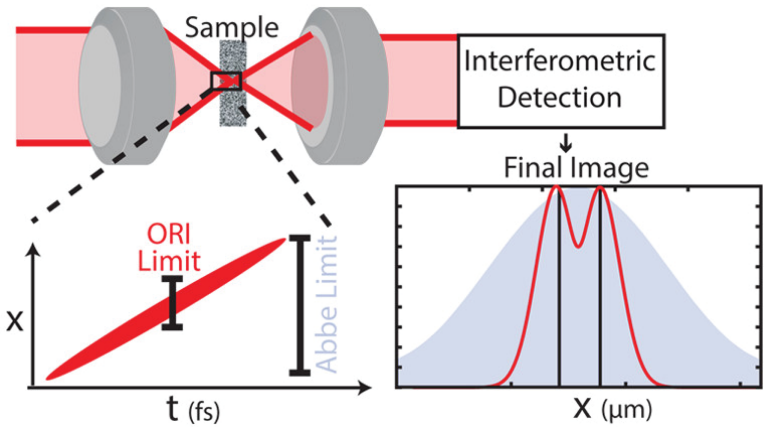

Figure 5.1: Three components allow ORI to achieve ultrafast sub-diffraction-limited imaging. Beginning (clockwise from bottom-left) with pulse front tilt (PFT) in beam three of a standard four-pulse ultrafast experiment, we can stimulate a photon echo at different points of time across a diffraction-limited spot, akin to sweeping a spotlight across an excited-state population. Since we can collect multiple points of information across this diffraction-limited spot, we are able to beat the diffraction limit. Heterodyne detection makes this acquisition of information possible, functioning essentially like a stop-watch to time the arrival of different portions of the emitted signal.

of collection time to produce an image. Thus, an apparatus can overcome the diffraction limit with these techniques but cannot simultaneously observe dynamical processes on timescales faster than the acquisition time [12]. Faster dynamics, such as those on the femtosecond (fs) to picosecond (ps) timescale, play a critical role in diverse physical and chemical processes ranging from energy transfer in photosynthetic light harvesting [13, 14, 15] and excitonic diffusion in materials [16, 17, 18], to photochemistry[19, 20] and the molecular dynamics of liquids [21, 22, 23]. ORI will allow access to these faster dynamics.

Leveraging time to gain spatial information is always necessary to beat the diffraction limit in the optical regime. For example, the first successful approach to far-field, sub-diffraction-limited imaging in the optical region of the spectrum exploited the time domain by stimulating emission prior to fluorescence. STimulated-Emission Depletion (STED) microscopy [24, 8] makes use of a diffraction-limited excitation beam that is followed in short succession by a toroidal depletion beam. The depletion beam stimulates emission from the

outside edge of the diffraction-limited spot, leaving an excitation area that is smaller than that originally illuminated by the excitation beam, thus decreasing the point-spread function and enabling superresolution imaging of diverse systems ranging from cells to nanomaterials [25]. Fluorescence-based superresolution techniques such as PALM[7] or STORM[9] use the spatial information from different emitters collected at different times to produce a superresolution image, whereas near-field techniques, like NSOM, as the name implies, must raster scanning over different positions at different times.

Superresolution at radio frequencies, also known as Magnetic resonance imaging (MRI), has shown that it is possible to decouple an image's resolution from the wavelength of light by creating spatially-defined magnetic field gradients across a sample [26]. The gradients change the Larmor frequency of the precessing nuclear spins (and thus the emitted photon energy) as a function of spatial position.[27, 28] The diffraction limit does not constrain the differences in photon energy, which can be measured to higher precision than their source could be imaged with optics. As a result, MRI maps a spatial coordinate to energy and uses meter-long light waves to generate images with millimeter-scale resolution, which has transformed the fields of medicine and neuroscience.[29]

In this work, we propose an optical analog of MRI to achieve widefield, sub-diffraction-limited imaging using ultrashort (femtosecond) laser pulses, which we call optical resonance imaging (ORI). To gain information about dynamics faster than the nanosecond timescale of fluorescence, ORI employs a three-pulse, photon-echo pulse sequence to stimulate emission from the sample. Unlike other photon-echo measurements, the stimulating pulse has significant pulse-front tilt. As such, ORI maps a lateral spatial coordinate of the sample to the emission time of the signal. The ultrashort character of the tilted pulse at the sample ensures that the emission of a photon-echo signal will occur at different times. The ultrafast temporal resolution makes sub-diffraction-limited imaging possible by measuring a difference in arrival time at the detector of different parts of the signal with high precision. In essence,

we exploit the same approach as in MRI, but instead of mapping space to energy, we map space to the time of emission. Being Fourier conjugates for electromagnetic fields, both time and energy allow us to escape the diffraction limit in a similar way, while the diffraction limit still determines time-independent, wave-like properties of the EM field such as the focal-spot size and pulse-front tilt that can be generated. We discuss below the conditions necessary for optical resonance imaging, and the possibilities for widefield, superresolution ultrafast imaging.

5.3 Results and Discussion of Theoretical Simulation of ORI

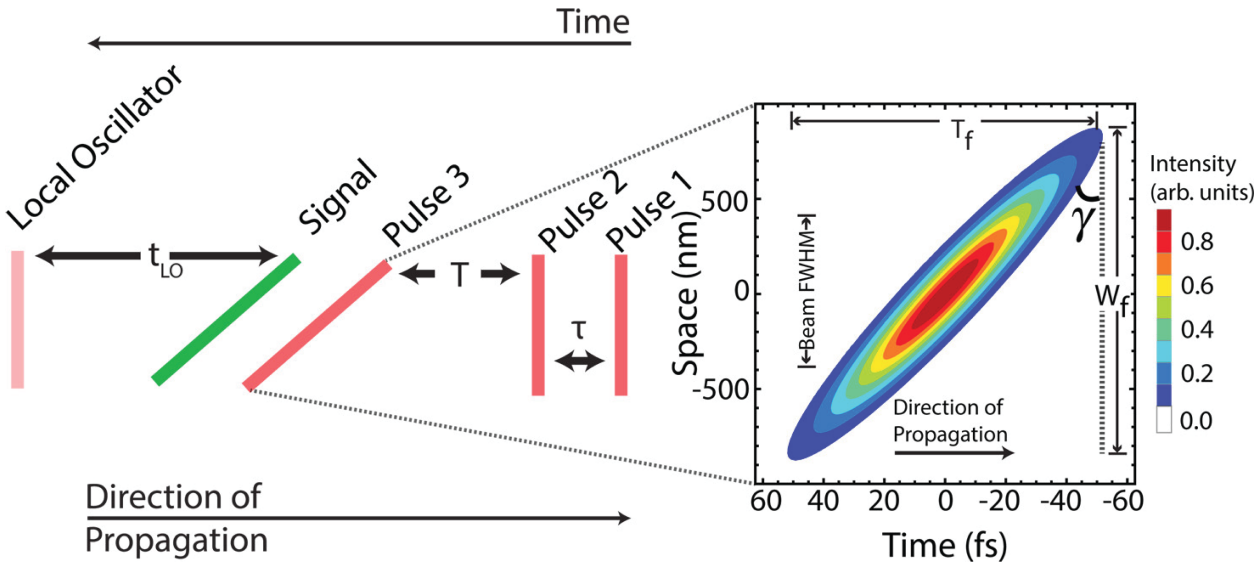

Figure 5.2: The pulse sequence for ORI. Pulses 1 and 2 are separated by time τ and prepare a population state which evolves for the waiting time T. pulse 3 stimulates emission of a photon echo from the sample. Since pulse 3 has significant pulse-front tilt, different parts of the sample will emit an echo at different times. The signal is emitted some time after pulse 3 and is shown in green. The right portion of the figure shows a plot of the calculated spatial and temporal extent of the third pulse with pulse-front tilt, focused at the sample using f/0.5 optics. The contours are plotted for the pulse intensity. A representative phase front of the pulse is illustrated by the dashed black line, and the angle γ defines the pulse-front tilt, W_f is the focused spot size and T_f is the length swept out by the pulse-front tilt. At the focus, the FWHM of the tilted pulse in the direction of propagation is 15 fs, the same as for the flat pulses (pulses 1 & 2).

Two key concepts from ultrafast nonlinear spectroscopy enable ORI measurements – the stimulated emission of a photon echo, and interferometric heterodyne detection. A photon echo results from a third-order nonlinear optical process [30, 31]. Three separate interactions of the sample with an optical electric field (in this case, three laser pulses) generate a polarization, $P^{(3)}(\tau, T, t_R)$, in the material that emits a signal, $E^{(3)}_{sig}$, where τ is the time between pulses 1 and 2, T is the time between pulses 2 and 3, and t_R is the time after pulse 3 interacts with the sample. Third-order perturbation theory ultimately shows that $P^{(3)}(\tau, T, t_R)$ is the time-ordered convolution of the material response function, $R^{(3)}(\tau, T, t_R)$, with the three laser pulses that interact with the sample at different times. In the impulsive limit, where the laser pulse duration is much shorter than the timescale of the dynamics of interest, the laser pulses can be thought of as delta functions, yielding a direct measurement of the response function. The photon-echo response can be isolated experimentally from other contributions to $E^{(3)}_{sig}(t)$ by using a phase-matching geometry of the input beams that selects for the rephasing Liouville space pathways [32, 33].

Beams with pulse-front tilt (PFT) have a non-separable coupling between space and time that results in the intensity front of the beam having an angle relative to the phase front [34]. Fig. 5.2 shows the calculated intensity profile focused at the sample position of a beam that has PFT, with γ the angle between the pulse-front and the phase front. The electric field of a beam containing PFT can be written as

$$E(x, t) = E_x(x)E_t(t - px), \tag{5.1}$$

where E_x is the spatial component in a direction perpendicular to the direction of propagation, E_t is the temporal component, and p is the coupling term representing PFT. Thus, the arrival time of the electric field is also a function of the position along the beam. When a laser pulse with PFT is incident on a sample, different parts of the pulse interact with different parts of the sample at different times. This can be thought of as a time-dependent

local spot size that sweeps across the diffraction-limited, time-integrated focal spot.[35]

The pulse sequence needed for ORI can also be seen in Fig. 5.2. The pulse order and phase-matching condition are identical to a photon-echo pulse sequence used in 2D electronic or infrared spectroscopy [32]. The ORI pulse sequence differs from the sequence used for a conventional photon echo in that pulses 1 and 2 have no PFT, while the third pulse that stimulates the coherent emission and generates the photon-echo signal has a large angle of PFT. The PFT of the third pulse ensures that emission from different parts of the sample is stimulated at different times. This approach introduces a coupling between space and time into the third-order response of the system such that $R^3(\tau, T - px, t_R)$.

To make this coupling between space and time possible, one must deliver a pulse with PFT to the sample and have it retain its ultrashort character. One way to generate PFT can be found if we consider Eqn. 5.1. If we take the fourier transform of both space and time we find

$$\iint dx\, dt\, E_x(x)E_t(t - px)e^{i\omega t}e^{ik_x x} = \int dx\, E_x(x)E(\omega)e^{-i\omega px}e^{ik_x x} = E(k_x - p\omega)E(\omega), \tag{5.2}$$

where we have made two uses of the shift theorem of Fourier analysis [36]. Clearly then, $d\omega/dk = p$, which is closely related to angular dispersion, $d\theta_0/dk = p/k_0$, where θ_0 is defined as the propagation angle.[34] The angular dispersion gained by a beam after diffracting off of a grating will generate PFT when that beam is re-imaged. Experimental results in the literature have shown that when the grating generating a tilted pulse is appropriately imaged, the imaged pulse retains its femtosecond character across its entire focal spot [37]. Though not relevant to ORI, it should be noted that not all electric fields can be written as in Eqn. 5.1, so PFT can also be generated from the product of spatial chirp and group velocity dispersion in a beam [34].

We calculated the tilted beam profile of pulse 3 at the focus of an image producing

optical system by propagating a Gaussian beam through an optical system calculated using the Kostenbauder extension to ray-transfer matrices.[38] The result is shown in the right portion of Fig. 5.2. The Kostenbauder matrices allow us to follow spatio-temporal couplings as a beam propagates through an optical system. Traditional ray-transfer linear algebra involves 2-dimensional vectors (containing position and angle) and 2 x 2 ABCD matrices that represent the operations performed by different optical elements [39, 40]. Kostenbauder extended this analysis to include frequency and time using 4-dimensional vectors and a 4 x 4 matrix:

$$\begin{pmatrix} x \\ \theta \\ t \\ f \end{pmatrix}_{out} = \begin{pmatrix} A & B & 0 & \frac{\partial x_{out}}{\partial f_{in}} \\ C & D & 0 & \frac{\partial \theta_{out}}{\partial f_{in}} \\ \frac{\partial t_{out}}{\partial x_{in}} & \frac{\partial t_{out}}{\partial \theta_{in}} & 1 & \frac{\partial t_{out}}{\partial f_{in}} \\ 0 & 0 & 0 & 1 \end{pmatrix} \begin{pmatrix} x \\ \theta \\ t \\ f \end{pmatrix}_{in} = \begin{pmatrix} A & B & 0 & E \\ C & D & 0 & F \\ G & H & 1 & I \\ 0 & 0 & 0 & 1 \end{pmatrix} \begin{pmatrix} x \\ \theta \\ t \\ f \end{pmatrix}_{in}, \tag{5.3}$$

where A,B,C,D are defined in the same way as in the 2 x 2 ray transfer matrices. A Gaussian beam can be propagated through an optical system where the optical elements are represented by these matrices and the explicit inclusion of frequency and time enable calculations of beams with spatio-temporal coupling. The pulse plotted in Fig. 5.2 was calculated by starting with an initial beam radius of 5 mm, and a 15 fs FWHM pulse centered at 800 nm. A lens matrix transformation allows us to calculate the beam spot at the grating position. A grating with 2000 lines/mm and an incident angle of 42° was used to generate angular dispersion in the calculated field. This calculated electric field was propagated through an optical system consisting of two lenses spaced by the sum of their focal lengths, and the result shows that an ultrashort tilted pulse can be delivered to the focus of an optical system. A tilted pulse can only be focused down to the diffraction limit, denoted as W_f in Fig. 5.2. However, the pulse-front tilt ensures that sub-diffraction-limited parts of the pulse will interact with the sample at different times [35]. In essence, we exploit the interference

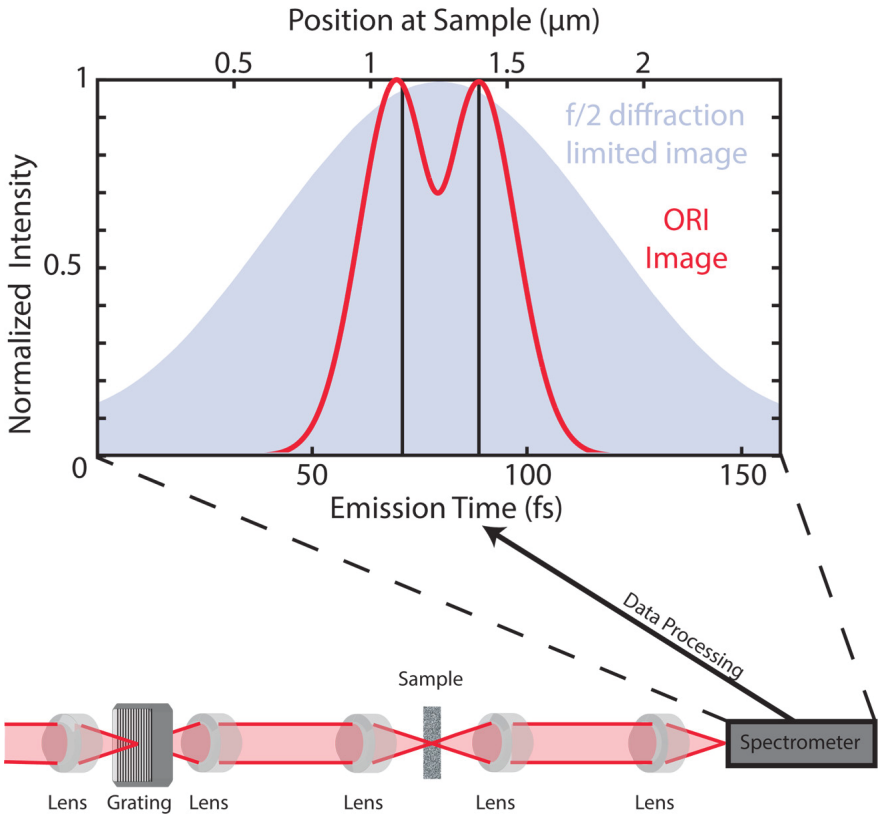

Figure 5.3: The calculated ORI image and diffraction-limited image. The ORI image is in red, with the dipole source positions identified with black lines. The the difference in the peak centers returns the spacing of the emitters. The diffraction-limited image of a set of individual, incoherent emitters located at the positions of the red lines and imaged with $f/2$ optics is shown in the filled trace behind. The bottom portion of the figure shows a possible optical apparatus that could generate ORI signals.

between different colors incident from different angles to generate a transform-limited pulse over a sub-diffraction limited area. More details about this calculation are available in the methods section and supplemental information.

Since the angle of PFT, γ, is defined as the angle of the intensity front of the pulse with respect to the phase fronts, we can calculate γ from the beam profile shown in Fig. 5.2 via the inverse tangent. We find $\gamma = tan^{-1}(\frac{T_f * c}{W_f}) = 87°$, where W_f and T_f are labeled in Fig. 5.2, and correspond to the size of the focused spot and the time it takes the beam to sweep over that spot respectively; c is the speed of light. The successful encoding of

space into the time-dependent polarization, $P^{(3)}(\tau, T - px, t_R)$, in the sample ensures that different parts of the sample will emit a photon echo at different times. We note that the three time intervals upon which $P^{(3)}$ depends result from the different arrival times of three independent ultrafast pulses. Thus, in addition to the spatial information, $P^{(3)}$ also contains all the spectral information that is contained in a measurement such as 2D electronic spectroscopy provided that all time intervals are scanned.

Interferometric heterodyne detection of the signal field, $E^{(3)}_{sig}$, measures the precise arrival time of the signal compared to a local-oscillator (LO) reference pulse [41, 42]. As in 2DES, a set of optics, often in a 4f imaging configuration, collect the emitted signal and focus both the signal and LO pulse into a spectrometer. The spectrometer converts the time-domain signals into the frequency domain and the resultant interference pattern between the LO and the signal is measured on a square-law detector. The frequency-domain signal on the detector can be expressed as

$$S(\omega) = \left| \int_{-\infty}^{\infty} dt \, (E_{LO}(t - t_{LO} + \phi) + E^{(3)}_{sig}(t)) e^{i\omega t} \right|^2, \tag{5.4}$$

$$S(\omega) = \left| e^{i\omega t_{LO} + \phi} E_{LO}(\omega) + E^{(3)}_{sig}(\omega) \right|^2, \tag{5.5}$$

$$S(\omega) = I_{LO} + I_{sig} + 2E^{(3)}_{sig}(\omega) E_{LO}(\omega) \cos(\omega t_{LO} + \phi), \tag{5.6}$$

where ϕ is the phase difference between $E^{(3)}_{sig}$ and E_{LO}, and we used the shift theorem of Fourier analysis to go from Eq. (5.4) to Eq. (5.5).[36] We note that if ϕ is nonzero, it can be set to zero through a phasing procedure in post-processing of the data [43]. The order of operations, a Fourier transform followed by taking the absolute square, reflects the experimental detection process, and I_{LO} and I_{sig} are the intensity of the LO and the signal pulses, respectively. The I_{sig} contribution is weak enough that it does not contribute to the measured signal, and I_{LO} produces a constant signal that can be removed experimentally in a variety of ways. Lock-in detection can remove this contribution, as can filtering in

the conjugate Fourier domain (the time domain) of the signal, t_ω. In this domain, we can think of I_{LO} as interference between E_{LO} with itself, and this homodyne process appears at time $t_\omega = 0$. The measured interference between $E_{LO}(\omega)$ and $E^{(3)}_{sig}(\omega)$ is modulated by the difference in arrival time between the LO and the signal, and appears at time $t_\omega = t_{LO}$. As such, this interference pattern provides a direct measurement of the time between the LO and the signal. In addition, as long as t_{LO} is greater than zero, we can isolate the final term in Eq. (5.6) that contains the information about the third-order molecular response of the sample [44].

In an optical resonance imaging measurement, interferometric heterodyne detection allows us to discriminate between arrival times of signals from different parts of the sample. Repeating the same mathematical analysis above for a signal with PFT we have

$$S(\omega) = \left| \int_{-\infty}^{\infty} dt \; (E_{LO}(t - t_{LO}) + E^{(3)}_{sig}(t - px))e^{i\omega t} \right|^2, \tag{5.7}$$

$$S(\omega) = I_{LO} + I_{sig} + 2E^{(3)}_{sig}(\omega)E_{LO}(\omega)\cos(\omega(t_{LO} + px)), \tag{5.8}$$

where we assume $\phi = 0$.

The value $E_{LO}(\omega)$ is simply the amplitude at a given frequency, and it can be found from the measurement of I_{LO}, since $I_{LO} = |E_{LO}(\omega)|^2$. Using this information in combination with the simplification of $S(\omega)$ discussed above, we can write the signal that contains our spatial information as

$$S(\omega) = 2E^{(3)}_{sig}(\omega)\cos(\omega(t_{LO} + px)) = 2E^{(3)}_{sig}(\omega)\cos(\omega px), \tag{5.9}$$

where in the last step we set $t_{LO} = 0$. In an ORI measurement, t_{LO} represents the difference in arrival time between the LO pulse and the start of the tilted signal pulse as shown in Fig. 5.2. Since t_{LO} can be thought of as a constant phase, we set it equal to zero.

Generating the final image can be accomplished with a final Fourier transform of Eqn.

(5.9) back to the time domain

$$S_{image}(t) = \int_{-\infty}^{\infty} d\omega \, 2E_{sig}^{(3)}(\omega)\cos(\omega px)e^{i\omega t} = \int_{-\infty}^{\infty} d\omega \, E_{sig}^{(3)}(\omega)(e^{i\omega px} + e^{-i\omega px})e^{i\omega t}, \quad (5.10)$$

$$S_{image}(t) = E_{sig}^{(3)}(t + px) + E_{sig}^{(3)}(t - px), \quad (5.11)$$

$$S_{image}(t)_{-} = E_{sig}^{(3)}(t - px), \quad (5.12)$$

where $S_{image}(t)_{-}$ corresponds to one side of the time axis generated by the Fourier transform. We can ignore the other side of the axis since it contains identical information because the signal field is a real valued function. Thus, the spatial information encoded into our signal can be extracted from the measured experimental data. We note that since the bandwidth of the transition that generates $E_{sig}^{(3)}$ is not infinite, it will provide a fundamental limit on the resolution of the instrument.

To assess the feasibility of this approach, we simulated the electric field emitted by a finite number of point emitters. We divided our sample into 5 nm blocks. Each block represented a dipole (e.g. a collection of molecules or atoms) that interacted with pulses 1 and 2, placing the system in an excited state from which pulse 3 stimulated emission. The size of the illuminated area was determined by W_f from Fig. 5.2, as we can set the spot size of beams 1 & 2 to be larger than W_f. The magnitude of a photon echo signal $E_{sig}^{(3)}$ scales as

$$E_{sig}^{(3)} \propto |E_1||E_2||E_3|, \quad (5.13)$$

so if $|E_1|$ and $|E_2|$ are roughly constant, then the Gaussian width across W_f scaled the magnitude of the stimulated emission generated by pulse 3.

The emitting polarization in the sample was approximated as a dipole source because the size of a single emitting block is much smaller than the wavelength of light. We simulated a dipole field with a carrier-wave wavelength of 800 nm, and a Gaussian temporal envelope that has a FWHM of 15 fs in the paraxial approximation, where a spherical wave is represented

by a complex quadratic phase. A 15 fs pulse duration is equivalent to a transition with 60 nm of bandwidth centered at 800 nm. We calculated the electric field in the spatial dimension with PFT, perpendicular to the optical axis as a function of time. To simulate what the signal will look like at the detector, we propagate the emitted dipole field through an $f/2$ optical imaging system using Fourier optics to simulate focusing the signal into our spectrometer and then perform the operations outlined mathematically above that simulate interferometric heterodyne detection with a 15 fs FWHM LO pulse.

The results of this simulation, shown in Fig. 5.3, were calculated for a pair of emitters spaced by 275 nm. This separation satisfies the Rayleigh criterion for identifying distinct point sources. The image produced by the ORI simulation is plotted as the red trace in Fig. 5.3. The black lines plotted in the figure correspond to where the expected peak centers are based on the simulation settings. Fig. 5.3 also shows the diffraction-limited image generated in these calculations.

The result in Fig. 5.3 demonstrates that ORI can resolve structures below the diffraction limit of the optics used in the experiment. As clearly seen in Fig. 5.3 for $f/2$, diffraction-limited imaging only yields one feature, while ORI can resolve two features using these optics. spaced below the diffraction limit of $f/0.5$ optics. The limits placed on spatial resolution then become dependent upon the separation *in time* of the emitted signal from different parts of the sample under study. In any real optical system, the physical optics cannot collect all possible steradians of emitted signal. However, in ORI, if the signals are measurably separated in time, this will determine the resolution and not the numerical aperture of the collection optics. As such, for the simulation of the signal shown in Fig. 5.3, we can calculate a smaller number of solid angles, and because of the spacing of the emitted spherical waves in time, accurately measure the spacing of the two point emitters below the diffraction limit.

Optical resonance imaging can overcome the diffraction limit of the optics used and offers the potential for superresolution imaging. It is possible to write a general equation

that specifies the resolution of an image generated with ORI. Starting with the definition of PFT from Eqn. 5.1 we have

$$pc = \tan\gamma = \frac{c \cdot T_f}{W_f}, \tag{5.14}$$

$$p = \frac{T_f}{W_f}, \tag{5.15}$$

where c is the speed of light, and T_f and W_f are defined in Fig. 5.2. To generate an image, the instrument must be able to distinguish between different points emitted by the sample as a function of time. The maximum possible number of independent time points that can be measured across the emitted signal, N, can be written as

$$N = \frac{T_f}{\tau_s} \tag{5.16}$$

where τ_s is the FWHM of the signal. This is true as long as the pulse duration of the LO pulse is as short or shorter than the temporal duration of the emitted signal. Since different portions of the sample emit at different times, the lateral spatial resolution (l_r) of the experiment can then be thought of as the number of independent points measured across the focused spot size

$$l_r = \frac{W_f}{N} = \frac{W_f \tau_s}{T_f}. \tag{5.17}$$

We can then make use of Eqn. 5.15 to find that

$$l_r = \frac{\tau_s}{p}. \tag{5.18}$$

The result in eqaution 5.18 shows that the resolution in an ORI experiment only depends upon the pulse front tilt applied and the temporal duration of the sample response (put

equivalently, the emission bandwidth of the sample). As such the resolution of an ORI image will improve with larger PFT and faster sample response. For the results discussed in this work, using f/0.5 optics to generate angle of γ equal to 87 degrees produces a PFT of 0.0636 fs·nm^{-1}. For a value of $\tau_s = 15$ fs, we find a resolution of 240 nm, independent of the wavelength of the light.

The value of p in Eqn. 5.18 is the PFT of the emitted signal. We have derived this result assuming that the PFT of pulse 3 is equal to the PFT of the emitted signal. The above result is quite general, implying that the PFT of the signal is independent of the method in which PFT is delivered to the sample. This presents opportunities to significantly improve the resolution if novel ways can be found to generate significant PFT of the emitted signal.

5.4 Conclusion

Excitons generated by the absorption of photons are routinely studied with nonlinear spectroscopy, however they cannot be imaged directly because techniques do not yet exist that have the requisite spatio-temporal resolution. Excitation imaging with ultrafast temporal resolution will offer new insights into the process of energy transfer and provide a tool to design and control how energy moves through materials.

Most experiments that can measure dynamics on femtosecond-to-nanosecond timescales remain diffraction-limited [16, 45]. Some recent work has demonstrated superresolution pump-probe microscopy; however, it is still limited to raster scanning a beam across the sample to generate an image [46]. In comparison, ORI generates a widefield image since different parts of the sample emit at different times and contribute to different parts of the image. Resolution is thus decoupled from wavelength and is determined by the bandwidth of the emitter and pulsefront tilt emitted by the sample.

A single ORI experiment to extract spatial information from the sample can be performed for a fixed time intervals, τ, T, and t_R. In this fashion, each acquisition will have temporal

resolution on the order of the pulse-front tilt (ps), while a series of images will provide temporal resolution limited by the length of the untilted pulse (15 fs) or the molecular response function, whichever is longer. Changing the waiting time changes the population evolution, analogously to pump-probe spectroscopy (or microscopy). Instead of looking at spectral changes, ORI will image the changes in the sample. An opto-mechanical delay line can be used to control T out to the nanosecond regime.

Another exciting possibility results from the opportunity spectroscopic resolve the input and output energy. ORI is a third-order nonlinear experiment, therefore, the timing between all three pulses can be experimentally controlled and so a complete measurement of the ORI response function $R^{(3)}(\tau, T, t_R)$ will also contain spectral information. The ability to vary the time between pulses 1 and 2 is a degree of freedom unavailable in pump-probe microscopy, and Fourier transforming along this coordinate would provide spectral information along the "pump" axis in the same way as two-dimensional electronic spectroscopy. In addition, the heterodyne-detected data in the frequency domain provide the spectral information contained in the signal. Assignment of different spectral features is possible from two-dimensional electronic spectroscopy, and when combined with this extra experimental handle, optical resonance imaging thus correlates the input energy with the final position and energy of the exciton.

5.5 Methods to Generate Simulations

Kostenbauder Simulation of Pulse 3: The Kostenbauder matrix as defined in Eq. (5.3) can be used to calculate how how a variety of different optical elements affect the propagation of a Gaussian beam. Mirrors and distance propagators are defined in the same way as ABCD matrices with terms E, F, G, H, and I (as defined in Eq. (5.3)) equal to zero, since mirrors

and lenses do not generate spatio-temporal couplings. A diffraction grating is represented as

$$g = \begin{pmatrix} -\frac{sin\phi}{sin\psi} & 0 & 0 & 0 \\ 0 & -\frac{sin\psi}{sin\phi} & 0 & \lambda\frac{cos\phi - cos\psi}{c\, sin\phi} \\ \frac{cos\psi - cos\phi}{c\, sin\phi} & 0 & 1 & 0 \\ 0 & 0 & 0 & 1 \end{pmatrix}, \tag{5.19}$$

where ψ and ϕ are the input and output angles defined relative to the grating surface in the same way as in reference [38]. The simulated optical system consists of a focusing lens, a grating, and then a pair of lenses to image the grating onto the sample. The electric field of a Gaussian beam can be described in terms of Q-matrices [35] such that

$$E(x,t) = exp\Big[-i\frac{\pi}{\lambda_0} \begin{pmatrix} x \\ -t \end{pmatrix}^T Q^{-1} \begin{pmatrix} x \\ t \end{pmatrix} \Big]. \tag{5.20}$$

The initial Q-matrix, Q_{in} is given by

$$Q_{in} = i\frac{\lambda_0}{\pi} \begin{pmatrix} \widetilde{Q}_{xx} & \widetilde{Q}_{xt} \\ \widetilde{Q}_{tx} & \widetilde{Q}_{tt} \end{pmatrix}^{-1}, \tag{5.21}$$

where

$$\widetilde{Q}_{xx} = -i\frac{\pi}{\lambda_0 R(z)} - \frac{1}{w(z)^2}, \tag{5.22}$$

$$\widetilde{Q}_{tt} = \frac{1}{\tau_i^2}, \tag{5.23}$$

and the off-diagonal terms are zero since the pulse begins with no spatio-temporal coupling. In the above equations, λ_0 is the center wavelength, R(z) is the radius of curvature, $w^2(z)$ is the beam radius, β is the spatial chirp, and τ_i is the temporal FWHM of the pulse and

we have no spatial chirp in the initial beam.

The Kostenbauder matrix representing the optical system can be found by taking the product of the optical elements

$$K = d_3 l_3 d_3 l_2 d_2 g d_1 l_1, \tag{5.24}$$

where l denotes a lens operator, d a distance propagation operator, and g the grating operator. Given Q_{in} and the matrix K, we can calculate

$$Q_{sample} = \left[\begin{pmatrix} A & 0 \\ G & 1 \end{pmatrix} Q_{in} + \begin{pmatrix} B & \frac{E}{\lambda_0} \\ H & \frac{I}{\lambda_0} \end{pmatrix} \right] \left[\begin{pmatrix} C & 0 \\ 0 & 0 \end{pmatrix} Q_{in} + \begin{pmatrix} D & \frac{F}{\lambda_0} \\ 0 & 1 \end{pmatrix} \right]^{-1}. \tag{5.25}$$

The value calculated for Q_{sample} can be fed into Eqn. 5.20 to calculate the electric field at the sample. The data plotted in Fig. 5.2 are the intensity of the electric field, $|E(x,t)|^2$. The specific choices of values for for the simulation plotted in Fig. 5.2 can be found in Table 5.1. These calculations were carried out using Wolfram Mathematica 10.2.

Simulation of Emitted Signal: All calculations of the emitted signal were performed using MATLAB R2015a. The emitted third-order signal, $E_{sig}^{(3)}$, was modeled as a spherical wave that results from a single dipole emitter. We choose to make the approximation necessary for the use of Fourier optics, where a spherical wave can be represented by a quadratic phase term that approximates the spherical wavefronts as parabolic.[47] In addition, since we only have pulse-front tilt in one spatial dimension, x, we choose to calculate the electric field in the x-dimension perpendicular to the direction of propagation, which is defined as z. The signal has a carrier frequency of 375 THz (center wavelength of 800 nm) and a Gaussian temporal envelope with a FWHM of 15 fs. As such, the signal from a given dipole and can

Table 5.1: List of Simulation Values

Kostenbauder		Signal	
Parameter	Value	Parameter	Value
g_{sp}	500 nm[a]	τ_s	15 fs
θ_{in}	0.74 rad[b]	$W_{f,FWHM}$	814 nm
θ_{out}	1.18 rad[b]	z_{obs}	210 μm
ψ	$\pi/2$- 0.74 rad	optical aperture (collection)	$f/2$
ϕ	$\pi/2$ + 1.18 rad	spatial stepsize	5 nm
λ_0	800 nm	temporal stepsize	10 as
w(0)	5 mm	d	1 Debye
R(0)	10^8 mm		
τ_i	15 fs		
optical aperture	$f/0.5$		
d_1 = f of l_1	125 mm[c]		
d_2 = f of l_2	100 mm[c]		
d_3 = f of l_3	25 mm[c]		

a) spacing between lines on diffraction grating. b) θ_{in} and θ_{out} for diffraction grating defined relative to grating normal. c) f in this context denotes the focal length of the lens.

be written as

$$E^{(3)}_{sig}(x,z,t) = \left(\frac{d\cdot k^2}{4\pi\epsilon_0}\right) e^{i\frac{k(x-\eta)^2}{2z}} e^{-i\omega(t+t')} e^{-(\frac{z}{c}-(t+t'))^2/2(\frac{\tau_{mol}}{2.35482})^2} e^{-(x)^2/2(\frac{W_{f,FWHM}}{2.35482})^2}, \tag{5.26}$$

where d is the dipole moment and k is the wavevector, z is the position along the optical axis of the system, and t' is the time of dipole emission as determined by the pulse-front tilt. The origin of the x-axis is centered about the axis defined by z, and η corresponds to the distance of the dipole emitter from the optical axis. The last term accounts for the Gaussian nature of the spatial illumination of the sample by Pulse 3. Pulse-front tilt leads to emission of different parts of the sample at different times. The emission of the first dipole at a given point in the material starts at a given time, $t' = 0$, and we calculate its $E^{(3)}_{sig}$ as a function of x and t for a fixed value of $z = z_{obs}$. The next dipole to emit is delayed in time from the

first by

$$t' = \frac{x}{c} tan\gamma. \tag{5.27}$$

The time spacing between points in the simulation is 0.01 fs, and the spatial extent of x corresponds to the size of the aperture of $f/0.5$ optics illuminated by the Gaussian beam plotted in Fig. 5.2.

To simulate imaging this field into a spectrometer, we model an optical system with $f/2$ optics, which consists of 2 lenses of focal length f, spaced by 2f. Equation 5.26 is used to calculate the electric field directly behind the first lens of the imaging system and we calculate the field at the front focal plane of the second lens, where the image forms using Fourier optics in the Fresnel approximation.[47] The image forms on the input slit of a spectrometer that will be used to measure the emitted interferogram of $E^{(3)}_{sig}(x, z, t)$ with E_{LO}. Taking $E^{(3)}_{sig}(x, z, t)$ as the input field of the Fourier optics, U_{in}, we can write an operator, $\hat{S}$, to model the optical system and calculate U_{out}, the output field, as

$$U_{out} = \hat{S}\, U_{in} = F^{-1}Q[-\lambda^2 f]FQ\left[\frac{-1}{f}\right]F^{-1}Q[-\lambda^2 2f]FQ\left[\frac{-1}{f}\right]U_{in}, \tag{5.28}$$

where F and Q are a spatial Fourier transform, and quadratic phase operator as defined by Goodman, respectively [47], and the values in brackets are the input arguments for the operator. All Fourier transforms are calculated numerically using the fast-Fourier transform (FFT) algorithm in Matlab. To simulate the effect of the spectrometer we perform an FFT along the temporal dimension of U_{out} and then sum down the spatial dimension since the imaging system is diffraction limited, there is no additional spatial information along this axis. Equivalently, we could have used just one line from the calculated array, representing a one-dimensional array of pixels on a detector. An LO signal is calculated using a carrier wavelength of 800 nm and τ = 15 fs FWHM and the FFT of the LO is multiplied by

the summed FFT of U_{out}. Measured electric fields are real valued, so we keep only the real part of the product defined in Eq.(5.9). Still in the frequency domain, we shift the position of the interferogram so that the peak is centered around zero frequency to remove any high-frequency contributions to the image. Finally we take the inverse FFT and plot the magnitude of the complex signal as the image in Fig. 5.3.

5.6 Supporting Information for ORI

5.6.1 The ORI Third-Order Response Function

The macroscopic polarization, $P(t)$, generated by an incident electric field connects a measured optical signal to the microscopic response of the molecules or materials. In the dipole approximation, this polarization can be expressed as

$$P(t) = Tr(\hat{\mu}\rho(t)) =< \hat{\mu}\rho(t) > \tag{5.29}$$

where $\hat{\mu}$ is the dipole operator, $\rho(t)$ is the time-dependent density matrix, and the angle brackets denote a trace. In the perturbative regime where the electric field of light only weakly couples to the material system, it is possible to perturbatively expand the density matrix. For a third-order nonlinear experiment, involving three interactions of an electric field with a sample at disinct times denoted as t_1, t_2, and t_3, in the interaction picture, we can write the trace above as the following convolution integral

$$P^{(3)}(t) = \int_{-\infty}^{t} dt_3 \int_{-\infty}^{t_3} dt_2 \int_{-\infty}^{t_2} dt_1 E(t_1)E(t_2)E(t_3) \cdot R^{(3)}(t_1, t_2, t_3) \tag{5.30}$$

where E denotes an electric field interaction and $R^{(3)}(t_1, t_2, t_3)$ is a third-order response function that can be written

$$R^{(3)}(t_1, t_2, t_3) = \left(\frac{-i}{\hbar}\right)^3 \theta(t_1)\theta(t_2)\theta(t_3)\langle\mu(t) \cdot [\mu(t_3), [\mu(t_2), [\mu(t_1), \rho(-\infty)]]]\rangle, \tag{5.31}$$

where $\theta(t)$ is the Hevaside step function.

The time variables discussed above are defined for absolute times, but it is more useful experimentally to discuss time intervals corresponding to the time differences between a pair of pulses. As such we make the following definitions:

$$t_1 = 0 \tag{5.32}$$

$$\tau = t_2 - t_1 \tag{5.33}$$

$$T = t_3 - t_2 \tag{5.34}$$

$$t_R = t - t_3 \tag{5.35}$$

where τ is the time between pulses 1 and 2, T is the time between pulses 2 and 3, and t_R is the time between pulse 3 and the signal tine t. This allows us to redefine the response function as $R^3(\tau, T, t_R)$.

In a canonical third-order nonlinear spectroscopic measurement, such as 2DES or 2DIR, where none of the pulses have pulse-front tilt, the third-order polarization generated in the sample, and thus the emitted third-order signal, is a function of three temporal intervals defined above. These three variables are controlled experimentally by moving an opto-mechanical delay line to delay one pulse's arrival relative to the other. Performing different measurements with different values of τ and then Fourier transforming over this coordinate produces a frequency axis that is equivalent to spectrally resolving the pump frequency (or excitation frequency, ω_t). The second time variable, T, corresponds to the time difference

between pulses 2 and 3. During this time, the measured system is generally thought to be in a population state, meaning the system evolves in time as an eigenstate of the unperturbed Hamiltonian. Again, this time is controllable by varying the arrival time of pulse 3 relative to pulse 2 using an opto-mechanical delay line. The final time domain, t_R, is dfined as the time after the third pulse, when the signal is emitted. This time domain is typically measured interferometrically by using a spectrometer to convert from time to frequency and mixing the signal with the local oscillator, producing the second frequency axis, or probe frequency, ω_{t_R}, presented in a typical 2D plot.

A nonseperable spatio-temporal coupling, such as pulse-front tilt, of pulse 3 means that arrival time of this pulse, ie. time variable t_3, will vary across the sample as a function of position, allowing us to write the spatially-dependent temporal interval between pulses two and three as

$$t_3 - t_2 = T - px, \tag{5.36}$$

where p denotes pulse-front tilt and x is a spatial coordinate. As such teh spatial-temporal coupling is present in the response function, which can be written as $R^3(\tau, T - px, t_R)$. Thus, all the time intervals, including T, remain experimentally controllable variables. This should enable the extraction of both two-dimensional spectra as well as optical resonant images from the same experimental setup, as long as all the time intervals are experimentally scanned.

5.6.2 Kostenbauder Matrix Calculations

The Kostenbauder formalism discussed in the main text allows us to follow the spatio-temporal coupling of pulse 3. The following figure confirms that the pulse still has a 15 fs FWHM.

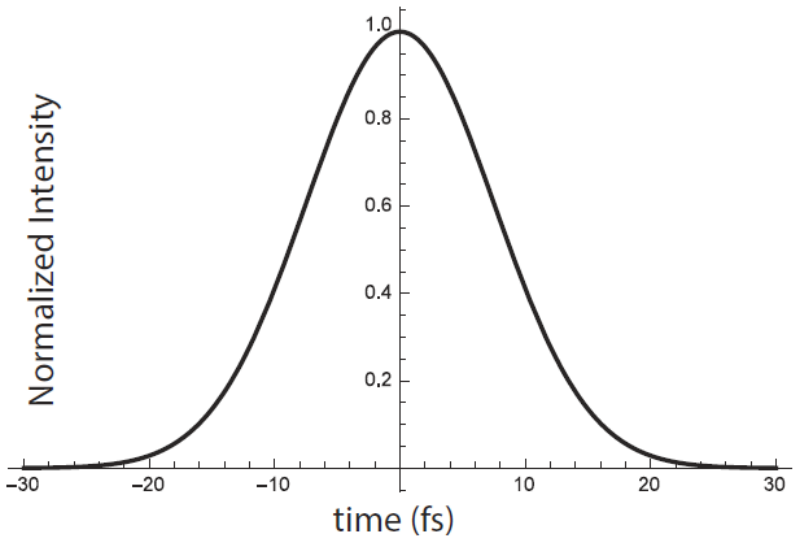

Figure 5.4: A slice through the point x = 0 from Fig 5.2

5.6.3 Fourier Optics Simulation

The simulated ORI signal was calculated by propagating the emitted dipole fields through a f/2 optiacl system. Fig.5 shows the field as calculated before the first lens. The lens applies a quadratic phase which cancels the phase from the emitted signal wave since the source was at the focus. The wave was then propagated to just before the second lens. The calculated collimated field can be seen in Fig. 6. Finally the field was propagated to the focus of the second lens, which in this model corresponds with the entrance slit of the simulated spectrometer. This simulated signal can be seen in Fig. 7.

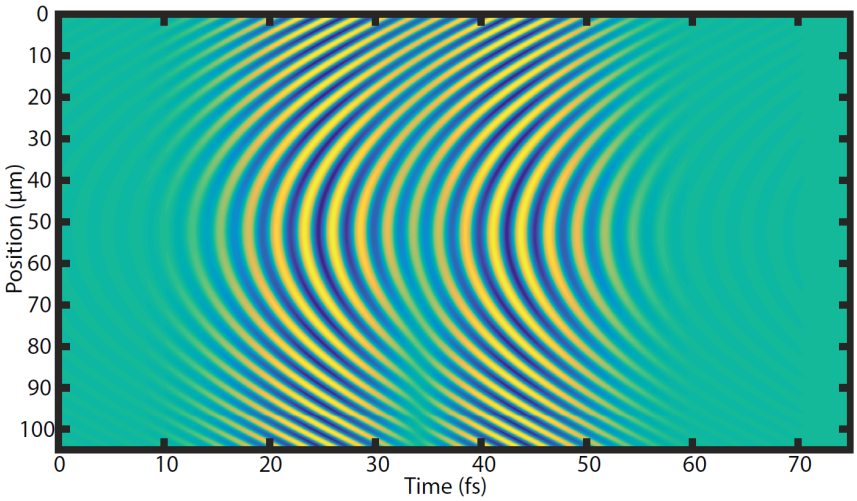

Figure 5.5: The real-valued electric field before the first lens of the collection optics.

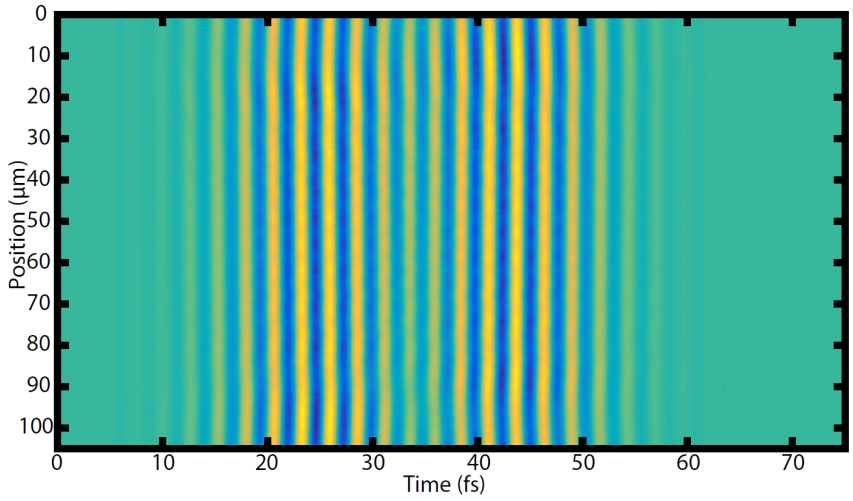

Figure 5.6: The real-valued electric field before the second lens of the collection optics.

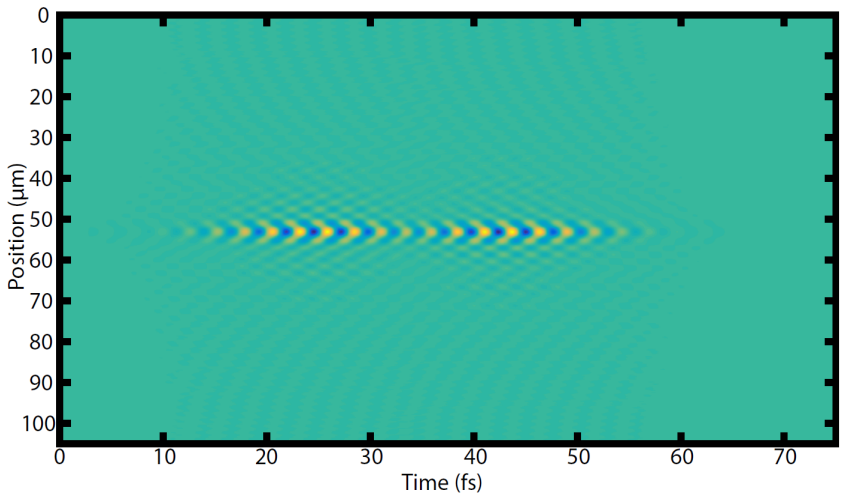

Figure 5.7: The real-valued electric field at the entrance slit of the simulated spectrometer.

REFERENCES

[1] Marco A. Allodi, Peter D. Dahlberg, Richard J. Mazuski, Hunter C. Davis, John P. Otto, and Gregory S. Engel. Optical resonance imaging: An optical analog to mri with subdiffraction-limited capabilities. *ACS Photonics*, 3(12):2445–2452, 2016.

[2] E. Abbe. Beitraege zur theorie des mikroskops und der mikroskopischen wahrnehmung. *Archiv fuer mikroskopische Anatomie*, 9(1):413–418, 1873.

[3] L. Rayleigh. Xxxi. investigations in optics, with special reference to the spectroscope. *Philosophical Magazine Series 5*, 8(49):261–274, 1879.

[4] E. A. Ash and G. Nicholls. Super-resolution Aperture Scanning Microscope. *Nature*, 237:510–512, June 1972.

[5] U. Ch. Fischer and D. W. Pohl. Observation of single-particle plasmons by near-field optical microscopy. *Phys. Rev. Lett.*, 62:458–461, 1989.

[6] Eric Betzig and Jay K. Trautman. Near-field optics: Microscopy, spectroscopy, and surface modification beyond the diffraction limit. *Science*, 257(5067):189–195, 1992.

[7] Eric Betzig, George H. Patterson, Rachid Sougrat, O. Wolf Lindwasser, Scott Olenych, Juan S. Bonifacino, Michael W. Davidson, Jennifer Lippincott-Schwartz, and Harald F. Hess. Imaging intracellular fluorescent proteins at nanometer resolution. *Science*, 313(5793):1642–1645, 2006.

[8] Thomas A. Klar, Stefan Jakobs, Marcus Dyba, Alexander Egner, and Stefan W. Hell. Fluorescence microscopy with diffraction resolution barrier broken by stimulated emission. *Proc. Nat. Acad. Sci. USA*, 97(15):8206–8210, 2000.

[9] Michael J Rust, Mark Bates, and Xiaowei Zhuang. Sub-diffraction-limit imaging by

stochastic optical reconstruction microscopy (storm). *Nat. Methods*, 3(10):793–796, 2006.

[10] Brent Bailey, Daniel L Farkas, D Lansing Taylor, and Frederick Lanni. Enhancement of axial resolution in fluorescence microscopy by standing-wave excitation. *Nature*, 366:44–48, 1993.

[11] Mats G. L. Gustafsson. Nonlinear structured-illumination microscopy: Wide-field fluorescence imaging with theoretically unlimited resolution. *Proc. Nat. Acad. Sci. USA*, 102(37):13081–13086, 2005.

[12] Dong Li, Lin Shao, Bi-Chang Chen, Xi Zhang, Mingshu Zhang, Brian Moses, Daniel E. Milkie, Jordan R. Beach, John A. Hammer, Mithun Pasham, Tomas Kirchhausen, Michelle A. Baird, Michael W. Davidson, Pingyong Xu, and Eric Betzig. Extended-resolution structured illumination imaging of endocytic and cytoskeletal dynamics. *Science*, 349(6251), 2015.

[13] R. E. Blankenship. *Molecular Mechanisms of Photosynthesis*. Blackwell Science, 2002.

[14] G. S. Engel, T. R. Calhoun, E. L. Read, Tae-Kyu Ahn, T. Cancal, Y Cheng, R. E. Blankenship, and G. R. Fleming. *Nature*, 446:782–786, 2007.

[15] Elisabetta Collini, Cathy Y Wong, Krystyna E Wilk, Paul MG Curmi, Paul Brumer, and Gregory D Scholes. Coherently wired light-harvesting in photosynthetic marine algae at ambient temperature. *Nature*, 463(7281):644–647, 2010.

[16] Yan Wan, Zhi Guo, Tong Zhu, Suxia Yan, Justin Johnson, and Libai Huang. Cooperative singlet and triplet exciton transport in tetracene crystals visualized by ultrafast microscopy. *Nature Chem.*, 7(10):785–792, 2015.

[17] Hoseok Heo, Ji Ho Sung, Soonyoung Cha, Bo-Gyu Jang, Joo-Youn Kim, Gangtae Jin, Donghun Lee, Ji-Hoon Ahn, Myoung-Jae Lee, Ji Hoon Shim, Hyunyoung Choi, and

Moon-Ho Jo. Interlayer orientation-dependent light absorption and emission in monolayer semiconductor stacks. *Nature comm.*, 6:7372, 2015.

[18] Xiaoping Hong, Jonghwan Kim, Su-Fei Shi, Yu Zhang, Chenhao Jin, Yinghui Sun, Sefaattin Tongay, Junqiao Wu, Yanfeng Zhang, and Feng Wang. Ultrafast charge transfer in atomically thin mos2/ws2 heterostructures. *Nature nanotechnol.*, 9(9):682–686, 2014.

[19] Dario Polli, Piero Altoe, Oliver Weingart, Katelyn M Spillane, Cristian Manzoni, Daniele Brida, Gaia Tomasello, Giorgio Orlandi, Philipp Kukura, Richard A Mathies, et al. Conical intersection dynamics of the primary photoisomerization event in vision. *Nature*, 467(7314):440–443, 2010.

[20] Philip JM Johnson, Alexei Halpin, Takefumi Morizumi, Valentyn I Prokhorenko, Oliver P Ernst, and RJ Dwayne Miller. Local vibrational coherences drive the primary photochemistry of vision. *Nature chemistry*, 7:980–986, 2015.

[21] Janne Savolainen, Saima Ahmed, and Peter Hamm. Two-dimensional raman-terahertz spectroscopy of water. *Proc. Nat. Acad. Sci. USA*, 110(51):20402–20407, 2013.

[22] Marco A. Allodi, Ian A. Finneran, and Geoffrey A. Blake. Nonlinear terahertz coherent excitation of vibrational modes of liquids. *J. Chem. Phys.*, 143(23):234204, 2015.

[23] Ian A. Finneran, Ralph Welsch, Marco A. Allodi, Thomas F. Miller, and Geoffrey A. Blake. Coherent two-dimensional terahertz-terahertz-raman spectroscopy. *Proc. Nat. Acad. Sci. USA*, 113(25):6857–6861, 2016.

[24] Stefan W. Hell and Jan Wichmann. Breaking the diffraction resolution limit by stimulated emission: stimulated-emission-depletion fluorescence microscopy. *Opt. Lett.*, 19(11):780–782, Jun 1994.

[25] Tobias Müller, Christian Schumann, and Annette Kraegeloh. Sted microscopy and its

applications: New insights into cellular processes on the nanoscale. *ChemPhysChem*, 13(8):1986–2000, 2012.

[26] P.C. Lauterbur. Image formation by induced local interactions: Examples employing nuclear magnetic resonance. *Nature*, 242:190–191, 1973.

[27] P. Callaghan. *Principles of Nuclear Magnetic Resonance Microscopy*. Oxford University Press, 1994.

[28] John D. Roberts. *ABCs of FT-NMR*. University Science Books, 1991.

[29] David A. Feinberg, Steen Moeller, Stephen M. Smith, Edward Auerbach, Sudhir Ramanna, Matt F. Glasser, Karla L. Miller, Kamil Ugurbil, and Essa Yacoub. Multiplexed echo planar imaging for sub-second whole brain fmri and fast diffusion imaging. *PLoS ONE*, 5:1–11, 12 2010.

[30] Minhaeng Cho and Graham R. Fleming. Photon echo measurements in liquids: Numerical calculations with model systems. *J. Chem. Phys.*, 98(4):2848–2859, 1993.

[31] P. Vöhringer, D.C. Arnett, T.-S. Yang, and N.F. Scherer. Time-gated photon echo spectroscopy in liquids. *Chem. Phys. Lett.*, 237(5):387 – 398, 1995.

[32] S. Mukamel. *Principles of Nonlinear Optical Spectroscopy*. Oxford University Press, 1995.

[33] P. Hamm and M. Zanni. *Concepts and Methods of 2D Infrared Spectroscopy*. Cambridge University Press, 2011.

[34] Selcuk Akturk, Xun Gu, Erik Zeek, and Rick Trebino. Pulse-front tilt caused by spatial and temporal chirp. *Opt. Express*, 12:4399–4410, Sep 2004.

[35] Selcuk Akturk, Xun Gu, Pablo Gabolde, and Rick Trebino. The general theory of first-order spatio-temporal distortions of gaussian pulses and beams. *Opt. Express*, 13:8642–8661, Oct 2005.

[36] Jyrki Kauppinen and Jari Partanen. *Fourier Transforms in Spectroscopy*. Wiley, 2001.

[37] Daniel Kreier and Peter Baum. Avoiding temporal distortions in tilted pulses. *Opt. Lett.*, 37(12):2373–2375, Jun 2012.

[38] A.G. Kostenbauder. Ray-pulse matrices: a rational treatment for dispersive optical systems. *IEEE J. Quant. Electron.*, 26(6):1148–1157, Jun 1990.

[39] Anthony Gerrard and James M. Burch. *Introduction to Matrix Methods in Optics*. Dover, 1975.

[40] Max Born and Emil Wolf. *Principles of Optics, 7th ed.* Cambridge, 1999.

[41] Allison W. Albrecht, John D. Hybl, Sarah M. Gallagher Faeder, and David M. Jonas. Experimental distinction between phase shifts and time delays: Implications for femtosecond spectroscopy and coherent control of chemical reactions. *J. Chem. Phys.*, 111(24):10934–10956, 1999.

[42] Christophe Dorrer. Influence of the calibration of the detector on spectral interferometry. *J. Opt. Soc. Am. B*, 16(7):1160–1168, Jul 1999.

[43] V. P. Singh, A. F. Fidler, B. S. Rolczynski, and G. S. Engel. Independent phasing of rephasing and non-rephasing 2d electronic spectra. *J. Chem. Phys.*, 139(8):084201, 2013.

[44] Peter D. Dahlberg, Andrew F. Fidler, Justin R. Caram, Phillip D. Long, and Gregory S. Engel. Energy transfer observed in live cells using two-dimensional electronic spectroscopy. *J. Phys. Chem. Lett.*, 4(21):3636–3640, 2013.

[45] Erik M. Grumstrup, Michelle M. Gabriel, Emma E.M. Cating, Erika M. Van Goethem, and John M. Papanikolas. Pump-probe microscopy: Visualization and spectroscopy of ultrafast dynamics at the nanoscale. *Chem. Phys.*, 458:30 – 40, 2015.

[46] Eric S. Massaro, Andrew H. Hill, and Erik M. Grumstrup. Super-resolution structured pump-probe microscopy. *ACS Photonics*, 3(4):501–506, 2016.

[47] J. W. Goodman. *Introduction to Fourier Optics, 3rd Edition.* W.H. Freeman & Co., 2004.

CHAPTER 6

FUTURE DIRECTIONS

6.1 Overview

What is the link between the different areas of my research? I would hazard that in all aspects I was looking for novel *mesoscale* dynamics of materials. One way to do this was seen in Chapter 4, where a series of structures were constructed where just a few variables were changed from structure to structure, giving a library of structure. This library was then studied using fluence-dependent pump-probe spectroscopy to extract design principles of the system, such as the relationship between the dimer trap-state and increased fluence. ORI, which was discussed in Chapter 5, takes an opposite approach. Instead of tuning the synthetic system in such fine detail that design principles can be found through process of eliminations (as seen by the series of control structures in Chapter 4), real materials and their ultrafast dynamics can be studied under a microscope. The experimental realization of ORI is still a work in progress, but significant thought has gone into how to realize it, and I hope to outline steps on how to achieve the first ORI image.

6.2 Realizing the First Optical Resonance Image

Figure 6.1 shows the first design used to experimentally test ORI. It has a number of issues which future versions of ORI should seek to improve upon. The first is using translation stages with mounted mirrors as retroreflectors. This compromises stability and repeatability in an area that isn't even novel to ORI. Mechanized delay lines should be used, and high quality retroreflectors or wedge pairs should be used to best control timings. Secondly, focusing Beam 3 onto a grating creates a large issue, as an ultrafast pulse when focused imparts a huge amount of energy and in our case, was burning the grating. Also, this

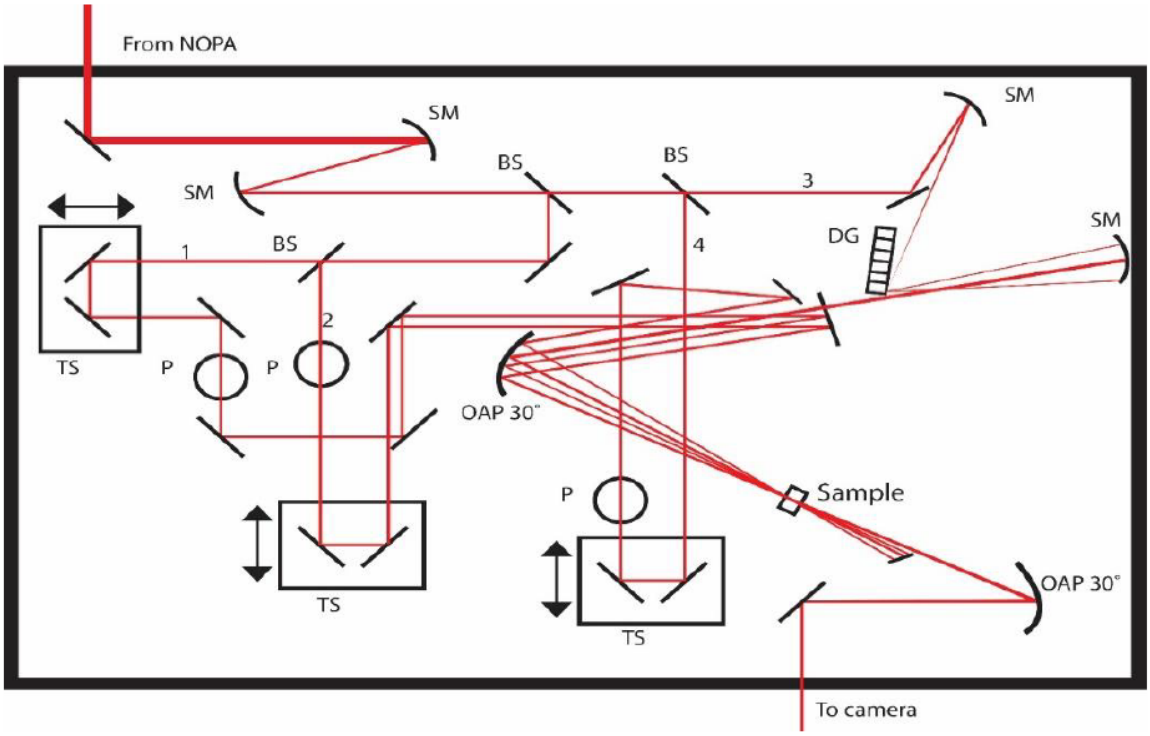

Figure 6.1: Light from a NOPA (or any other compressed source) would first be telescoped by two spherical mirrors (SM), before two beam splitters (BS) split off 1+2, 3, and 4. Beam 3 is focused onto a diffraction grating (DG), which imparts angular dispersion onto the beam. An SM catches the dispersing beam to collimate and send towards an OAP, where Beam 3 is spatially chirped. On the other side of the table, Beams 1 and 2 are separated and both go through translation stages (TS) to encode time delays τ and T. Every beam is sent to an off axis parabolic (OAP), which focuses the beams onto the sample. Most beams are blocked, with the exception of Beam 4, the local oscillator, which is collimated and sent to the camera along with the emitted signal.

amount of dispersion generated by coming from such a steep angle will not be corrected by simply collimation.

A more sophisticated approach would be to create half of a stretcher which would balance second-order dispersion with pulse front tilt generation. Finally, more thought needs to be given to the phase-matching direction, since although a tilted pulse front still travels with the same wave-vector as a beam without a tilted pulse front, the instantaneous phase has a delay from the top to the bottom of the beam (pulse front tilt is after all defined by an

angle between phase front and wave front). Even if signal could be acquired, there was no certainty that we were able to capture it in the camera. There is plentiful literature available on the generation of PFT, and I would say generating high quality, non-distorted PFT would be the first step for the next foray into ORI.[1, 2, 3]

Finally, for samples to look at, I would recommend constructing something for a test and calibration sample. Something similar to the 1951 US Air Force resolution test chart would test the resolution and field of view of ORI. An optically transparent background would be necessary, as well as very bright emitters. The first non-test sample could be thin films of organic semiconductors. In these, heterogenous environments are known to affect exciton diffusion, and path lengths are known to be well into the micron range, which will be within ORI's spatial resolution limits.

6.3 Future Directions of Synthetic Light Harvesting and Ultrafast Spectroscopy

In Chapter 3 I discussed preliminary results for studying the four-arm star. It seems that fluence-dependent 2DES does have a role to play in discerning the dynamics of synthetic FRET based systems, especially when dyes are pushed together towards an intermediate coupling regime. The future for that particular project necessitates accurate phase correction, which was unfortunately only possible for long time data. Phasing this particular sample is important because it would distinguish a double-excitation feature from energy transfer below the diagonal. Beyond this, we have seen in Cy5 homodimer samples that oscillations around 600 cm^{-}1 persist throughout the structure and could possibly provide a vibronic method of ultrafast energy transfer. Beating map analysis of the short time data of the four-arm star remains inconclusive, but it would be possible for it to lead to a deeper understanding of the underlying photophysics.

Figure **??** shows a preliminary beat map from absolute value 2DES data. We see here

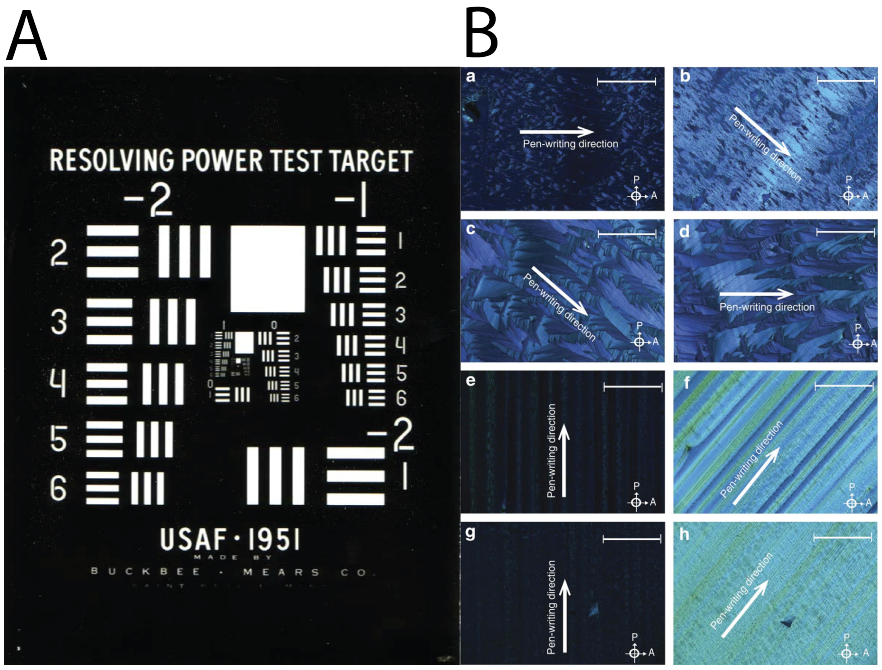

Figure 6.2: (A) The 1951 USAF resolution test chart used to validate imaging systems. ORI could make use of a similar test sample, constructed on very thin glass. Image from Wikipedia [4] and used under Creative Commons Attribution-Share Alike 2.5 Generic license (B) Long range ordering and transport in phthalocyanine films as revield by polarized microscopy. Various solvents and conditions are used. Scale bar is 500 μm. Used from Pan et al. [5] with permission under Creative Commons Attribution 4.0 International License.

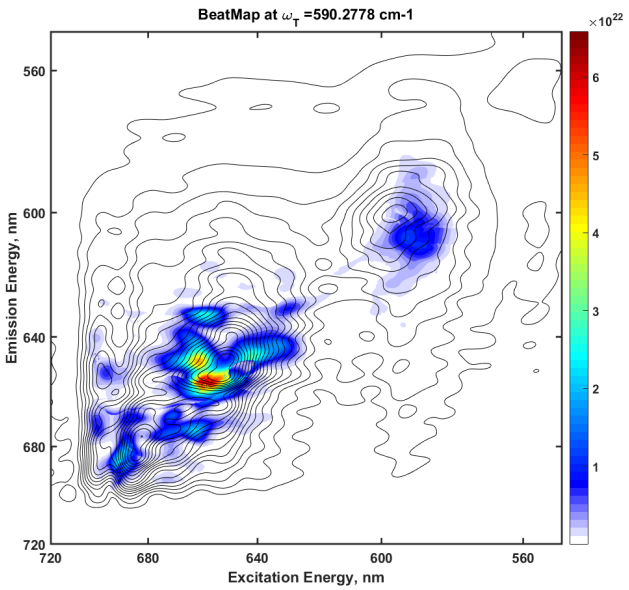

Figure 6.3: Beating at 590 cm^{-1} shows persistent beating along all dyes.

some beating at 590 cm^{-1} which shows persistent beating from the Cy5.5 nexus all the way out to Cy3.5. Our laser pulse's coverage of the Cy3 dye was potentially inadequate to fully see beating to the same extent that we were able to in the lower three dyes, however, closer inspection at the Cy3 feature in 2D gives a beating plot which shows a similar spike of intensity above the noise at a little less than 600 cm^{-1}. The vibronic coupling model developed by Sohail et al. (publication forthcoming) could possibly be applied to the system. The reminder here is that in the end, novel photophysics seem to always crop up as either unexplained spikes in performance, or in failures of experiments to meet theoretical expectations. The four-arm star underperforms theoretical models, so the underlying explanation could be found with careful study.

Finally, two-color pump-probe spectroscopy could be used to probe the end-to-end ultrafast dynamics of the four-arm star. Potentially exciting the sample at 480 nm, a two-color pump-probe experiment could track the initial energy transfer events while also quantifying the exact amount of energy transfer. I would note that the Cy5.5 absorption at 480 nm (or

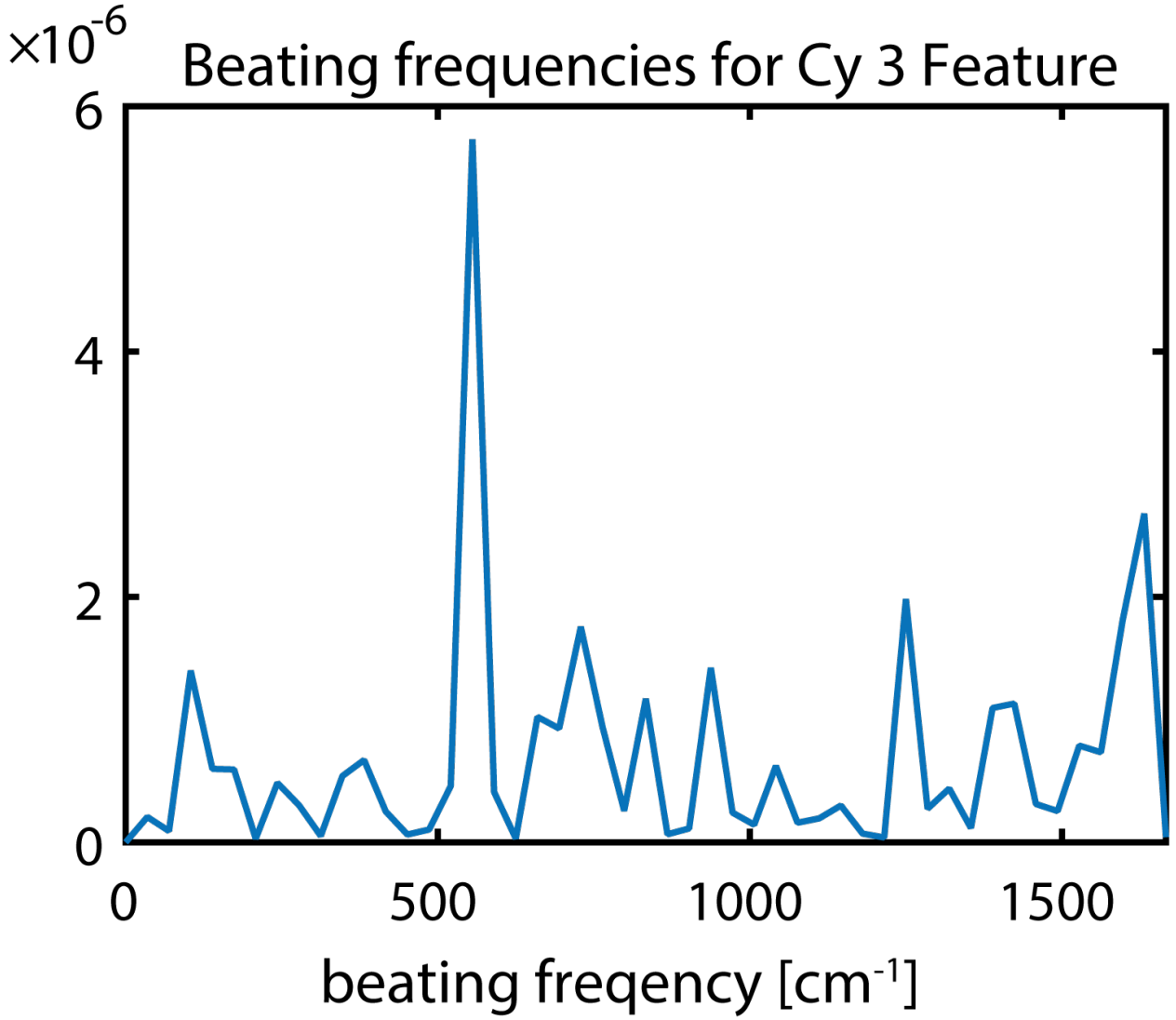

Figure 6.4: Beating at the Cy3 site shows a similar spike in intensity at just lower than 600 cm^{-1}.

466 nm, as was the case in the fluorescence experiments by Klein et al. [6]) is non-zero, so in fluorescence it is possible that initial excitation at 480 nm is captured by Cy5.5 (or Cy3, Cy3.5, and Cy5) and thus is the source of the red fluorescence. Careful experimentation with two-color pump-probe could prove fruitful to quantify the actual energy transfer events which occur within the four-arm star.

Within simpler MPWs, one experiment almost begging to be done is a temperature-dependent study of the glass transition responsible for the deactivation of the nonradiative trap in our dimer MPW. This experiment would be done in a 3:1 glycerol-to-buffer solution. At room temperature, fluence-dependence was preserved and lower excitation density resulted in a shorter excited state lifetime. At cryogenic temperatures, this fluence dependence was deactivated.[7] The experiment in question would require careful calibration of temperature to study the thermodynamics of this transition, using broadband pump-probe to mimic the spectrosocpy of the initial study. It would be possible to use simpler samples such as the control dimer to make the case more simple.

Finally, from a device design point of view, the use of coupled homoFRET dimers to trap excited energy transfer adds intriguing possibilities to logical DNA-based computing and excitonic engineering. One could see how on two divergint paths from a central core, one could use dimers to prevent FRET while the other could have single dyes. The former would become activated at low temperatures while the latter would remain open under all circumstances. The possibilities expand considerably when directional FRET is added to the equation, and dynamics of heterodimer dye-DNA samples are an active research area.

REFERENCES

[1] Daniel Kreier and Peter Baum. Avoiding temporal distortions in tilted pulses. *Opt. Lett.*, 37(12):2373–2375, Jun 2012.

[2] H. Esat Kondakci, Nicholas S. Nye, Demetrios N. Christodoulides, and Ayman F. Abouraddy. Tilted-pulse-front space-time wave packets. *ACS Photonics*, 6(2):475–481, 2019.

[3] J. A. Fülöp, L. Pálfalvi, G. Almási, and J. Hebling. Tilted-pulse-front pumping for phase matching and synchronization. In Solomon M. Saltiel, Alexander A. Dreischuh, and Ivan P. Christov, editors, *International Conference on Ultrafast and Nonlinear Optics 2009*, volume 7501, pages 101 – 108. International Society for Optics and Photonics, SPIE, 2009.

[4] Wikimedia Commons. File:1951usaf test target.jpg — wikimedia commons, the free media repository, 2015. [Online; accessed 18-May-2020].

[5] Z. Pan, N. Rawat, I. Cour, L. Manning, R. L. Headrick, and M. Furis. Polarization-resolved spectroscopy imaging of grain boundaries and optical excitations in crystalline organic thin films. *Nature Communications*, 6(1):8201, 2015.

[6] William P. Klein, Sebastián A. Díaz, Susan Buckhout-White, Joseph S. Melinger, Paul D. Cunningham, Ellen R. Goldman, Mario G. Ancona, Wan Kuang, and Igor L. Medintz. Utilizing homofret to extend dna-scaffolded photonic networks and increase light-harvesting capability. *Advanced Optical Materials*, 6(1):1700679, 2018.

[7] Richard J. Mazuski, Sebastián A. Díaz, Ryan E. Wood, Lawson T. Lloyd, William P. Klein, Divita Mathur, Joseph S. Melinger, Gregory S. Engel, and Igor L. Medintz. Ultrafast excitation transfer in cy5 dna photonic wires displays dye conjugation and excitation

energy dependency. *The Journal of Physical Chemistry Letters*, 0(0):4163–4172, 0. PMID: 32391695.

CHAPTER 7

CONCLUSION

One of the grand challenges of this century is *energy*. Conventional strategies are inefficient and costly from an environmental point of view, so using the limitless resource of the Sun meets both our desire for limitless expansion of energy-consuming behavior as well as being reasonably sustainable to the environment. The fundamental first step, and oftentimes a stumbling block for many emergent technologies, is light harvesting.

In the introduction, I listed some principles of light harvesting in photosynthesis that make it such a good model for improving synthetic light harvesting technologies. Three main motifs were discussed:

1. the use of spatial and energetic funneling,

2. robust response to multiple excitations,

3. and implementation of different degrees of coupling for energy transfer.

That section concluded with a brief review of synthetic light harvesing technologies, which will no doubt play an increased role in the future in both research and application.

The tools that are used to study light harvesting are ultrafast laser pulses because only with these optical tools can we see the femto- to picosecond dynamics off energy capture and manipulation. You can't engineer what you can't resolve. The study of ultrafast dynamics of complex materials is rooted in time dependent quantum mechanics and statistical mechanics. We use Feynman diagrams to explain the third-order response function and resolve the various pathways that contribute to a 2DES signal. Finally, I discussed the lab-work which makes our spectroscopy possible.

My preliminary results on the four-arm star show some promise when looking at the femtosecond dynamics. I would have initially thought picosecond dynamics of FRET transfer

much more important, but fluence changes have been proved irrelevant towards long time dynamics. In short time, we see certain interesting dynamic differences between low power and high power near the Cy5.5 core of the four-arm star. Taken in conjunction with Future Directions, I believe that the work here shows promise in determining the intricacies of energy transfer within the four-arm star.

My main project emerged somewhat by chance. Following the perceived negative results of the four-arm star, my group together with collaborators at the NRL sought to simplify the energy transfer scheme by testing distance and ligature. Crudely put, the dimer MPW was created as a way of jamming as many dyes in place as the DNA scaffold could handle. The results are novel, as the inverse fluence dependence is a rarely, if ever, reported phenomenon. Given this result, dynamics of homoFRET dyes on DNA seem as interesting and mysterious as ever. In music, it is said that there are still plenty of melodies to be written in C-Major (the simplest key in music, no sharps or flats), and an analogy to synthetic light harvesting would be, there are still plenty of MPWs to be constructed with Cy5s.

ORI has the potential to break wide open the study of excitons and provide a novel way of achieving high-efficiency light harvesting media. Mesoscale dynamics at interfaces are poorly understood due to the fact that many measurements either look at an ensemble, which would average over interfaces, or at the nanoscale, which isn't wide-field enough to see the full interaction of an excitation with an interface. The ultrafast portion of ORI would also allow for spatially-encoded 2DES, which could spectrally resolve ultrafast microscopy. For instance, seeing excitations from one origin could be separable from another origin.

In all, from the three main motifs of light harvesting in photosynthesis, a few conclusions can be reached from the various projects presented in this thesis. In terms of spatial and energetic funneling, we have seen that redundancies, which are ever-present in biology in the form of many light harvesting complexes per special pair, can be useful to increase effective energy transfer distance. The four-arm star accomplishes this by having each arm present

the same downwards FRET cascade towards a Cy5.5 arrival point. Increased redundancies, however, don't always lead to higher efficiency. In the MPWs, when we added dimer-like nodes to the wire, these effectively trapped energy flow.

Multiphoton effects are seen throughout not only photosynthesis, but in most optically active materials. External environment (such as illumination) can not always be controlled, so it is important to understand how a material responds. In the case of photosynthesis, photoprotective schemes involving the OCP have been used to prolong organism viability by quenching reactive oxygen radicals. We hypothesize a dynamic fluence response in the ultrafast dynamics of the four-arm star particularly in Cy5 to Cy5.5 transfer. In terms of the Cy5 MPWs, we saw a very dynamic response to increased fluence at room temperature, where notably, excited state lifetime was increased. This fluence-dependence was sensitive to temperature but not solvent, which further complicates matters.

Finally, strong and weak coupling regimes determine the energy transfer pathways that excitations can take in materials. The Fenna-Matthews-Olson complex from green sulfur bacteria is a prime example of modeling using coherent energy transfer and LH2 from purple bacteria can be modeled using a range of energy transfer schemes ranging from FRET between BChl rings to modified Redfield between adjacent BChl *a*. While the four-arm star primarily operates in the weakly coupled (FRET) regime, the dimer MPW demonstrated that control over strongly and weakly coupled dynamics within synthetic systems still has more questions than answers. It becomes evident that novel techniques will be needed to continue to unravel the mysteries of excitonic engineering.

The field of synthetic light harvesting will move forward both from the creation of novel materials and controls for study and from the implementation of new experimental techniques. This is a new frontier for both synthetic chemists as well as spectroscopists. My work has looked on both ends, on one side creating a library of wires to study their fundamental photophysics, on the other hand, theorizing about a whole new type of measurement

which could unlock a closer view to excitons then has ever been achieved. Both sides, however, strive towards the creation of sustainable and robust light harvesting materials.